



UNIVERSIDAD NACIONAL AUTÓNOMA DE MÉXICO
PROGRAMA DE MAESTRÍA Y DOCTORADO EN INGENIERÍA
ELÉCTRICA – SISTEMAS ELECTRÓNICOS

MICRO PLATFORM FOR THE MANIPULATION OF BIOPARTICLES USING
NONUNIFORM ELECTRIC FIELD ELECTROKINETICS

TESIS
QUE PARA OPTAR POR EL GRADO DE:
DOCTOR EN INGENIERÍA

PRESENTA:
OSCAR PILLONI CHOREÑO

TUTOR PRINCIPAL
DRA. LAURA ADRIANA OROPEZA RAMOS, FACULTAD DE INGENIERÍA
COMITÉ TUTOR
DRA. MARGARITA NAVARRETE MONTESINOS, INSTITUTO DE INGENIERÍA
DRA. TATIANA FIOREDELISIO COLL, FACULTAD DE CIENCIAS
DR. FEDERICO MÉNDEZ LAVIELLE, FACULTAD DE INGENIERÍA

CIUDAD UNIVERSITARIA, CD. MX. ENERO 2019



Universidad Nacional
Autónoma de México

Dirección General de Bibliotecas de la UNAM

Biblioteca Central



UNAM – Dirección General de Bibliotecas
Tesis Digitales
Restricciones de uso

DERECHOS RESERVADOS ©
PROHIBIDA SU REPRODUCCIÓN TOTAL O PARCIAL

Todo el material contenido en esta tesis esta protegido por la Ley Federal del Derecho de Autor (LFDA) de los Estados Unidos Mexicanos (México).

El uso de imágenes, fragmentos de videos, y demás material que sea objeto de protección de los derechos de autor, será exclusivamente para fines educativos e informativos y deberá citar la fuente donde la obtuvo mencionando el autor o autores. Cualquier uso distinto como el lucro, reproducción, edición o modificación, será perseguido y sancionado por el respectivo titular de los Derechos de Autor.

JURADO ASIGNADO:

Presidente: Dr. Álvarez Icaza Longoria Luis A.

Secretario: Dra. Navarrete Montesinos Margarita

Vocal: Dra. Oropeza Ramos Laura A.

1 er. Suplente: Dr. Madou Marc Jozef

2 do. Suplente: Dr. Muhl Saunders Stephen

Lugares donde se realizó la tesis:

Laboratorio de microsistemas BioMEMS y Lab on a Chip, Facultad de Ingeniería, UNAM, México.

Departamento de Materiales de Baja Dimensionalidad, Instituto de Investigaciones en Materiales, UNAM, México.

Laboratorio experimental de grafeno, Instituto de Física, UNAM, México.

BioMEMS Laboratory, UCI, USA.

TUTOR DE TESIS:

DRA. LAURA ADRIANA OROPEZA RAMOS

FIRMA

Para Jr.

▪ AGRADECIMIENTOS

La vida es cruel. Se que ésta es una forma rara de empezar una sección de agradecimientos, pero es algo que vemos día a día. Ejemplos sobran de personas que pierden personas o cosas importantes ya sea por desastres naturales, naturaleza humana o enfermedad.

Los esfuerzos de buena parte de la sociedad se enfocan en resolver estos problemas, ya sea de una u otra forma; y aun sabiendo que son problemas titánicos, pequeños avances (pequeñas victorias) como los logrados en el presente trabajo forman la base sobre la cual se fundamentaran sus soluciones.

Sin embargo, estas soluciones no se pueden obtener sin primero sacrificar algo. No se puede ganar algo sin dar otra cosa a cambio.

Hace muchos años (estaba en la preparatoria) murió mi abuelito Vicente, quien, junto a mi abuelita Eloísa, cuidaba de mi mientras mis papás trabajaban. La razón: una enfermedad mal diagnosticada. Recuerdo qué sucedió entre semana, en un día de escuela. También recuerdo las últimas palabras que me dijo: “Hijo, que haces aquí. Deberías estar en la escuela estudiando”. Lo quería mucho.

Ese día perdí a mi abuelito, pero gané algo: determinación.

Decidí que quería hacer algo al respecto. No quería que otras personas sintieran lo que sentí ese día. Así que decidí estudiar para volverme alguien que pudiera ayudar a resolver esos malditos problemas. Y estudiar es lo que hice. Y no paré hasta verme aquí, escribiendo los agradecimientos de una tesis Doctoral (¡y no planeo parar aquí!).

Pero jamás hubiera podido llegar a este punto de no ser por el apoyo y amistad de una cantidad inconmensurable de personas a quienes quisiera agradecer.

Digo inconmensurable, pero lo voy a intentar (perdón por adelantado si alguien se me va).

Voy a empezar por mis papás, Irma y Jaime, a quienes amo y admiro. Les agradezco infinitamente haberme educado, corregido y tolerado mis exabruptos (los viejos y los nuevos). También agradezco a mi carnala Sandra, por ser la voz de la razón en infinidad de

argumentos (aunque no siempre estuviera en lo correcto); y a mi carnal Gustavo por seguir siendo mi mejor amigo, en las buenas y en las malas.

También le doy las gracias a mis primos y primas, tíos y tías, sobrinos y sobrinas que en las reuniones familiares siempre recriminan cuando uno no va... ¡pero como festejan cuando si!

Agradezco a mi otra familia, los amigos que me mantienen cuerdo (bueno, casi) después de semanas continuas de trabajo: Les agradezco a Cesar, Lalo, Gabriel, Jimena, Ana y Lupita por la magia de sentirme niño cuando estoy con ellos. A Arturo, Tabo y David por una buena carcajada a expensas de otros. A Marco, Arturo, Yuri, Israel, Daniel, Samuel, Gerardo, José, Manuel, Brenda y Dina, mi tropa de desorden y aventura.

I also want to thank my friends outside México: Sunny, Albert S, Ehsan, Sasha, Brandon, Maziar, Michelle, Derosh, Victor, Michiel, Maria, Albert L and Horacio. May the party and the research never end!

Agradezco a mi otra otra familia, los chicos y chicas del laboratorio de BioMEMS: Sveidy, Edgar, Fer, LG, Erick, Mike y Poncho. Por haber compartido parte del viaje en la máquina del tiempo que es nuestro laboratorio.

A los doctores con los que trabajé: Dr. Federico, Dra. Tatiana, Dra. Margarita, Dr. Marc, Dr. Luis O, Dr. Luis A, Dr. Naser, Dra. Laura S, Dr. Enrique, Dr. Doroteo y Dr. Stephen, y a todos sus estudiantes que conocí, y de quienes aprendí tanto en tan poco tiempo.

En particular, le agradezco mucho a la Dra. Laura O. en quien encontré no solo a una fenomenal mentora sino también a una amiga.

Y finalmente, agradezco a mis abuelitos Luis y Sara, que, aunque prácticamente no los conocí me dieron un papá genial, y a mi abuelita Eloísa y mi abuelito Vicente por darme la mejor mamá del mundo.

■ **AGRADECIMIENTOS INSTITUCIONALES**

Atentamente agradezco a:

Al Consejo Nacional de Ciencia y Tecnología (CONACYT) por la beca número 487698 que me permitió desarrollar el presente trabajo.

A los proyectos DGAPA-PAPIIT-UNAM número IN115116 y IN106316 cuyos financiamientos permitieron el desarrollo de esta tesis.

Al proyecto CONACYT-UNAM número 269280 por la adquisición de un tribómetro Nanovea.

Al proyecto CONACYT Fronteras de la Ciencia número 344 que aportó parte del financiamiento para el proyecto del que deriva la tesis.

A la beca mixta CONACYT 2016 numero 291062 que me permitió realizar una estancia en la University of California Irvine, Estados Unidos.

A la Ma. Cristina Zorrilla Cangas del Laboratorio de Materiales Avanzados del Instituto de Física de la UNAM por su asistencia en la realización de espectroscopía Raman.

Al Laboratorio Central de Microscopía del Instituto de Física, al Laboratorio Universitario de Microscopia Electrónica del Instituto de Investigación en Materiales y al Laboratorio de Microscopia Electrónica de la Facultad de Ingeniería de la UNAM por las facilidades prestadas para la obtención de imágenes SEM.

Al Dr. Doroteo Mendoza López del Instituto de Investigaciones en Materiales y a la Dra. Laura Serkovic Loli del Instituto de Física de la UNAM por su ayuda en la realización de los experimentos de pirolisis.

Al Dr. Stephen Muhl del Instituto de Investigaciones en Materiales de la UNAM por su ayuda en la medición de las propiedades tribológicas del material producido.

A la Dra. Laura Oropeza Ramos de la Facultad de Ingeniería de la UNAM por facilitar las instalaciones donde se realizaron la mayoría de los procesos de fabricación y experimentación.

▪ RESUMEN

El posicionamiento preciso de micropartículas dentro de un volumen micrométrico ha sido un tema importante para el estudio de sistemas biológicos complejos durante años. La micromanipulación de células biológicas se puede utilizar para estudiar una variedad de fenómenos biológicos, como la capacidad de ciertas células para replicarse, las interacciones célula a célula, la actividad bioquímica y las propiedades micromecánicas de las células, para enumerar solo algunas.

A partir de las técnicas de micromanipulación disponibles, la dielectroforesis se ha vuelto popular debido a su selectividad y fácil implementación en sistemas microelectromecánicos (MEMS, por sus siglas en inglés). Esta técnica obtiene beneficios adicionales al combinarla con nuevos dispositivos MEMS a base de carbono (C-MEMS), como lo son la estabilidad electroquímica y la biocompatibilidad que exhiben los microelectrodos de carbono.

Un fenómeno electrocinético conocido como dielectroforesis actualmente solo se ha utilizado para manipular micropartículas en espacios bidimensionales, aunque tiene potencial para ser útil en el posicionamiento preciso de micropartículas en volúmenes tridimensionales.

En el presente trabajo se diseñó, fabricó y probó una microplataforma que utiliza una combinación de microelectrodos de carbono planares (2D) y extruidos (3D), individualmente accesibles y construidos sobre un sustrato transparente, para el posicionamiento preciso de micropartículas objetivo dentro de un microvolumen mediante el uso de la fuerza de dielectroforesis.

Los microelectrodos de carbono fueron caracterizados metódicamente, encontrando que el material producido fue carbono vítreo con máximos en espectro Raman encontrados en $1350 \pm 1.4 \text{ cm}^{-1}$ y $1585 \pm 0.4 \text{ cm}^{-1}$, exhibiendo una resistividad eléctrica de $0.382 \pm 0.003 \text{ m}\Omega \text{ m}$, una fuerza de adhesión al sustrato de $3.212 \pm 0.32 \text{ N}$, y alturas promedio de trazas conductoras de $10.3 \pm 0.18 \mu\text{m}$, electrodos 2D de $15.3 \pm 0.32 \mu\text{m}$ y electrodos 3D de $33.5 \pm 0.54 \mu\text{m}$.

Como prueba de concepto, se realizaron experimentos de micromanipulación empleando micropartículas de plástico fluorescente. Se observó una fuerza de DEP negativa para el experimento propuesto (factor de Clausius-Mossotti ~ -0.5) a voltajes aplicados relativamente bajos ($\sim 15 \text{ V}$). Es decir, las partículas fueron repelidas de regiones con gradientes de campo eléctrico de gran magnitud.

Por encima de todo, se logró la micromanipulación de partículas en el microvolumen.

Finalmente, se discuten las ventajas y limitaciones de la plataforma propuesta.

▪ **ABSTRACT**

Precise positioning of micro particles inside a microvolume has been an important topic to perform the study of complex biological systems for many years. Micromanipulation of biological cells can be used to study a variety of topics, such as the ability of certain cells to replicate, cell to cell interactions, biochemical activity and cell micro mechanical properties, to list just a few.

From the available micromanipulation techniques, dielectrophoresis has become popular due to its selectivity and easy implementation in micro electro mechanical systems (MEMS). This is improved even further by new advancements using carbon-based MEMS (C-MEMS), with the added benefits that carbon microelectrodes exhibit, such as electrochemical stability and biocompatibility.

An electrokinetic phenomenon known as dielectrophoresis has currently only been used to manipulate micro particles in two dimensional spaces although it has potential to be useful in the precise positioning of microparticles in tridimensional volumes.

In the present work a micro platform was designed, fabricated and tested for the precise positioning of target micro particles inside a microvolume by means of dielectrophoretic forces. The micro platform was made of a combination of individually addressable planar (2D) and extruded (3D) carbon microelectrodes built on a transparent substrate.

The produced carbon microelectrodes were methodically characterized, finding that the produced material was glassy carbon with Raman spectra peaks found at $1350 \pm 1.4 \text{ cm}^{-1}$ and $1585 \pm 0.4 \text{ cm}^{-1}$, an electrical resistivity of $0.382 \pm 0.003 \text{ m}\Omega \text{ m}$, an adhesion force to the

substrate of 3.212 ± 0.32 N, and average electrical trace heights of $10.3 \pm 0.18 \mu\text{m}$, 2D electrode heights of $15.3 \pm 0.32 \mu\text{m}$ and 3D electrode heights of $33.5 \pm 0.54 \mu\text{m}$.

As a proof of concept, micromanipulation experiments employing plastic fluorescent microparticles were performed. A negative DEP force was observed for the proposed experiment (Clausius-Mossotti factor ~ -0.5) at relatively low applied voltages (~ 15 V). That is, particles were repelled from regions with high electrical field gradients.

Above all, particle micromanipulation in the microvolume was achieved.

Finally, the advantages and limitations of the proposed platform are discussed.

Contents

▪ Agradecimientos	4
▪ Resumen	8
▪ Abstract	10
▪ List of figures	17
▪ List of tables	21
1 Introduction	23
1.1 Motivation	23
1.2 Hypothesis	24
1.3 Objectives	24
2 Theoretical background	26
2.1 Bioparticle manipulation in the microscale	27
2.1.1 Bioparticle micromanipulation	27
2.1.2 Mechanical micromanipulation	27
2.1.3 Optical micromanipulation	28
2.1.4 Electrokinetic micromanipulation	28
2.1.5 Selection of the micromanipulation technique	29
2.2 Dielectrophoretic (DEP) force	30
2.2.1 Polarizable particles and the effective dipole moment	31
2.2.2 DEP force for the nth multipole moment	35
2.2.3 DEP models for bioparticles	38
2.3 Fluid mechanics in a microvolume	39
2.3.1 Suspended particles in a fluid	39
2.3.2 Velocity field	40

2.3.3	Boundary conditions	40
2.3.4	Flow regimes	43
2.3.5	Constitutive equations for incompressible flow	46
2.4	Microelectrode arrays for dielectrophoretic manipulation	49
2.4.1	Types of operating strategies	49
2.4.2	Microelectrode geometries for particle micromanipulation	53
2.4.3	Carbon-based microelectromechanical systems (C-MEMS)	57
2.4.4	Considerations for the micromanipulation of bioparticles	60
3	Micro platform design and fabrication	64
3.1	Design goals	64
3.2	Micro platform modules	67
3.2.1	Microelectrode array	68
3.2.2	Microfluidics	75
3.2.3	Control electronics	78
4	Micro platform tests and results	83
4.1	Microelectrode array metrology	83
4.1.1	Optical microscopy	83
4.1.2	Scanning electron microscopy (SEM)	85
4.1.3	Optical profilometry	87
4.1.4	Raman spectra	89
4.1.5	Electrical resistivity	90
4.1.6	Adhesion to substrate	91
4.2	Experimental array	92
4.2.1	Complete micro-platform	92
4.2.2	Proof of concept experiment	94

4.2.3	Micromanipulation experiment	96
5	Conclusions	101
▪	References	104
▪	Appendix A: Electric potential induced by charge distribution	113
▪	Appendix B: Viscosity	119
▪	Appendix C: Microelectrode array designs and fabrication protocols	122
○	Design schematics	122
○	Photolithography	128
○	Pyrolysis	131
○	Electronics interface board	133
▪	Appendix D: Microfluidics module designs and fabrication protocols	134
○	Design schematics	134
○	Soft lithography	136
○	Support structure design schematics	137
▪	Appendix E: Control electronics module designs and software	138
○	Electrical schematics	138
○	PCB schematics	140
○	Bill of materials	142
○	Support structure design schematics	143
▪	Appendix F: Control electronics module software	144
○	Raspberry PI firmware	144
○	Computer interface software	144
▪	Appendix G: MATLAB programs	156
○	Clausius-Mossotti factor and electric field strength	156
○	Van der Pauw's numerical resistivity computation	157

- Appendix H: Article “Micro Device for Bio-Particle Positioning in a 3D space based on Carbon MEMS and Dielectrophoretic Forces” 158
- Appendix I: Article “Methodology and Fabrication of Adherent and Crack-free SU-8 Photoresist-derived Carbon MEMS on Fused Silica Transparent Substrates” 171

■ LIST OF FIGURES

Fig. 1: Spherical dielectric particle with complex permittivity $\epsilon p *$ immersed in a medium with complex permittivity $\epsilon m *$ and under the influence of an electric field E parallel to the x-axis.	31
Fig. 2: Graphical representation of the n th multipole moment formed inside a dielectric particle. Moments up to $n=3$ are shown.	36
Fig. 3: Positive (left) and negative (right) DEP force exerted on a bioparticle by a microelectrode generating an electric field.	37
Fig. 4: Living cell and successive approximations to simplify it by the multi shell model.	38
Fig. 5: Velocity profile of a fluid trapped in between a fixed and a moving plate.	41
Fig. 6: Navier's extrapolation model for slipping boundaries.	42
Fig. 7: Example of laminar, transitional and turbulent flow lines.	43
Fig. 8: Microelectrode geometries for DEP micromanipulation [51]. (A) Castellated, (B) Insulator-based, (C) Quadrupole, (D) Curved, (E) Interdigitated, (F) Matrix, (G) Microwells, (H) Oblique, (I) Sidewall patterned, (J) Top-bottom patterned, (K) Contactless, (L) Extruded and (M) 3D C-MEMS.	53
Fig. 9: High aspect ratio microstructures fabricated with C-MEMS technology [97].	58
Fig. 10: Combination of planar and 3D C-MEMS microelectrodes. Using pulsed DEP between 3D electrodes for movement parallel to the substrate, and pulsed DEP between planar electrodes and a top counter electrode for movement normal to the substrate.	62
Fig. 11: Lateral view of the proposed design.	62
Fig. 12: Modules that conform the micro platform for manipulation of bioparticles.	67
Fig. 13: Conceptual design for microelectrode type and placement. 3D electrodes control x-axis and y-axis movement while 2D electrodes and a top counter electrode control z-axis movement.	68
Fig. 14: Design evolution of the microelectrode array. Ordered from earliest (a) to latest (f) with f being the final design used in the micro platform.	70
Fig. 15: Electric field generated by a combination of a 3D and a 2D electrodes (left), and two 2D electrodes (right). Red vector sizes are proportional to the electric field strength.	73
Fig. 16: Snapshots of a 60 second simulation of particle movement along the substrate plane for three configurations of selected 3D microelectrodes. Particle sizes were scaled to 1/10 their size for clarity. No particle-particle interaction was simulated.	73
Fig. 17: Simulated electric field strength using a two-electrode configuration. (Top left) Electric potential applied. Resulting gradient of the squared electric field in the volume (top right) and in the yz-plane (bottom left) represented by red vectors. Vector size is proportional to field intensity. (bottom right) Numerical values for the yz-plane electric field at four different distances above the microelectrode array base.	74
Fig. 18: Conceptual use of multiple microfluidic chip designs with a single microelectrode array chip. For this to be possible, a temporal interface strategy had to be developed.	75

Fig. 19: (Top) Microchannel layer built in the microelectrode array module, and (bottom) PDMS chip that adds the counter electrode (ITO covered slide) for micromanipulation in the z-axis and seals the microchannel.	76
Fig. 20: Microfluidic module support structure. Bottom part slides in the microelectrode array interface board and functions as an anchor support for the top part. The top part holds the PDMS chip and is mechanically secured to the bottom part using four bolts.	77
Fig. 21: Block diagram of the electronic submodules and electric signals used in the control electronics module.	78
Fig. 22: Graphic user interface (GUI) that controls the electrical state of each microelectrode.	79
Fig. 23: Pinout and designator names for each microelectrode.	80
Fig. 24: Electrical connections for the signal rails interfacing with each microelectrode. Switches on the left side select the DEP voltage source while switches in the right side select the electrode state (VDEP, GND or High-z).	81
Fig. 25: Control electronics module mounted in a minimalistic custom support.	81
Fig. 26: Step by step graphical renders (a) and photographs (b) of the microelectrode array fabrication process. Layers 1 through 3 were patterned before pyrolysis and layer 4 after pyrolysis.	83
Fig. 27: Photograph of the full microelectrode C-MEMS chip after pyrolysis.	84
Fig. 28: Photograph of the complete electronics interface board with C-MEMS microelectrodes connected to the PCB.	84
Fig. 29: 200x SEM image of the carbon microelectrode array after pyrolysis.	85
Fig. 30: 500x SEM image of the 2D and 3D microelectrodes. Some distortion at the interface between layer 2 and 3 is observed. Also, there is a deformation on the smallest diameter microelectrode structures.	86
Fig. 31: 4000x SEM image of the carbon microstructures. Top right corner is substrate while bottom left is a carbon microstructure. No appreciable pores were found at this scale.	86
Fig. 32: Optical profilometry of the microelectrode array. (Left) 3D perspective, (top right) top perspective and (bottom right) photograph of the measured zone.	87
Fig. 33: Optical profilometry of the 2D microelectrodes. (Left) 3D perspective, (top right) top perspective and (bottom right) photograph of the measured zone.	88
Fig. 34: Optical profilometry of the 3D microelectrodes. Note the aberration due to a diameter mismatch between layers 2 and 3. (Left) 3D perspective, (top right) top perspective and (bottom right) photograph of the measured zone.	88
Fig. 35: Raman spectra of the produced carbon microstructures. Both spectra show the characteristic peaks of pyrolytic carbon close to the 1350 cm^{-1} and 1580 cm^{-1} bands.	89
Fig. 36: (Top) Scratch test representative schematic and (Bottom) a pair of scratch test measurements. Loading tip traveled from left to right. Spallation force was reached at the marked spots.	91

Fig. 37: Assembly of the micro platform. _____	92
Fig. 38: Snapshots of a 9 second $1\ \mu\text{m}$ particle suspension experiment. Orange electrode is connected to V_{DEP} while blue electrode is connected to ground. A particle and its motion are highlighted in red. Note its movement in a vector colinear to the applied electric field, and away of the closest electrically active microelectrode indicating nDEP. _____	94
Fig. 39: Particle image velocimetry of the experiment described in Fig. 38. The white arrows represent the velocity vectors of the microparticles and are indicative of microparticle movement. _____	95
Fig. 40: Experimental setup for the micromanipulation experiment with the micro platform. _____	96
Fig. 41: Snapshots of single particle micromanipulation experiments along the xy-plane (a and c) and in the z-axis directions (b). In sequence b, note how the particle enters and exits the focal plane of the microscope. Orange arrows denote intended particle motion before the experiment. Green arrows denote actual particle movement during the experiment. Concentric circles denote movement perpendicular to the focal plane (z-axis). Working electrodes (red = V_{DEP} and blue = GND) and particle movement (green circle) are highlighted. _____	98
Fig. 42: Snapshots of multiple particle micromanipulation experiments along the xy-plane (a-c). Orange arrows denote intended particle motion before the experiment. Green arrows denote actual particle movement during the experiment. Working electrodes (red = V_{DEP} and blue = GND) and particle movement (green circle) are highlighted. _____	99
Fig. 43: Point charge q placed on the z-axis and arbitrary point P where the electric potential needs to be calculated. _____	113
Fig. 44: Diagram of the variables involved in the definition of dynamic viscosity. _____	120
Fig. 45: Velocity profile of a fluid trapped in between a fixed and a moving plate. _____	121
Fig. 46: Layer 1 [mm]. _____	122
Fig. 47: Blue detail from layer 1 [mm]. _____	123
Fig. 48: Purple detail from Fig. 47 [mm]. _____	123
Fig. 49: Layer 2 [mm]. _____	124
Fig. 50: Blue detail from layer 2 [mm]. _____	124
Fig. 51: Layer 3 [mm]. _____	125
Fig. 52: Blue detail from layer 3 [mm]. _____	125
Fig. 53: Layer 4 [mm]. _____	126
Fig. 54: Blue detail of layer 4 [mm] _____	126
Fig. 55: Layer 5 [mm]. _____	127
Fig. 56: Blue detail from layer 5 [mm]. _____	127
Fig. 57: Multilayer photolithography process. _____	128
Fig. 58: Heating profile for the vacuum pyrolysis process. _____	132

<i>Fig. 59: (Left) Silk and (right) top copper layers of the electronics interface PCB. Actual size. Part ST60-18P was used for connector J4.</i>	133
<i>Fig. 60:PDMS chip schematics [mm].</i>	134
<i>Fig. 61: ITO-covered glass slide dimensions [mm]. Thickness = 0.8 mm.</i>	134
<i>Fig. 62: PDMS chip mold schematics [mm].</i>	135
<i>Fig. 63: Microfluidic module support structure top part [mm].</i>	137
<i>Fig. 64: Microfluidic module support structure bottom part [mm].</i>	137
<i>Fig. 65: Power regulation and voltage rails.</i>	138
<i>Fig. 66: Voltage test terminals (left) and protection stage for the microcontroller input signals (right).</i>	138
<i>Fig. 67: Analog switch array and terminal for external DEP signals.</i>	139
<i>Fig. 68: Internal VDEP signal generator.</i>	139
<i>Fig. 69: Top layer silk labels. Actual size.</i>	140
<i>Fig. 70: Top layer PCB design. Actual size.</i>	140
<i>Fig. 71: Bottom layer PCB design. Actual size.</i>	141
<i>Fig. 72: Support structure for the electronics control module. Isometric front view [mm].</i>	143
<i>Fig. 73:Support structure for the electronics control module. Isometric back view [mm].</i>	143
<i>Fig. 74: (Left) Design components and (right) handler names of each element of the software window.</i>	144

▪ LIST OF TABLES

<i>Table I: Relevant characteristics of the different DEP operational strategies [51].</i>	<i>60</i>
<i>Table II: Relevant characteristics of microelectrode geometries for DEP particle micromanipulation [51].</i>	<i>61</i>
<i>Table III: Proposed design parameter for the micro-platform.</i>	<i>66</i>
<i>Table IV: Spin coater parameters for photoresist deposition.</i>	<i>129</i>
<i>Table V: Layer exposure parameters for the mask-less exposure machine.</i>	<i>130</i>
<i>Table VI: Heating profile and gas flows for the pyrolysis process under a forming gas atmosphere.</i>	<i>132</i>

1 INTRODUCTION

1.1 MOTIVATION

The study of life and living organisms is of undeniable importance. Be it by the study of the chemical processes, physical structure or physiological mechanisms that permit life, or the study of how to prevent, diagnose and treat the diseases that disturb it.

Cell biology is a sub category of these studies that seeks to understand how cells work, their structure, chemical composition, function, physiological properties, interactions with their environment and life cycle. That is, cell biology seeks to understand the fundamental unit of life.

A group of technologies have been developed or implemented to further our understanding of cell biology, such as micromanipulation techniques, fluorescent microscopy, cytometry, scanning probe microscopy, Raman microspectroscopy, microbeam analysis, and biological microelectromechanical systems (Bio-MEMS) [1].

For these technologies, micromanipulation is fundamental to allow the positioning or isolation of target cells or, more general, bio particles suspended in a liquid medium. A strategy developed to achieve this uses nonuniform electric field electrokinetic phenomena to polarize the bioparticle and induce a net force on it. This phenomenon is known as dielectrophoresis.

Although dielectrophoresis has been successfully used to position bioparticles in a plane inside microchannels, it has the unexploited potential to be used for bioparticle tridimensional positioning inside a microvolume.

1.2 HYPOTHESIS

Even though dielectrophoresis has proven to be useful to position or to trap bioparticles in a confined position inside two dimensional micro channels, this phenomenon has the potential to be applied for tridimensional positioning of a target bioparticle inside a microvolume. As far as we know, this potential hasn't been exploited in a micro platform.

Hypothesis: It is possible to design and fabricate a micro platform capable of using nonuniform electric fields to position bioparticles inside a microvolume.

1.3 OBJECTIVES

Main objective

Develop an experimental methodology for the fabrication of a micro platform that uses nonuniform electric field electrokinetics to manipulate bioparticles.

Secondary objectives

- Investigate the theoretical basis that describes the use of nonuniform electric field electrokinetics for bioparticle manipulation.
- Develop the experimental methodology necessary to fabricate tridimensional microelectrode arrays in microfluidic chips.

2 THEORETICAL BACKGROUND

We start by defining our unit of interest: the bioparticle. Then, we continue to describe the usefulness of manipulating its position inside a microvolume, current micromanipulation techniques and the main advantages of using an electrokinetic approach to do this manipulation.

From the electrokinetic phenomena introduced, dielectrophoresis is shown to have key advantages for bioparticle positioning. Theory of operation, dielectrophoresis models for bioparticles and state of the art micro manipulation devices are addressed.

Afterwards, a summary of relevant fluid mechanics in the microscale is given. This is done to introduce the forces involved in the motion of a target bioparticle suspended in a liquid media and the role that electrokinetic forces play in that motion.

We continue by introducing the types of microelectrode arrays used to induce dielectrophoretic forces, our electrokinetic force of choice, for micromanipulation and the special considerations the system must address when positioning bioparticles.

Finally, carbon based microelectromechanical systems (C-MEMS) are introduced as a new and desirable technology for the fabrication of devices for the micromanipulation of bioparticles.

2.1 BIOPARTICLE MANIPULATION IN THE MICROSCALE

2.1.1 Bioparticle micromanipulation

The term “Bioparticle” is widely used to refer to particles made of biological matter. That is, the term refers to any small unit that can be associated to a biological system or process. Cells [2], bacteria [3], DNA [4] and proteins, for example, are all bioparticles by this definition.

The study of the structures, interaction with the environment and inner functioning of the bioparticles is fundamental for biological sciences, and their research requires technologies and tools that enable their visualization, characterization and manipulation.

From these technologies, micromanipulation has been widely used to separate bioparticles based on particular criteria [5]–[8], confine specific bioparticles for further analysis [9]–[12], and move bioparticles to desired locations for further processing or inspection [13]–[17]. Current micromanipulation techniques can be divided by their actuation principle into mechanical, optical and electrokinetic [1].

2.1.2 Mechanical micromanipulation

Mechanical micromanipulation is achieved by using a medium or physical object to exert mechanical forces in a target particle. This method has been implemented by attaching micromanipulator arms directly to microscopes to move and count cell populations. Current technologies employ electrical micromanipulators that can be automated for improved throughput and precision. Other mechanical methods for micromanipulation include atomic force microscopy, micro-probe force transduction and flow force transduction.

Although this technique is easy and fast to implement and is pervasive in disciplines that require micromanipulation (biology, medicine), it needs bulky setups surrounding the test area which are not easily miniaturizable.

2.1.3 Optical micromanipulation

The use of techniques that induce optical pressure to control the position of a target microparticle is known as optical micromanipulation. In this technique, a laser is used to induce enough optical pressure on even large particles (such as microbial cells) to move, twist, pull, trap or cut them.

Even though this micromanipulation technique has proven useful by techniques such as optical tweezers, there exists a risk of photodamaging the target particles. This happens due excessive power dissipation at the particle's surface due to inadequate laser power or wavelength selection. This technique requires a source of highly collimated light with enough power to induce an adequate optical pressure, and some means to move the laser beam to move the particle, both things being hard to miniaturize and integrate in a micro platform.

2.1.4 Electrokinetic micromanipulation

Electrokinetic manipulation relies in the Coulomb forces induced into a particle or medium to exert movement through the application of an electric potential. There are three main electrokinetic phenomena:

- Electro-osmosis: Induced motion on a polarized medium which carries the suspended species of interest. Here, the medium experiences an electromotive force while the target particles are dragged mechanically by it.
- Electrophoresis: Induced motion in suspended polarized particles through electrostatic attraction or repulsion. This requires that the target particles be already polarized, that is, they must have a non-zero electrical charge.
- Dielectrophoresis: Induced motion in suspended neutral particles through the application of a nonuniform electric field.

2.1.5 Selection of the micromanipulation technique

Each micromanipulation method has advantages and caveats. Two main points were considered to choose an actuation technique: ability to miniaturize the elements needed to generate said actuation, and ability to directly manipulate bioparticles.

Electrokinetics usually requires microelectrodes built directly in the device to induce their actuation forces, while mechanical and optical techniques require mounting of the device in specialized experimental arrays that have mechanical micromanipulator probes or electromechanically controlled laser emitters, respectively. This already favors the use of electrokinetic phenomena for the micro platform due to the possibility of building a custom array of microelectrodes to apply the desired electromotive force inside of microvolume. Another point in favor lies in the supporting devices that enable the use of electrokinetics: only a controlled source of electric potential is needed, which can also be easily miniaturized.

From the electrokinetic phenomena presented, it is necessary to pick one technique for the micro platform suitable for the manipulation of bioparticles. Because many bioparticles such as cells, microorganisms, proteins and DNA are considered to be electrically neutral, dielectrophoresis was chosen over electrophoresis and electro-osmosis as the actuation force for the micro platform because it allows direct micromanipulation of neutral particles.

2.2 DIELECTROPHORETIC (DEP) FORCE

Dielectrophoretic phenomena occurs when a dielectric particle suspended in a medium becomes polarized by an external nonuniform electric field, inducing a net force on the particle[18].

Since first described by H. A. Pohl in 1951 [19], dielectrophoresis (DEP) has received much interest by the scientific community because it enables the application of an electric force unto an electrically neutral particle [20]–[22].

The polarization of an electrically neutral particle results from an accumulation of charges at the interface between the particle and the medium. This is known as Maxwell-Wagner polarization or interface polarization.

Two factors contribute to this polarization: the perturbation to the particle's internal charges induced by the electric field, and the movement of free surface charges at the particle-medium interface [23].

The DEP force ($\bar{\mathbf{F}}_{DEP}$) induced into a particle due to this polarization can be determined by the dipole moment ($\bar{\mathbf{p}}$) generated by the net charge density (\mathbf{q}), and the electric field intensity (\mathbf{E}). This relationship is shown in eq. (1).

$$\bar{\mathbf{F}}_{DEP} = \bar{\mathbf{p}} \cdot \nabla \bar{\mathbf{E}} \quad (1)$$

To understand how the dielectrophoretic effect exerts a force it is necessary to describe the dipole moment that acts in a dielectric particle due to the electric potential generated by its polarization due to an external electric field. In the following sections, the multipole moment induced in a spherical particle is obtained (From which the dipole results as a particular case). This multipole is then used to obtain the DEP force exerted to the particle. Finally, the multi shell model for particles is introduced which serves to better approximate the dielectric behavior of complex particles, such as bioparticles.

2.2.1 Polarizable particles and the effective dipole moment

It is of interest to know the way in which a particle made of a dielectric material is polarized due to the distribution of charges, caused by the external influence of an electric field, at the interface between it and the medium.

We start by defining a homogeneous and isotropic sphere that represents a first approximation of a polarizable particle. This sphere has radius R_p , complex electrical permittivity ϵ_p^* , and it is immersed in a homogenous medium with complex electrical permittivity ϵ_m^* .

For such a sphere, we have that the electric potential caused by an arbitrary distribution of charge along a line inside it is identical to the potential of a system of multipoles located at its center [24], as long as the diameter of the sphere coincides with the length of the line.

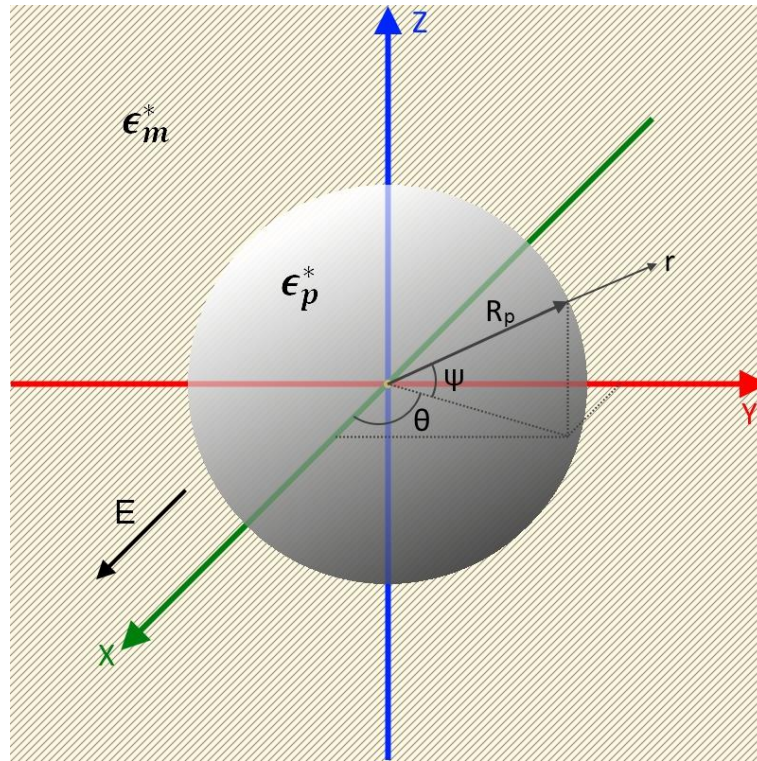


Fig. 1: Spherical dielectric particle with complex permittivity ϵ_p^* immersed in a medium with complex permittivity ϵ_m^* and under the influence of an electric field \mathbf{E} parallel to the x -axis.

In order to deduce the way in which the particle will polarize and generate its own electric potential (ϕ), the following boundary conditions must be applied, and must hold true [30]:

- I. The electric potential must be continuous across the interface between medium (ϕ_m) and particle (ϕ_p). $\phi_m = \phi_p$.
- II. The normal component of the gradient of the electric potential at the particle's surface must be constant across the interface. $\epsilon_m^* \left(\frac{d\phi_m}{dr} \right) = \epsilon_p^* \left(\frac{d\phi_p}{dr} \right)$.
- III. The particle's electric potential must satisfy Laplace equation across all space. $\nabla^2 \phi = 0$.

We define the complex electrical permittivity with eq. (2).

$$\epsilon^* = \epsilon - i \left(\frac{\sigma}{\omega} \right) \quad (2)$$

Where:

ϵ = Electrical permittivity $\left[\frac{F}{m} \right]$.

σ = Electrical conductivity $\left[\frac{S}{m} \right]$.

$\omega = 2\pi f$ = Angular frequency of the electric field [Hz].

To obtain the electric field of the particle under these conditions we align an externally applied electric field (\mathbf{E}) with the x-axis, as shown in Fig. 1. If the particle polarizes homogeneously, it creates an internal electric field (\mathbf{E}_p) that is symmetric to the external field about the x-axis. The particle's internal electric potential (ϕ_p) is then defined by eq. (3).

$$\phi_p = -\mathbf{E}_p \mathbf{r} \cos \theta \quad (3)$$

Now, the electric potential outside the particle (ϕ_m) must be the superposition of the potential generated by the external electric field and the potential generated by the multipoles defined by eq. (4), which represents the electric potential induced by a charge distribution. For an in dept description of eq. (4) see Appendix A: Electric potential induced by charge distribution.

$$\phi_n = \frac{(-1)^n \mathbf{p}_n}{4\pi\epsilon_n! r^{n+1}} [\cdot]^n (\nabla)^n \left(\frac{1}{r} \right) \quad (4)$$

For simplicity, only the dipole (\mathbf{p}_1) will be considered (eq. (4) with $n = 1$).

$$\phi_m = -E r \cos \theta + \left(\frac{1}{4\pi\epsilon_m} \right) \frac{\cos \theta}{r^2} \mathbf{p}_1 \quad (5)$$

Equations (3) and (5) satisfy condition (III) because the divergence and rotational of the field are both equal to zero. We investigate \mathbf{p}_1 and E_p by using boundary conditions (I) and (II) when $r \rightarrow R_p$, giving us eq. (6) and (7).

$$-E_p R_p \cos \theta = -E R_p \cos \theta + \left(\frac{1}{4\pi\epsilon_m} \right) \frac{\cos \theta}{R_p^2} \mathbf{p}_1 \quad (6)$$

$$-E_p \epsilon_p^* \cos \theta = -E \epsilon_m^* \cos \theta - \left(\frac{2\epsilon_m^*}{4\pi\epsilon_m} \right) \left(\frac{\cos \theta}{R_p^3} \right) \left(\frac{d}{dr} \mathbf{p}_1 \right) \quad (7)$$

By solving eq. (6) and (7) we find that \mathbf{p}_1 and E_p are defined as shown in eq. (8) and eq. (9).

$$E_p = \frac{3\epsilon_m^*}{\epsilon_p^* + 2\epsilon_m^*} E \quad (8)$$

$$\mathbf{p}_1 = 4\pi\epsilon_m R_p^3 \frac{\epsilon_p^* - \epsilon_m^*}{\epsilon_p^* + 2\epsilon_m^*} E \quad (9)$$

The relationship of the complex electrical permittivity of the particle and the medium surrounding it is known as the Clausius-Mossotti factor (K) [31] (eq. (10)). This factor contains information of the degree of polarizability the particle has in a medium.

$$K = \frac{\epsilon_p^* - \epsilon_m^*}{\epsilon_p^* + 2\epsilon_m^*} \quad (10)$$

Equation (9) can be rewritten as a vector that describes the effective dipole moment induced in a dielectric particle by an external electric field (eq. (11)) [32].

$$\bar{p}_1 = 4\pi\epsilon_m R_p^3 K \bar{E} \quad (11)$$

From equations (10) and (11) it is possible to derive the following conclusions:

- For a dipole moment to be able to form, the complex electrical permittivities of the involved materials must not be equal. ($\epsilon_p^* \neq \epsilon_m^*$).
- The dipole moment can collinearly follow the direction of the external electric field ($\epsilon_p^* > \epsilon_m^*$) or go in the opposite direction ($\epsilon_p^* < \epsilon_m^*$).

2.2.2 DEP force for the nth multipole moment

T. B. Jones et. al expanded the expression in eq. (11) to obtain the nth multipole moment of a particle under a dielectrophoretic effect [28] (eq. (12)). See that also the Clausius-Mossotti factor (eq. (10)) was redefined for the nth multipole $\mathbf{K}^{(n)}$ factor (eq. (13))

$$\bar{\mathbf{p}}_n = \frac{4\pi n \epsilon_m}{(2n-1)!!} \mathbf{K}^{(n)} \mathbf{R}_p^{2n+1} (\nabla)^{(n-1)} \bar{\mathbf{E}} \quad (12)$$

$$\mathbf{K}^{(n)} = \frac{\epsilon_p^* - \epsilon_m^*}{n\epsilon_p^* + (n+1)\epsilon_m^*} \quad (13)$$

By using the $\bar{\mathbf{p}}_n$ multipole in eq. (1) and grouping terms using the dyadic notation, we obtain the general expression for the dielectrophoretic force for the nth multipole moment (eq. (14)), where $[\cdot]^n$ represents the nth application of the dot product to the dyadic tensor, and $(\nabla)^n$ represents the application of n ∇ operators to the electric field [28].

$$\bar{\mathbf{F}}_{DEP_n} = \text{Re} \left[\frac{\bar{\mathbf{p}}_n}{n!} [\cdot]^n (\nabla)^n \bar{\mathbf{E}} \right] \quad (14)$$

Finally, the total time average dielectrophoretic force exerted on a dielectric particle suspended in a medium and under the effects of an electric field is given by eq. (15) [20]. This expression is usually simplified to obtain the DEP force due to the dipole moment (eq. (16)).

$$\langle \mathbf{F}_{DEP} \rangle = \frac{1}{2} \sum_{n=1}^{\infty} \text{Re} \left[\frac{4\pi \epsilon_m \mathbf{K}^{(n)} \mathbf{R}_p^{2n+1}}{(n-1)! (2n-1)!!} (\nabla)^{(n-1)} \bar{\mathbf{E}} [\cdot]^n (\nabla)^n \bar{\mathbf{E}} \right] \quad (15)$$

$$\langle \mathbf{F}_{DEP_1} \rangle = 2\pi \epsilon_m \mathbf{R}_p^3 \text{Re}[\mathbf{K}] \nabla \bar{\mathbf{E}}^2 \quad (16)$$

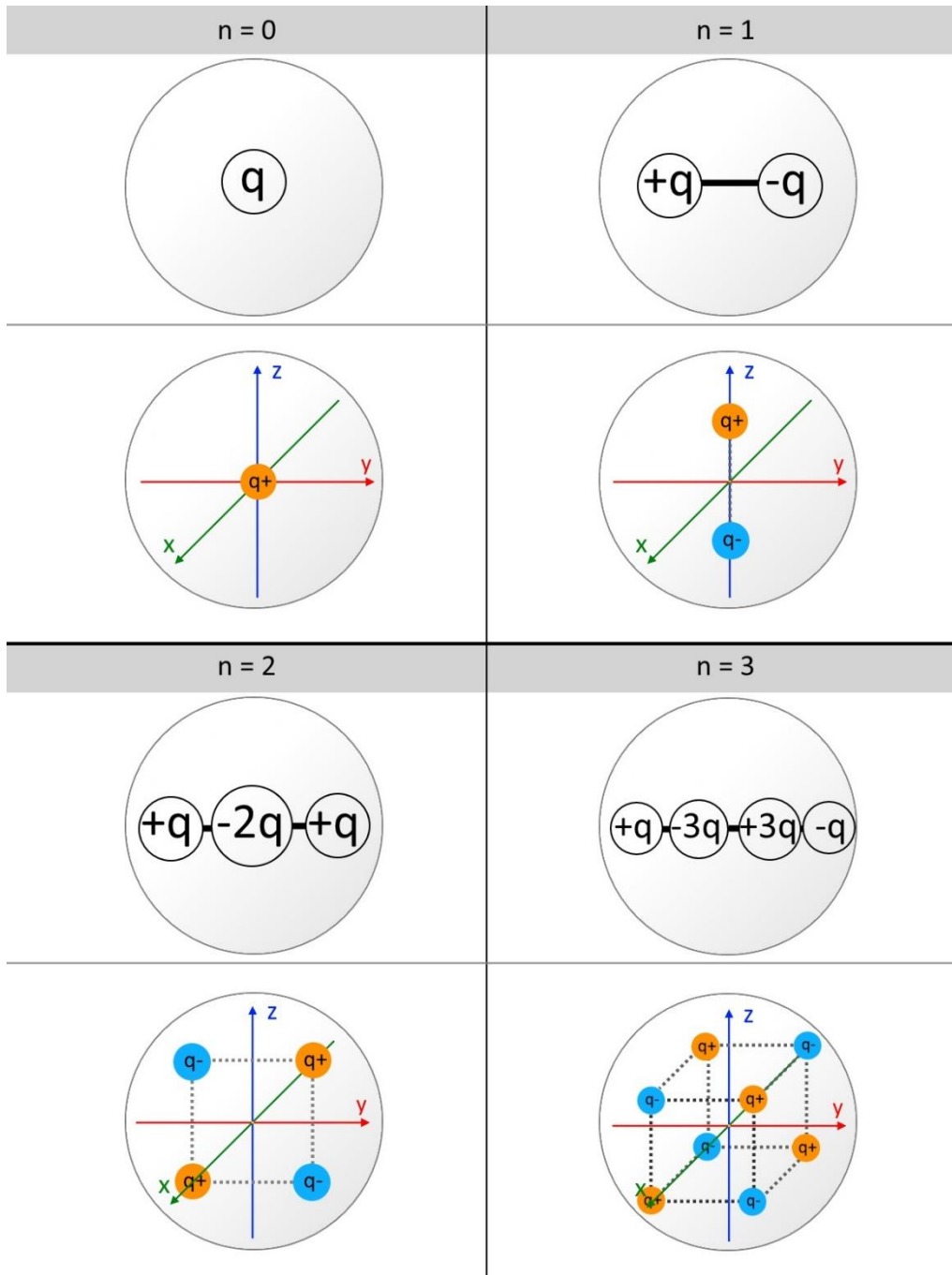


Fig. 2: Graphical representation of the n th multipole moment formed inside a dielectric particle. Moments up to $n=3$ are shown.

As stated by R. Pethig [29], some important remarks can be drawn from eq. (16):

- The DEP force is zero if the field is uniform ($\nabla \mathbf{E} = 0$).
- The DEP force is proportionally dependent on the particle volume, with larger particles experiencing a greater DEP force.
- Depending on whether the particle's permittivity is greater or less than that of the surrounding medium the induced dipole moment is either aligned with or directed against the applied field, respectively. This corresponds to what is defined as positive or negative DEP, depicted in Fig. 3.
 - Positive DEP ($\epsilon_p^* > \epsilon_m^*$): The particle is attracted to regions with high gradient of electric field strength.
 - Negative DEP ($\epsilon_p^* < \epsilon_m^*$): The particle is repelled from regions with high gradient of electric field strength.
- The DEP force depends on the square of the applied field magnitude ($\overline{\mathbf{E}}^2$), indicating that the vector of this force is independent of the type of voltage used to induce the electric field (ac or dc).
- Electrode geometry is an important experimental factor in the control of the factor ($\nabla \overline{\mathbf{E}}^2$), which has dimensions of $\frac{V^2}{m^3}$. For example, a dipole with a factor of $10^{12} \frac{V^2}{m^3}$ can induce a significant DEP force on biological cells ($R_p \sim 10^{-6} m$) using suitably scaled microelectrodes and applied voltages of the order of 1 V.

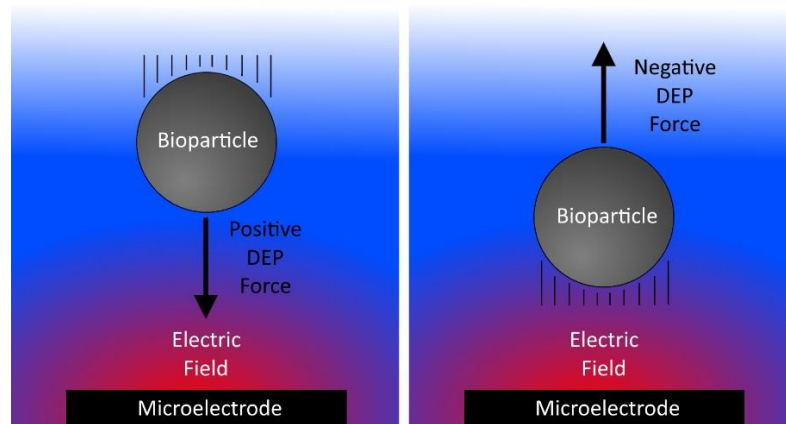


Fig. 3: Positive (left) and negative (right) DEP force exerted on a bioparticle by a microelectrode generating an electric field.

2.2.3 DEP models for bioparticles

The approximation of a particle as a perfect sphere is useful to understand the dielectrophoretic phenomena but it doesn't accurately describe the broad spectrum of bioparticles that we wish to manipulate, living cells in particular.

Simplistically, a living animal cell is composed of organelles, cytoplasm and a cell membrane, as shown in Fig. 4.

One way to adjust eq. (15) to obtain relevant results arises from the application of the so-called multi shell model. This model is used to approximate the geometry of the particle of interest to a group of concentric spheres, among which there is an effective electric permittivity. Using these permittivities, an equivalent permittivity between layers is calculated, bringing the model of the particle closer to the form used to derive the equations used up to now [20]. Equation (17) shows how the equivalent permittivity between layers is calculated.

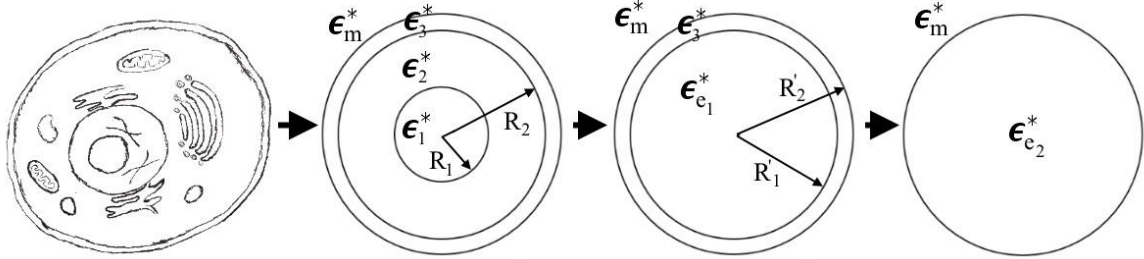


Fig. 4: Living cell and successive approximations to simplify it by the multi shell model.

$$\epsilon_e^* = \epsilon_2^* \left[\frac{\left(\frac{R_2}{R_1}\right)^3 + 2 \frac{\epsilon_1^* - \epsilon_2^*}{\epsilon_1^* + 2\epsilon_2^*}}{\left(\frac{R_2}{R_1}\right)^3 - \frac{\epsilon_1^* - \epsilon_2^*}{\epsilon_1^* + 2\epsilon_2^*}} \right] \quad (17)$$

2.3 FLUID MECHANICS IN A MICROVOLUME

Fluid mechanics is responsible for describing the behavior of a fluid due to the forces acting on it. Its study is useful for microfluidics because the equations that describe the behavior of macroscopic flows can be adapted to include forces that predominate at micro scale [33].

To understand the forces involved in moving a bioparticle suspended in a fluid, we start by describing some fluid properties such as its velocity field, viscosity, boundary conditions that need to be considered and flow regimes. Afterwards, some relationships for an incompressible flow are introduced, including the Navier-Stokes equation which describes the conservation of lineal momentum, which helps to link the effect of the DEP force to the velocity (and motion) of a particle.

2.3.1 Suspended particles in a fluid

A fluid is defined as any substance that is incapable of supporting shear stresses without undergoing a deformation [34]. Fluids are made up of sets of molecules, very separated in gases and closely packed in liquids, which are grouped to form the bulk of the fluid.

Fluids possess and are affected by several properties, which are useful to describe their static and dynamic behavior, such as the velocity field that affects them, their dynamic viscosities and kinematic viscosities. Other thermodynamic properties that affect fluids are pressure, temperature, density, internal energy, entropy, enthalpy, thermal conductivity and specific heat capacities. Brief definitions of dynamic (μ) and kinematic (ν) viscosities are given in Appendix B: Viscosity.

A sufficiently small particle suspended in a fluid acts as part of the fluid, following its motion. Due to this, the following properties and derivations also apply for small suspended particles.

2.3.2 Velocity field

The velocity field of a fluid is arguably its most significant property, because several of its other properties are directly dependent on it [34]. Described by the vector $\bar{\mathbf{u}}(\mathbf{x}, \mathbf{y}, \mathbf{z}, \mathbf{t})$, the velocity field contains the following directional components in tridimensional space:

$$\bar{\mathbf{u}}(\mathbf{x}, \mathbf{y}, \mathbf{z}, \mathbf{t}) = u(\mathbf{x}, \mathbf{y}, \mathbf{z}, \mathbf{t})\hat{\mathbf{i}} + v(\mathbf{x}, \mathbf{y}, \mathbf{z}, \mathbf{t})\hat{\mathbf{j}} + w(\mathbf{x}, \mathbf{y}, \mathbf{z}, \mathbf{t})\hat{\mathbf{k}} \quad (18)$$

Obtaining the time derivative of eq. (18) yields the acceleration vector $\bar{\mathbf{a}}$ of elements inside the fluid.

$$\bar{\mathbf{a}} = \frac{d\bar{\mathbf{u}}}{dt} = \frac{\partial\bar{\mathbf{u}}}{\partial t} + \mathbf{u}\frac{\partial\bar{\mathbf{u}}}{\partial x} + \mathbf{v}\frac{\partial\bar{\mathbf{u}}}{\partial y} + \mathbf{w}\frac{\partial\bar{\mathbf{u}}}{\partial z} \quad (19)$$

2.3.3 Boundary conditions

A characteristic that viscous fluids (fluids with a non-zero viscosity) exhibit is that the velocity of their elements that come in contact with a boundary element (a wall for example) becomes that of said boundary. This is known as the non-slip condition.

Fig. 5 shows an example of the velocity profile of a fluid trapped between two parallel plates, the velocity of the fluid elements is zero for those that are in direct contact with the immobile plate and $\bar{\mathbf{u}}$ for those that are in contact with the moving plate. As a result, the velocity of any fluid element between the two plates becomes a function of its position between them.

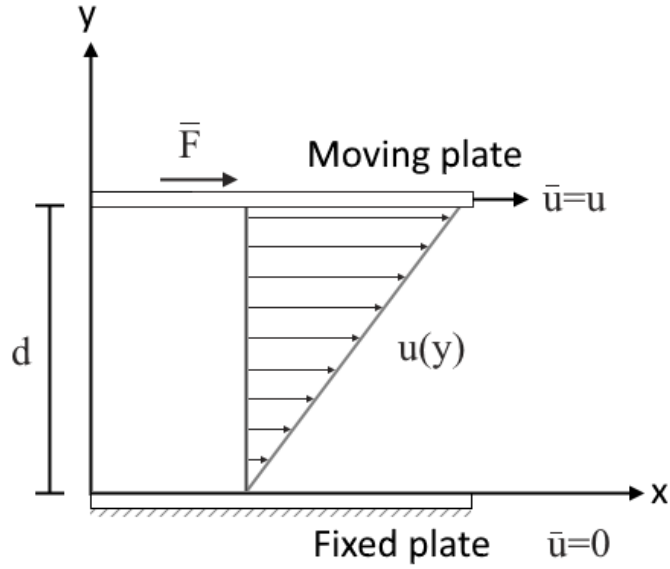


Fig. 5: Velocity profile of a fluid trapped in between a fixed and a moving plate.

The non-slip boundary condition allows us to analyze the way in which the velocity field of a fluid flow between two plates develops. This condition is defined as the non-existence of tangential velocity (\bar{u}_t) of fluid elements that come into contact with an incompressible and impermeable boundary.

$$\bar{u}_t = 0 \quad (20)$$

This condition holds true for most cases, but it may fail if the boundary is built from a hydrophobic material, in which case it is possible to use Navier's model for slipping boundaries (eq, (21)).

$$\bar{u}_t = b \frac{\partial \bar{u}_t}{\partial \hat{n}} \Big|_{\text{boundary}} \quad (21)$$

Where:

\hat{n} = Boundary normal unit vector.

b = Slipping distance.

The slipping distance can be obtained extrapolating the velocity profile of the fluid towards a virtual point inside the boundary where the velocity would become zero, as depicted in Fig. 6.

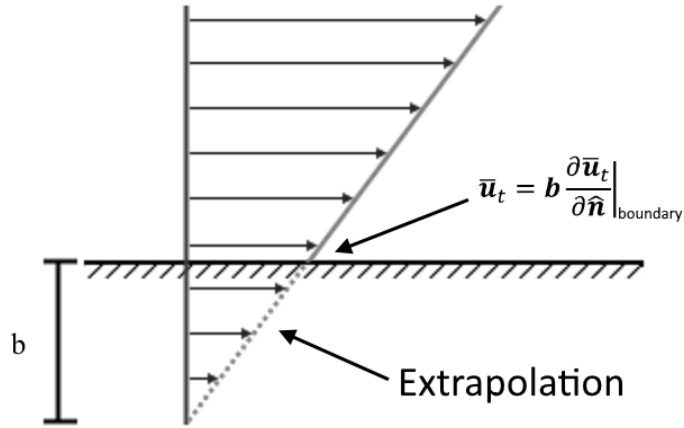


Fig. 6: Navier's extrapolation model for slipping boundaries.

Another condition that exists at the boundary between fluid and an incompressible, inert and impermeable wall is the absence of velocities that develop in the normal direction \bar{u}_n towards the wall, due to the absence of flow through it. This is known as the non-penetration condition.

$$\bar{u}_n = 0 \quad (22)$$

These boundary conditions need to be considered whenever micromanipulation of suspended particles is desired, implying that the particle will become nearly immobile if it contacts a static surface.

2.3.4 Flow regimes

Flow regimes are a way to describe the susceptibility of the fluid to show turbulence, which are chaotic displacements of the fluid particles. Generally, flow regimes can be divided in three main categories: laminar flow, turbulent flow and transitional flow.

In the laminar regime, particles of the fluid move in an orderly manner following well-defined planes, without transitioning from one plane to another.

The particles in turbulent regime do not follow the planes in an orderly way, entering and leaving other planes in a chaotic way.

The transitional regime lies at the border between the laminar and the turbulent regimes, showcasing a flow that is not fully turbulent but cannot be considered laminar. In this regime the particles can follow a laminar behavior for a time but are susceptible to generate turbulences caused by external disturbances.

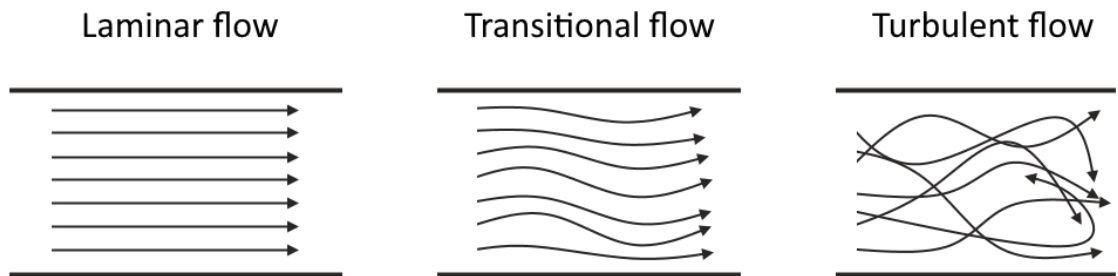


Fig. 7: Example of laminar, transitional and turbulent flow lines.

2.3.4.1 Reynolds number

The Reynolds number (R_e) is an especially useful quantity for the study of fluids, because through it it is possible to know in which flow regime one will work. It depends on the viscosity of the fluid, its density, the magnitude of the flow velocity and the hydraulic diameter of the channel, as shown in eq. (23).

$$R_e = |\bar{u}| \frac{\rho D_H}{\mu} \quad (23)$$

The hydraulic diameter (D_H) is a mathematical figure that helps to involve the geometry of the transport element (pipe, channel, etc.) with the total surface that comes into contact with the fluid. Because of this, the equations developed for circular section of pipes can be taken and applied for almost any cross-section geometry. The hydraulic diameter is defined by eq. (24).

$$D_H = \frac{4A}{P_w} \quad (24)$$

Where:

A = Cross-section area of the transport element.

P_w = Wet perimeter.

The wet perimeter is defined as the sum of all perimeter segments (l_i) of a transversal section of the transport element that contact the fluid.

$$P_w = \sum_i l_i \quad (25)$$

In particular, for a channel with a rectangular cross section of height a and base b , in which the fluid completely fills the cavity, the wet perimeter and hydraulic diameter can be obtained by eq. (26) and eq. (27) respectively.

$$P_w = 2(a + b) \quad (26)$$

$$D_H = \frac{2ab}{a + b} \quad (27)$$

As a convention, it is considered that fluids with a $R_E \leq 2300$ are always in a laminar regime and that fluids with are $R_E > 4000$ in a turbulent regime with the intermediate values belonging to the transitional regime [33].

It is common for flows in microfluidics to have very low Reynolds numbers ($R_E < 1$). Because of this, microfluidic flows are expected to show a laminar behavior for most cases.

2.3.5 Constitutive equations for incompressible flow

A flow is considered incompressible when the variations of the density gradient along the fluid are so small that a uniform density can be assumed for the entire fluid, this can always be considered true for micro fluid flows. The equations that describe this type of flow are the conservation of mass equation and the conservation of linear momentum equation.

2.3.5.1 Conservation of mass

Also known as the continuity equation, it describes the behavior of the flow of matter within the channel. This equation states that the change of mass within a control volume must be equal to the mass flow that enters or exits through the surfaces that enclose it (eq. (28)).

$$\frac{\partial}{\partial t} \int_V \rho dV = - \int_S (\rho \bar{\mathbf{u}}) \cdot \hat{\mathbf{n}} dA \quad (28)$$

Considering a microfluidic flow an incompressible flow, the density within the control volume is constant at all times. Due to this, the first member of eq. (28) becomes zero (eq. (29)).

$$\frac{\partial}{\partial t} \int_V \rho dV = 0 \quad (29)$$

Equation (30) is obtained by solving the surface integral for the second member of eq. (28).

$$- \int_S (\rho \bar{\mathbf{u}}) \cdot \hat{\mathbf{n}} dA = -\nabla \cdot (\rho \bar{\mathbf{u}}) \quad (30)$$

Having a constant density across the fluid allows the simplification to eq. (31).

$$-\nabla \cdot (\rho \bar{\mathbf{u}}) = -\rho(\nabla \cdot \bar{\mathbf{u}}) \quad (31)$$

Finally, substituting these results in the original equation (eq. (28)), we obtain that for incompressible flow the equation of conservation of mass is reduced to eq. (32).

$$\nabla \cdot \bar{\mathbf{u}} = 0 \quad (32)$$

2.3.5.2 Conservation of linear momentum

Better known as the Navier-Stokes equation, it describes the motion of fluids due to the forces that intervene in them (eq. (33)).

$$\frac{\partial}{\partial t} \int_V \rho \bar{\mathbf{u}} dV = - \int_S (\rho \bar{\mathbf{u}} \bar{\mathbf{u}}) \cdot \hat{\mathbf{n}} dA + \int_S \bar{\bar{\boldsymbol{\tau}}} \cdot \hat{\mathbf{n}} dA + \int_V \sum_i \bar{f}_i dV \quad (33)$$

Where:

ρ = Fluid density.

$\bar{\mathbf{u}} \bar{\mathbf{u}}$ = Velocity diadic tensor.

$\hat{\mathbf{n}}$ = Surface normal unit vector.

$\bar{\bar{\boldsymbol{\tau}}}$ = Fluid stress tensor.

From eq. (33), the left member describes the inertial forces, for the right member the first term describes convection forces, the second term surface forces, and the last term involves all the body forces that act on the particles of the fluid, for example the force of gravity or the electrokinetic forces. For an incompressible fluid, the Navier-Stokes equation is simplified to the Cauchy momentum equation (eq. (34)) [33].

$$\rho \frac{\partial \bar{\mathbf{u}}}{\partial t} = -(\rho \bar{\mathbf{u}} \cdot \nabla \bar{\mathbf{u}}) + (\nabla \cdot \bar{\bar{\boldsymbol{\tau}}}) + \sum_i \bar{f}_i \quad (34)$$

For Newtonian fluids, in which the viscosity is considered to be independent of the velocity of the fluid, the viscous stress tensor is proportional to the rate of deformation of the fluid. Consequently, the term $(\nabla \cdot \bar{\tau})$ can be expressed in terms of the pressure gradient of the system and the Laplacian velocity vector [33]. Also, if the viscosity is assumed to be uniform throughout the fluid, eq. (34) is simplified to eq. (35).

$$\rho \frac{\partial \bar{\mathbf{u}}}{\partial t} = -(\rho \bar{\mathbf{u}} \cdot \nabla \bar{\mathbf{u}}) - \nabla P + \mu \nabla^2 \bar{\mathbf{u}} + \sum_i \bar{f}_i \quad (35)$$

Furthermore, if we consider microfluidic flows where the Reynolds number is very low ($R_E \ll 1$), surface forces become predominant and eq. (35) is further reduced to a expression known as the Stokes equation (eq. (36))

$$\nabla P - \mu \nabla^2 \bar{\mathbf{u}} = \sum_i \bar{f}_i \quad (36)$$

Solving eq. (36) for the velocity of a spherical particle of radius R_p in a fluid where the only source of velocity is due to the application of a DEP force (eq. (16)) gives the steady-state velocity of a microparticle being dragged by that DEP force. Using the DEP force due the dipole moment, eq. (37) is obtained.

$$\bar{\mathbf{u}} = \frac{\overline{F_{DEP}}}{6\pi\mu R_p} = \frac{\epsilon_m R_p^2}{3\mu} Re[K] \nabla \bar{E}^2 \quad (37)$$

This equation will be used in posterior sections to estimate the actuation velocity of a suspended particle under the effects of a DEP force.

2.4 MICROELECTRODE ARRAYS FOR DIELECTROPHORETIC MANIPULATION

There are several ways to implement the DEP effect to perform a specific function in a microfluidic chip. The target function depends on the shape of the electrode array used, the type of particles to be manipulated, the characteristics of the applied electric field, the speed with which the particles respond to the effect and the flow velocity of interest, among other factors. Some of these operating strategies and microelectrode types are presented below. Afterwards, some considerations for the micromanipulation of bioparticles are introduced and are used to select the operating strategy and type of microelectrodes to be used in the present work.

2.4.1 Types of operating strategies

We will define an operating strategy as the way the DEP force is used to exert a specific motion on a suspended particle. The operating strategies introduced are pulsed DEP, traveling wave, lateral sorting, immuno-assisted DEP, gravitational field flow fractionation, barrier-assisted DEP, multiple frequency DEP, medium conductivity gradient, marker-specific DEP and electrorotation.

2.4.1.1 Pulsed DEP

A low frequency component (<10 Hz) is added to the DEP signal (> 100 kHz) to intermittently exert a DEP force on the target particle. This causes the particle to travel between two positions within the channel which depend on the flow applied and the susceptibility of the particle to the DEP effect. A particular case of this strategy is the use of on and off cycles instead of a low frequency signal, in order to exert the force at key moments to achieve a desired path of motion [35]–[37].

2.4.1.2 Traveling wave

Motion is induced to the target particles by generating a negative DEP force through the application of a series of alternating current electrical fields temporally offset by 0° , 90° , 180° and 270° from each other. This is achieved by applying a potential difference to a succession of planar electrodes. The electric potential is temporally offset by 90° with respect to the previous and next electrodes, so that the moment experienced by the particle has a component parallel to the electrodes plane [38], [39].

2.4.1.3 Lateral sorting

Particles with different dielectric properties are exposed to an applied electric field by means of electrodes that direct them to a specific area within the microfluidic channel. Their final position depends on the size of the particle, its dielectric properties and the relationship between the applied DEP force and the drag generated by the flow used. It is known as lateral sorting because the application of a DEP force moves the particles to lateral flow lines located on the sides of the original flow line from which they moved [40], [41].

2.4.1.4 Immuno-assisted DEP

This strategy is used mainly to improve the selectivity and rapid separation of particles in fast flows. The surface of the electrodes is covered by a layer of an active substance that reacts with the target particle and fixes it to the electrode.

By applying a positive DEP force to a flow of particles that passes over the activated electrodes, an attractive force is induced between the target particles and the electrodes, which leads them to the surface of these. When target particle comes into contact with the active substance it gets trapped. This strategy helps to improve the selectivity of the DEP effect for separation due to the addition of a chemical element (active layer), in addition to the electrical element (dielectric properties) to the discrimination factors for the capture of particles [42], [43].

2.4.1.5 Gravitational field flow fractionation (FFF)

By using gravitational FFF, the particles are pushed in the direction normal to the electrodes by a negative DEP force. The particles are positioned in flow lines at heights corresponding to their weight and their electrical properties, because particles with different properties experience a different DEP force, with which they are dragged by the flow at speeds corresponding to the parabolic profile of the flow through the channel. This scheme is mostly useful for separation purposes [44], [45].

2.4.1.6 Barrier-assisted DEP

Barrier-assisted DEP is a strategy used for the capture of particles. It uses the geometry of structures deliberately placed in the channel for that purpose. The objective is to create zones of very low flow velocity within the channel and to position the desired particles in them by means of the DEP effect. By the no-slip condition, in zones close to the barriers the particles acquire very low speeds that effectively leave them immobile in their position [46].

2.4.1.7 Multiple frequency DEP

In multiple frequency DEP, the separation of different types of particles is achieved by using several electric fields at different frequencies at the same time. The total DEP force experienced by each particle and its final position result from the geometric sum of the contributions of each field and the positions of the electrodes that generate them. Using this strategy, groups of particles with susceptibilities very similar to the effect can be placed in well-defined areas of the channel [47].

2.4.1.8 Medium conductivity gradient

The DEP force depends on the Clausius - Mossotti factor, which is a measure of the polarizability of the particle with respect to the surrounding environment. This factor depends on the difference between the electrical permittivity and conductivity of both particle and medium. The greater this difference, the greater the DEP effect. One way to control the DEP force on the particle comes from varying the electrical conductivity of the medium in which it is immersed. This strategy is known as medium conductivity gradient assisted DEP.

Groups of particles can be separated by modifying the conductivity of the medium to reduce the effect of the force induced on them, to the point where the drag force of the flow is greater than the DEP force that traps them. The above can be achieved by modifying the chemical concentrations of the aqueous medium or temporarily replacing it [48].

2.4.1.9 Marker-specific DEP

In marker-specific DEP, one or several particles are marked by means of a substance that alters the DEP force that is exerted onto them, allowing them to be mixed with other unlabeled particles and subsequently recovered by means of DEP for a post experiment analysis [49].

2.4.1.10 Electrorotation

A rotational force is induced to a particle by set of four electrodes in which the electrical signals are applied 90° out of phase with respect to each other. The particle tries to align with the electric field that is rotating around it, therefore causing it to rotate. The torque experienced by the particle is counteracted by the viscosity of the surrounding medium. Due to this, the angular velocity that it experiences becomes a function of the DEP force and viscoelastic forces. This strategy is used mainly to characterize the particle's electrical properties involved in the Clausius-Mossotti factor [20], [36], [50].

2.4.2 Microelectrode geometries for particle micromanipulation

There are several ways to implement a set of electrodes that allow the use of DEP to manipulate particles in a microfluidic channel. The possible geometric designs are almost unlimited, as has been proven by the large number of applications developed in the literature [51]. However, it is possible to categorize most of the designs in some easily identifiable types based in their predominant geometric shapes.

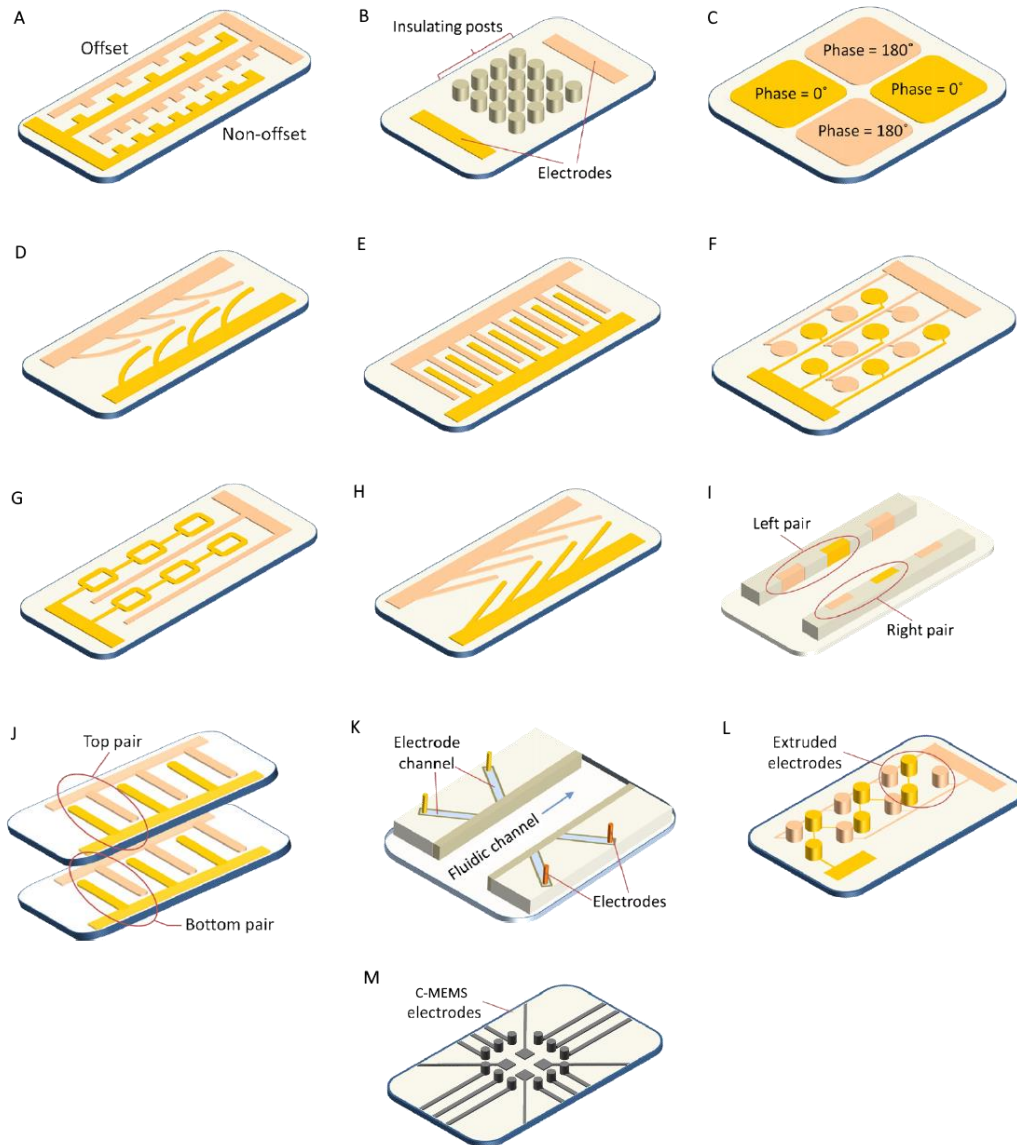


Fig. 8: Microelectrode geometries for DEP micromanipulation [51]. (A) Castellated, (B) Insulator-based, (C) Quadrupole, (D) Curved, (E) Interdigitated, (F) Matrix, (G) Microwells, (H) Oblique, (I) Sidewall patterned, (J) Top-bottom patterned, (K) Contactless, (L) Extruded and (M) 3D C-MEMS.

2.4.2.1 A) Castellated

The castellated geometry consists of electrodes with a trident-shaped pattern that repeats throughout the electrode. To achieve the DEP effect, at least two electrodes are placed with these characteristics separated from each other, with their teeth in line or off-set from one another. This type of arrangement allows the capture of particles on relatively large surfaces and with moderate to high flows using negative DEP [4], [7], [36], [37], [52]–[56].

2.4.2.2 B) Insulator-based

A set of microstructures are placed to limit the flow of particles in the microfluidic channel. A pair of electrodes, each at one end of the channel and with the insulating microstructures in between, are responsible for generating the electric field that induces the DEP force to the particles. The DEP force acts as the only mechanism of movement in the system, whereby the affected particles move from their initial position aligned with the electric field, until they meet some of the insulating barriers. When this happens, if the particle meets the wall of the barrier, they become trapped due to the non-slip condition near walls, against which the DEP force is insufficient to continue moving them. Therefore, the insulator-based geometry is mainly employed for trapping particles [6], [57]–[60].

2.4.2.3 C) Quadruple

The quadrupole geometry uses four electrodes distributed equidistantly around a focal point to exert a DEP force. This type of arrangement is mainly used to generate electrorotation in particles of interest to perform the characterization of their electrical properties [10], [11], [61]–[63]. Its application to generate levitation forces in particles using multipole moments of higher order has also been studied [64].

2.4.2.4 D) Curved

This geometry consists of a set of planar elongated electrodes with a curved profile, placed like a funnel in such a way that they cover the width of the microfluidic channel. This allows the electric field to affect the target particles at any point along the width of the channel and direct them to a flow line centered at the midpoint between the closest end of the electrodes, which could be interpreted as the neck of the funnel [21], [39], [41], [46], [65], [66].

2.4.2.5 E) Interdigitated

Interdigitated electrodes are characterized by having successive rows of planar electrodes in the form of crossed fingers. This configuration of electrodes is versatile, allowing to implement of strategies such as gravitational FFF, barrier-assisted DEP, traveling wave, pulsed DEP and medium conductivity gradient [8], [43], [45], [67]–[69].

2.4.2.6 F) Matrix

This type of arrangement is formed by a set of planar electrodes distributed in a rectangular area of interest in the chip. These electrodes are usually individually addressable (programmable) which allows the user to control the vector on which the DEP force is exerted. The matrix geometry is used mainly in conjunction with pulsed DEP to manipulate the position of individual particles on the array [13], [70], [71].

2.4.2.7 G) Microwells

The microwell arrangement uses square or circular structures as planar electrodes where their central parts are hollow in the sense that they have absence of conductive material at their geometric center. They are generally used in conjunction with negative DEP force (nDEP), which repels the particle away from the electrodes that induce it, to produce virtual wells of electrical potential that confine one or a small group of particles at the geometric center of the electrode. This geometry can also be used in conjunction with positive DEP force (pDEP) to attract a target particle to a physical well (micro structure manufactured on the chip) to get it mechanically trapped. This type of arrangement is especially useful for pulsed DEP trapping strategies [9], [72]–[75].

2.4.2.8 H) Oblique

Oblique electrodes are planar electrodes that are so named because they have an oblique angle with respect to the direction of movement of the particles on which the DEP force acts. They are used to perform particle separation by means of lateral ordering [40], medium conductivity gradient [48], marker-specific differentiation [49] or FFF [76].

2.4.2.9 I) Sidewall patterned

Current microfabrication techniques allow the generation of conductive structures embedded in the walls that make a microfluidic channel. The main use of this type of electrodes is the separation of particles by means of lateral ordering [44], [77], [78].

2.4.2.10 J) Top-bottom patterned

This arrangement consists of pairs of electrodes positioned at the top and bottom of the microfluidic channel. Top-bottom geometries are useful for strategies such as lateral ordering [79]–[81], pulsed DEP [42] or FFF [82].

2.4.2.11 K) Contactless

As the name implies, contactless electrodes are characterized by not coming into direct contact with the fluid or the suspended particles. The main advantages of this geometry are less wear due to corrosion, and zero chance of cross contamination between electrode and medium due to electrochemical reactions at the electrode-electrolyte interface. The main disadvantage of these electrodes is the need to use high-voltage high-frequency electrical systems (for example, 250 V_{rms} at 200 kHz [83]). The electric potential needed to exert DEP force with contactless electrodes is much greater than that needed with electrodes that come into contact with the fluid (for example 3 V at 1 MHz [53]). For an electric field strong enough to generate the DEP effect, the potential must overcome the dielectric barrier introduced by the material used to separate the electrode from the electrolyte. The strategy of choice for contactless electrodes is pulsed DEP [83], [84].

2.4.2.12 L) 3D or extruded

Up to now, the electrode geometries discussed possess low aspect ratios, that is, they have big areas compared to their height. The 3D or extruded electrode geometry is obtained by increasing the height of these previous geometries, obtaining structures with higher aspect ratios. Extruded electrodes have been used successfully in the manufacture of tridimensional matrices for the selective capture of particles, manipulation of the position of groups of particles, and the simultaneous application of a DEP-induced flow and particle sorting device [85]–[87].

One of the main advantages of 3D electrodes is their ability to exert a DEP force with electric potentials similar or lower to planar electrodes while increasing system performance and reducing possible sources of damage to the target particles [2].

The challenges of generating this kind of electrodes involves the fabrication of conductive microstructures with high aspect ratio. Traditional microfabrication of metallic high aspect ratio electrodes has proven to be complex and time consuming. This has driven the search for manufacturing alternatives to continue exploring the benefits offered by this versatile type of electrodes, one such alternative being carbon based microelectromechanical systems [88]–[91].

2.4.3 Carbon-based microelectromechanical systems (C-MEMS)

Carbon-based microelectromechanical systems (C-MEMS) is an emerging technology for the fabrication of microelectrodes that use the carbon atoms present in various materials (carbon precursors) for the manufacture of micro structures.

Recently, photoresists have been used as the carbon precursors for this technology [92], [93]. The combination of photolithography processes of the photoresists with pyrolysis in inert atmospheres has been used to easily fabricate carbon microstructures that have high aspect ratios [88], that are biocompatible [94], electrochemically stable and of low cost [95].

Although this technology can be used to fabricate most of the microelectrode geometries, it is of special use for the easy fabrication of biocompatible 3D electrodes. C-MEMS technology solves two of the mayor drawbacks of the fabrication of 3D microelectrodes: their usual complex fabrication procedures, and the lack of biocompatibility of the final device due to material incompatibility or process contamination.

In short, the manufacturing process of C-MEMS involves:

1. Deposition of a photoresist with high carbon content on a substrate that supports the temperatures of the pyrolysis process ($\sim 1000\text{ }^{\circ}\text{C}$).
2. Patterning of the photoresist by means of photolithography.
3. A pyrolysis process is carried out at high temperatures ($\sim 1000\text{ }^{\circ}\text{C}$). During this process most of the other elements present in the photoresist are evaporated, leaving only carbon structures on the substrate.

Pyrolysis is the process of thermal decomposition of a material at high temperatures without combustion. Combustion is prevented by using an inert atmosphere. The temperature needed for the decomposition depends on the material. Finally, once the pyrolysis temperature is achieved, the decomposition continues until the remaining molecules of the material are insensitive to the temperature of the process. This process usually only leaves carbon due to the high temperature.

The potential to obtain complex 3D micro structures using C-MEMS is evident because it is possible to deposit several layers of photoresist with different patterns by means of photolithography in order to obtain intricate geometries [91], [96]. An example of microstructures fabricated with this technology is shown in Fig. 9.

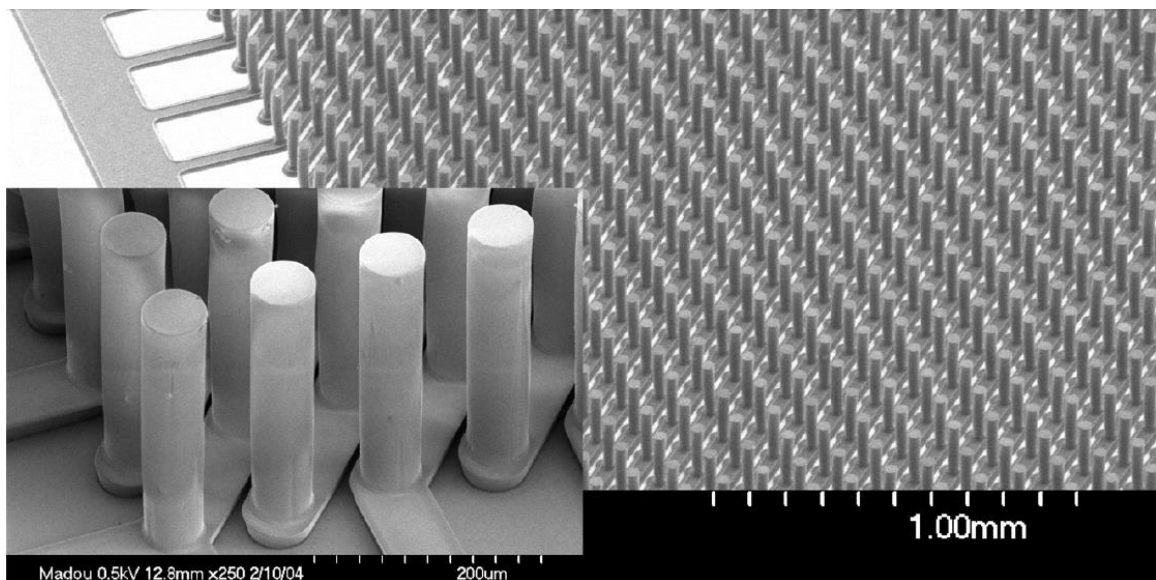


Fig. 9: High aspect ratio microstructures fabricated with C-MEMS technology [97].

Another technique for obtaining complex structures from a single layer of resin consists in the application of different doses of radiation during photolithography, either using multiple exposures of slightly different masks in the same layer [96], changing the dose in specific sections of the layer by means of optical systems or using optical lithography combined with gray-scale devices to achieve this effect [98]–[100].

Furthermore, another important result is the conductivity of the carbon micro structures. This property has proven to be dependent on the temperature at which pyrolysis takes place [101], [102]. By increasing the temperature of the pyrolysis graphitization of the carbon structure is improved, which results in an increase to the conductivity of the material.

The electrochemical properties of carbon structures produced with this process have been studied extensively by J. Kim et. al. [101]. It was found that after pyrolysis the carbon structures are similar to glassy carbon, that is, structures tend to be electrochemically stable. Another observation of this technology is that there is a loss of mass greater than 50% with respect to the mass of deposited photoresist. To accommodate this loss of mass the microstructures shrink. This change of volume was recently characterized by Natu et. al. [103]. The resulting carbon microstructures usually have smooth surfaces with relatively small pores and a structure that resemble that of amorphous carbon [101].

In addition, recently efforts have been made to tailor the type of carbon obtained from pyrolysis. In collaboration with the UCI BioMEMS group, I participated in a study that showed that by using mechanical treatments to stress the carbon precursor before it was pyrolyzed, it was possible to enhance the graphitic nature of the obtained carbon [104]. This readily showed the versatility of C-MEMS technology for the fabrication of 3D microelectrodes.

2.4.4 Considerations for the micromanipulation of bioparticles

While all the operating strategies and electrode configurations discussed previously allow the generation of the dielectrophoretic phenomenon applied to particles, some considerations must be met for a platform that seeks their use for the micromanipulation of the position of bioparticles in a microvolume:

- Operating strategy and microelectrode geometry must not affect bioparticle viability.
- The operating strategy must allow fast and precise manipulation of the position of groups or single particles.
- Microelectrode geometry must be able to generate DEP force without the need of high electric potentials in vectors that allow the precise movement of particles in a tridimensional fashion. That is, the electrode array must be programmable in the sense that it should allow the assignation of specific electric potentials to each electrode.
- Microelectrode geometry must be biocompatible after fabrication.

Table I summarizes bioparticle viability, quickness of response of the manipulation strategy and if the strategy allows manipulation of particle positioning for the operating strategies introduced in section 2.4.1. Strategies that met all our criteria are highlighted.

Table I: Relevant characteristics of the different DEP operational strategies [51].

Operating strategy	Bioparticle viability	Manipulation response	Allows manipulation of particle position?
Pulsed DEP	Viable	Fast	Yes
Traveling wave	Viable	Fast	Yes
Lateral sorting	Viable	Fast	Yes
Immuno-assisted DEP	Viable	Slow	No
Gravitational FFF	Viable	Slow	No
Barrier-assisted DEP	Viable	Fast	No
Multiple frequency DEP	Viable	Fast	Yes
Medium conductivity gradient	Non-viable	Fast	Yes

Marker-specific DEP	Viable	Fast	Yes
Electrorotation	Viable	Fast	No

Table II shows a comparison between the microelectrode geometries introduced in section 2.4.2. Fabrication complexity, electric potential required to generate DEP effect, individual programmability of the microelectrodes and ability to affect single bioparticles were compared. Strategies that met all our criteria are highlighted.

Table II: Relevant characteristics of microelectrode geometries for DEP particle micromanipulation [51].

Microelectrode geometry	Fabrication	Electric potential required	Programable	Enables single cell analysis?
Castellated	Simple	Small	No	No
Insulator-based	Simple	Small	No	No
Quadrupole	Simple	Small	No	Yes
Curved	Simple	Small	No	No
Interdigitated	Simple	Small	No	No
Matrix	Simple	Small	Yes	Yes
Microwell	Simple	Small	No	Yes
Oblique	Simple	Small	No	No
Sidewall patterned	Complex	Small	No	No
Top-bottom patterned	Simple	Small	No	No
Contactless	Simple	Large	No	No
Extruded	Complex	Small	Yes	Yes
3D Carbon MEMS	Simple	Small	Yes	Yes

Using Table I and Table II information, it was decided that a combination of planar and 3D matrix C-MEMS electrodes would be ideal to address the needs of the micromanipulation platform. Pulsed DEP was chosen as the operating strategy due to its compatibility with the chosen geometries allowing temporal control for the application of the DEP force.

Conceptual schematics of the proposed geometry and operation of the platform are given in Fig. 10 and Fig. 11. Using pulsed DEP between 3D electrodes would allow movement of a target bioparticle parallel to the substrate, while pulsed DEP between the planar electrodes and a top counter electrode would allow movement normal to the substrate.

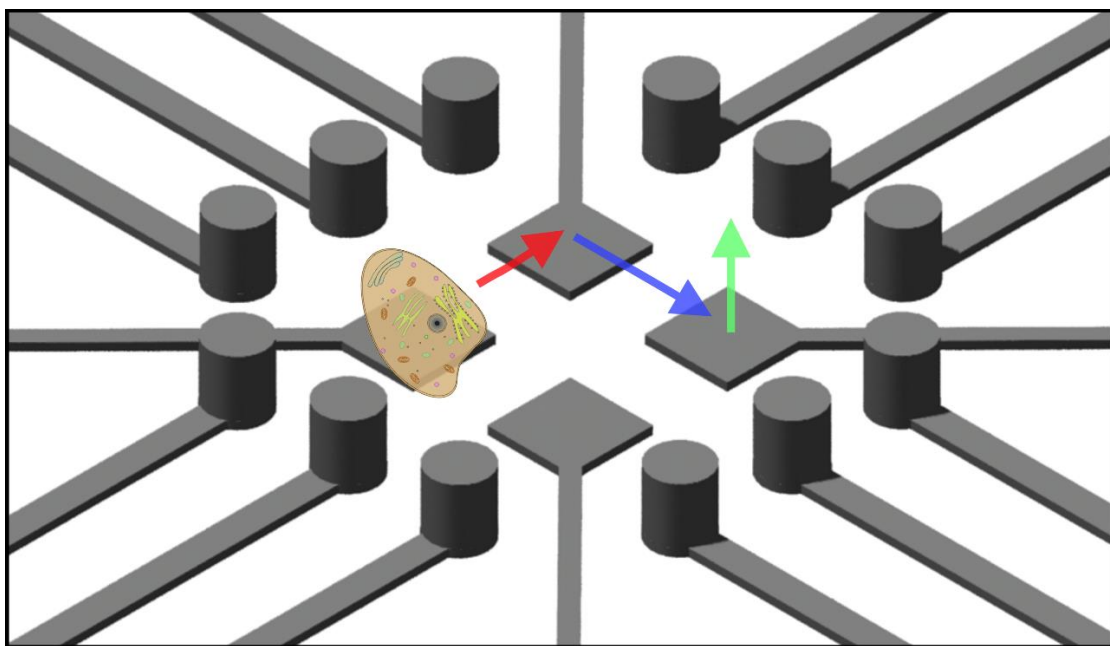


Fig. 10: Combination of planar and 3D C-MEMS microelectrodes. Using pulsed DEP between 3D electrodes for movement parallel to the substrate, and pulsed DEP between planar electrodes and a top counter electrode for movement normal to the substrate.

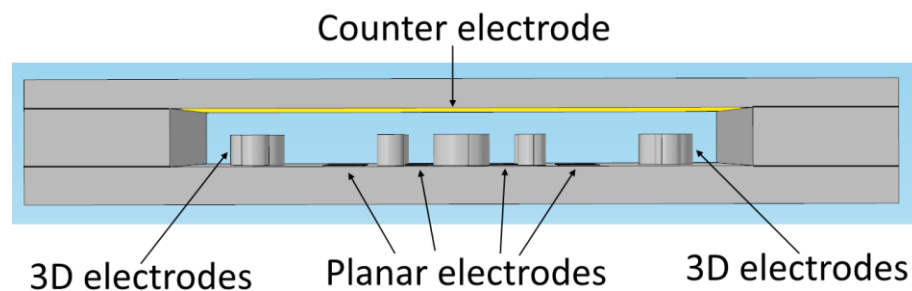


Fig. 11: Lateral view of the proposed design.

3 MICRO PLATFORM DESIGN AND FABRICATION

In this section, the design process and fabrication of a series of modules that form the micro platform for the manipulation of bioparticles using DEP is described.

First, design goals for the platform are established, such as microvolume and bioparticle sizes, flow conditions and magnitude of electric potential for DEP effect.

Secondly, the micro-platform will be broken down in modules for their individual design and fabrication. It was concluded that three main modules were necessary: a microelectrode array, a microfluidics chip and a control electronics board.

3.1 DESIGN GOALS

Following the proposed platform described in section 2.4.4 several variables need to be constrained to design an effective micro-platform:

- Bioparticle sizes to be manipulated.
- Magnitude and frequency of the electric potential needed to induce DEP.
- Volume size in which the microelectrodes can effectively manipulate the target particles.

First, the intended use of this platform is for the micromanipulation of bioparticles. As stated before, there are many types of biological particles which range in sizes from hundredths of micrometers (for example, egg cells) to the nanometers (for example, DNA). For the present work, bioparticle size will be constrained to the size range of a widely studied bioparticle: the mammalian cell (10-30 μm) [105]. Furthermore, due to the exploratory nature of this work polystyrene particles will be employed as a substitute of real cells for testing the micro platform.

To obtain the magnitude of the electric potential needed to induce DEP, an analysis of eq. (37) from section 2.3.5.2 is needed:

$$\bar{u} = \frac{\epsilon_m R_p^2}{3\mu} \text{Re}[K] \nabla \bar{E}^2 \quad (37)$$

For simplicity, the following parameters will be used for the estimations:

- Particles (Polystyrene microparticles)
 - Density $\rho = 1040 \frac{\text{kg}}{\text{m}^3}$
 - Diameter $\phi = 10 \mu\text{m}$
 - Electrical conductivity $\sigma_p = 6.7 \times 10^{-14} \frac{\text{S}}{\text{m}}$
 - Electrical permittivity $\epsilon_p = 2.6$
- Medium (Deionized water)
 - Electrical conductivity $\sigma_m = 5 \times 10^{-6} \frac{\text{S}}{\text{m}}$
 - Electrical permittivity $\epsilon_m = 80$
 - Dynamic viscosity $\mu = 8.9 \times 10^{-4} \text{Pa s}$

Solving eq. (37) for the electric field using a reasonable velocity inside a microvolume ($10^{-5} \frac{\text{m}}{\text{s}}$), a field strength in the order of $|\nabla \bar{E}^2| \sim 10^{12} \frac{\text{V}^2}{\text{m}^3}$ is obtained. This is comparable to previous magnitude analysis of the forces involved in DEP experiments [106]. Using an approximation for planar and parallel electrodes [107], this field strength can be obtained with microelectrode areas ranging from $10^{-10} - 10^{-8} \text{m}^2$ separated by gaps ranging $10^{-5} - 10^{-4} \text{m}$, up to a height above them of 10^{-4}m , and with applied voltages in the range of 1 to 20 V.

In brief, the effective microvolume for manipulation, magnitude of the electric potential for DEP and microelectrode quantity are coupled parameters. For a fixed number of electrodes, the bigger the intended microvolume is desired, the larger an electric potential will be needed to induce DEP in the target particles. Trying to maximize the volume for manipulation, the parameters shown in Table III are proposed for the micro-platform.

The frequency of the applied electric potential is largely determined by two factors: medium electrolysis and the Clausius-Mossotti factor. Aqueous media undergo hydrolysis at DC voltages above 1.23 V. This process generates bubbles at the electrode-electrolyte interface that can potentially damage the structure. This forces the use of an AC signal.

The frequency of the AC signal can be obtained by solving eq. (10) for a common range of DEP frequencies ($10^5 - 10^7$ Hz) and picking the one that maximizes the absolute value of the Clausius-Mossotti factor. It was found that for the proposed particles and medium the Clausius-Mossotti factor takes an approximate value of -0.5 for all the frequency range. A computer program was used to calculate this value (Appendix G: MATLAB programs). This corresponds to negative DEP. Since the DEP force will be constant in this range of frequencies, a middle value of 10^6 Hz will be employed.

Table III: Proposed design parameter for the micro-platform.

Parameter	Value - magnitude
Particle size (diameter)	$1 - 10 \mu m (10^{-6} - 10^{-5} m)$
Microvolume for manipulation	$100 \mu m \times 100 \mu m \times 100 \mu m$
Microelectrode area	$10^2 \mu m^2 (10^{-10} m^2)$
Microelectrode gap	$10 \mu m (10^{-5} m)$
Applied electric potential	$5 - 20 V$
AC signal frequency	$1 MHz (10^6 Hz)$
Particle velocity	$10 \frac{\mu m}{s} (10^{-5} \frac{m}{s})$

3.2 MICRO PLATFORM MODULES

The design goals defined above can be met by designing three independent modules that compose the micro platform. These modules are:

1. Microelectrode array: Contains the combination of planar and 3D microelectrodes that exert the DEP force.
2. Microfluidic chip: Contains the bioparticles and medium in which they are suspended. Interfaces with the microelectrode array module to enclose the microvolume for manipulation.
3. Control electronics: Allows the selection of individual microelectrodes and the application of the DEP electric potential. It is composed of an electronics board that interfaces with the microelectrode array module, and a control software that allows the electrical control of each microelectrode through a friendly graphic user interface.

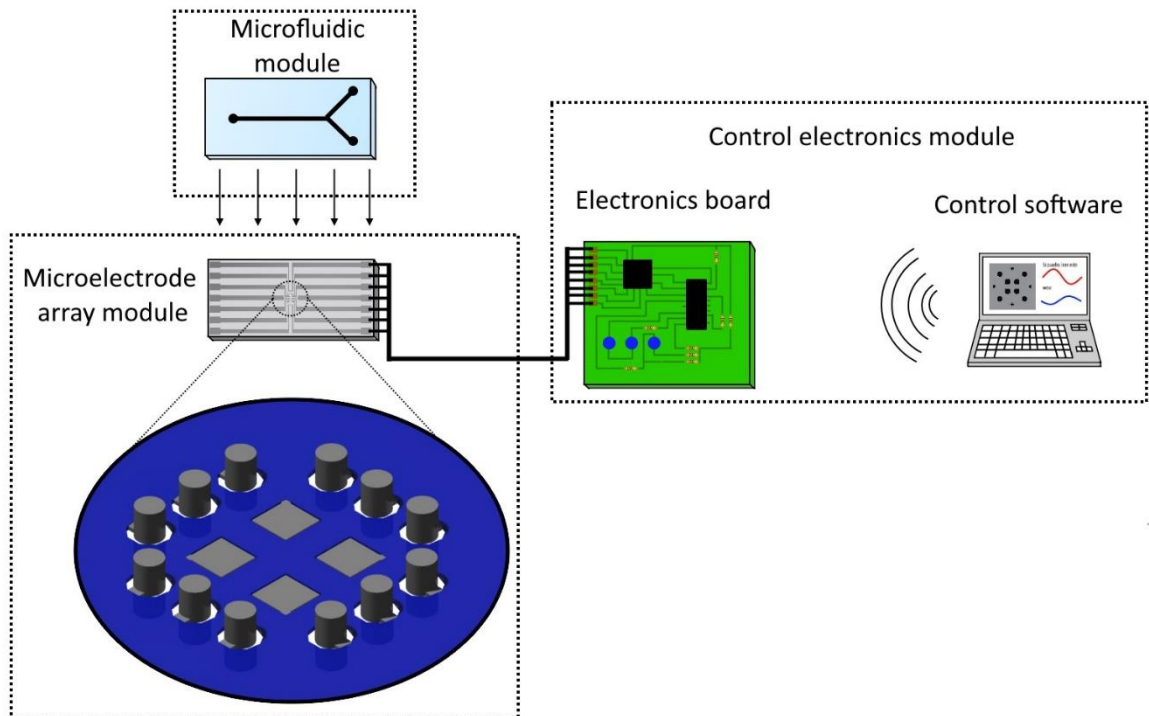


Fig. 12: Modules that conform the micro platform for manipulation of bioparticles.

3.2.1 Microelectrode array

3.2.1.1 Microelectrode array type and working principle

A combination of planar (2D) and 3D C-MEMS electrodes were selected to make the microelectrode array that will exert the DEP force, shown in Fig. 13. From equation (37) we know that the vector of movement of a suspended particle moved only by a DEP force will be collinear with the vector of this force. Therefore, we can distribute 3D microelectrodes at the boundaries of the control microvolume to move the particles along the x-axis and y-axis, while 2D electrodes placed at the bottom and a counter electrode placed at the top of the control volume can move the particles in the z-axis direction. Admittedly, this holds true if we only consider the force exerted due to the dipole moment. Multipole moments of higher order can deflect the particle movement. Fortunately, it is possible to compensate for this inconvenience by continuously pulsing the DEP force and smartly changing the selected pairs of microelectrodes, so that overall the particle moves as desired.

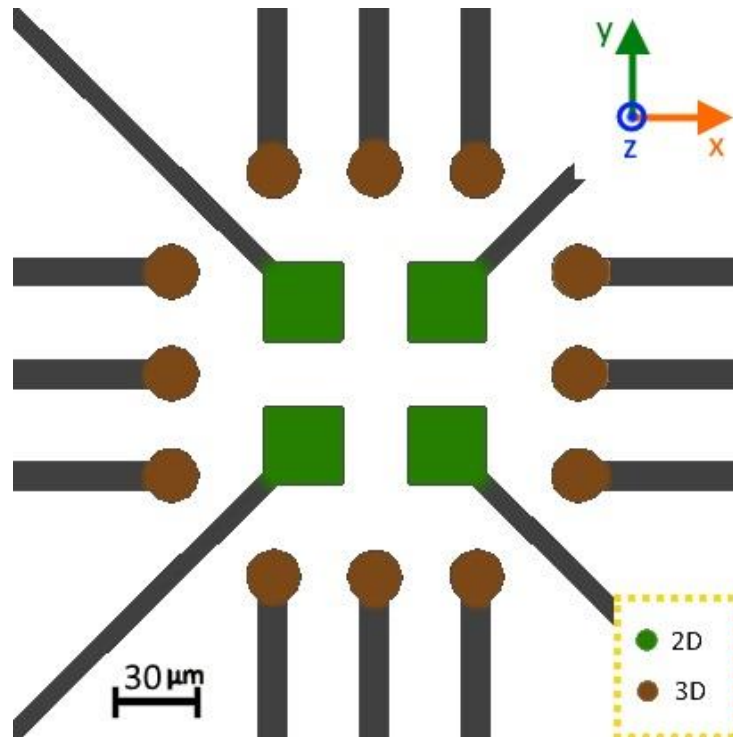


Fig. 13: Conceptual design for microelectrode type and placement. 3D electrodes control x-axis and y-axis movement while 2D electrodes and a top counter electrode control z-axis movement.

3.2.1.2 Prototype design and fabrication

Multiple iterations of the conceptual design shown in Fig. 13 were tested for fabrication with the photolithography protocol described in Appendix C: Microelectrode array – Photolithography.

Fig. 14 shows the evolution of the design. There were several fabrication challenges that needed to be addressed in each revision of the design. We now summarize the main development findings:

- a. Too complex for fabrication, footprint of the design exceeded the dimension of the pyrolysis chamber. 28 electrodes.
- b. Simplified version. 16 electrodes. Some traces were found problematic to fabricate due to bounding to adjacent traces (not enough clearance between traces).
- c. Introduced the use of angled traces to improve clearance between traces.
- d. Scaled revision with final electrode shapes. Control volume constrained to target $100\ \mu\text{m} \times 100\ \mu\text{m}$. Electrode shapes chosen to aid in the generation of nonuniform fields: squares for 2D electrodes, and cylinders and pikes for 3D electrodes. Clearance between traces was found to be insufficient for fabrication.
- e. Simplified version. 12 electrodes. Traces were found adequate for fabrication.
- f. Final design. Electrical traces redistributed and resized. Improved the separation between traces.

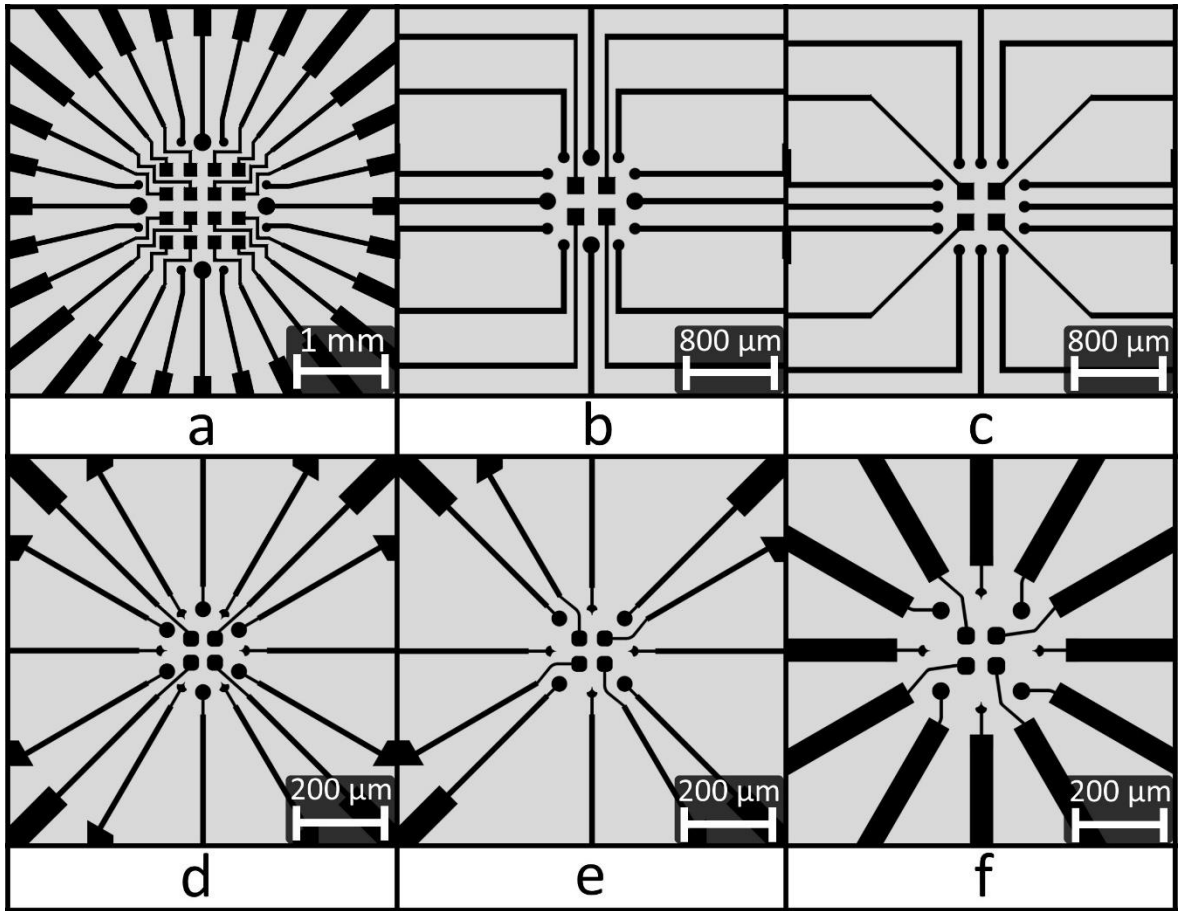


Fig. 14: Design evolution of the microelectrode array. Ordered from earliest (a) to latest (f) with f being the final design used in the micro platform.

Fabrication of the microelectrode array was performed in a multi-layer photolithography process using SU-8 photoresist on a fused silica substrate.

The use of SU-8 2035 and SU-3035 was explored. Our findings are summarized in Appendix I: Article “Methodology and Fabrication of Adherent and Crack-free SU-8 Photoresist-derived Carbon MEMS on Fused Silica Transparent Substrates”. In short, Fused silica was chosen as the substrate material due to its ability to withstand pyrolysis temperatures ($\sim 1000\text{ }^{\circ}\text{C}$) and optical transparency, allowing devices built in this type of substrate to be observed with transmitted light microscopy instruments. SU-8 3035 was chosen because it yields well-adhered crack-free carbon microstructures after pyrolysis.

The microelectrode design was divided in five layers:

1. Electrical traces and pads
2. 2D and 3D microelectrode bases
3. 3D microelectrodes
4. Passivation
5. Microchannel

After the deposition and photopatterning of layers 1 through 3, a pyrolysis process was employed to obtain the carbon microelectrodes. Two pyrolysis atmospheres were explored for the fabrication of the carbon microelectrodes: forming gas (95% Nitrogen / 5% Hydrogen), and 4 mTorr Vacuum. Although both processes yielded carbon microstructures, the vacuum process was selected for the fabrication of the final prototype due to its simplicity compared to the forming gas process.

Afterwards, layer 4 was deposited to passivate the electrical traces so that only the microelectrodes could contact the medium with particles. Layer 5 was added to contain said medium and to protect the extruded 3D microelectrodes against unintentional mishandling of the C-MEMS chip.

Finally, the C-MEMS chip was mounted in an electronics interface board that enabled a convenient nonpermanent electrical connection between the microelectrode array and the control electronics module. Photographs and further metrology of this module can be found in section 4.1.

Comprehensive schematics of each layer of the final design, photolithography and pyrolysis procedures, and schematics of the interface board can be found in Appendix C: Microelectrode array.

3.2.1.3 Finite element simulations of the proposed design

A finite element simulation software (COMSOL 5.1) was used to simulate particle movement inside the designed microelectrode array due to an induced DEP force. Also, electric field intensity was obtained. Element properties were defined using the following values:

- Particles (Polystyrene microparticles)
 - Density $\rho = 1040 \frac{kg}{m^3}$
 - Diameter $\phi = 10 \mu m$
 - Electrical conductivity $\sigma_p = 6.7 \times 10^{-14} \frac{S}{m}$
 - Electrical permittivity $\epsilon_p = 2.6$
- Medium (Deionized water)
 - Electrical conductivity $\sigma_m = 5 \times 10^{-6} \frac{S}{m}$
 - Electrical permittivity $\epsilon_m = 80$
 - Dynamic viscosity $\mu = 8.9 \times 10^{-4} Pa s$
- Electric signal applied
 - Electric potential $V_{DEP} = 5 V$
 - Signal type = sine
 - Signal frequency $f = 1 MHz$

The following figures show electrodes with an applied DEP voltage colored in red-orange, grounded electrodes are shown in blue and non-connected electrodes are left transparent.

Electric field (Fig. 15) and particle movement (Fig. 16) were simulated for multiple combinations microelectrodes. It was observed that despite the gradient being maximum closer to the electrodes, a sufficiently strong DEP force to move the microparticles inside the whole microvolume was still obtained.

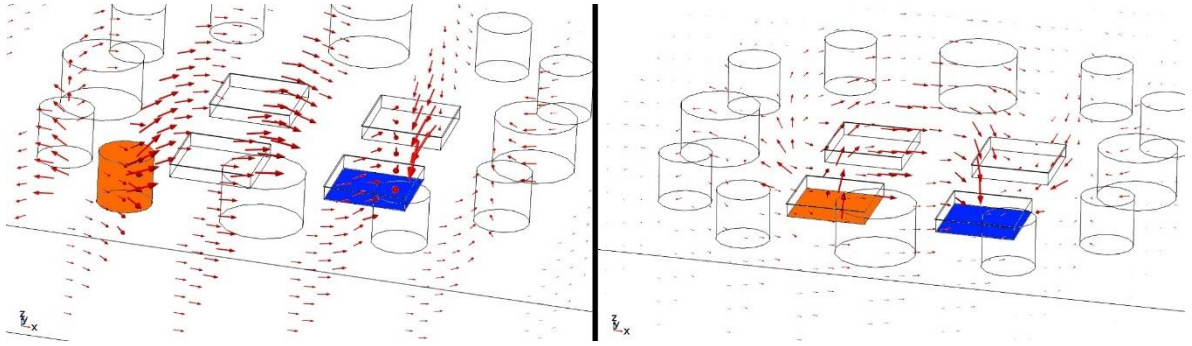


Fig. 15: Electric field generated by a combination of a 3D and a 2D electrodes (left), and two 2D electrodes (right). Red vector sizes are proportional to the electric field strength.

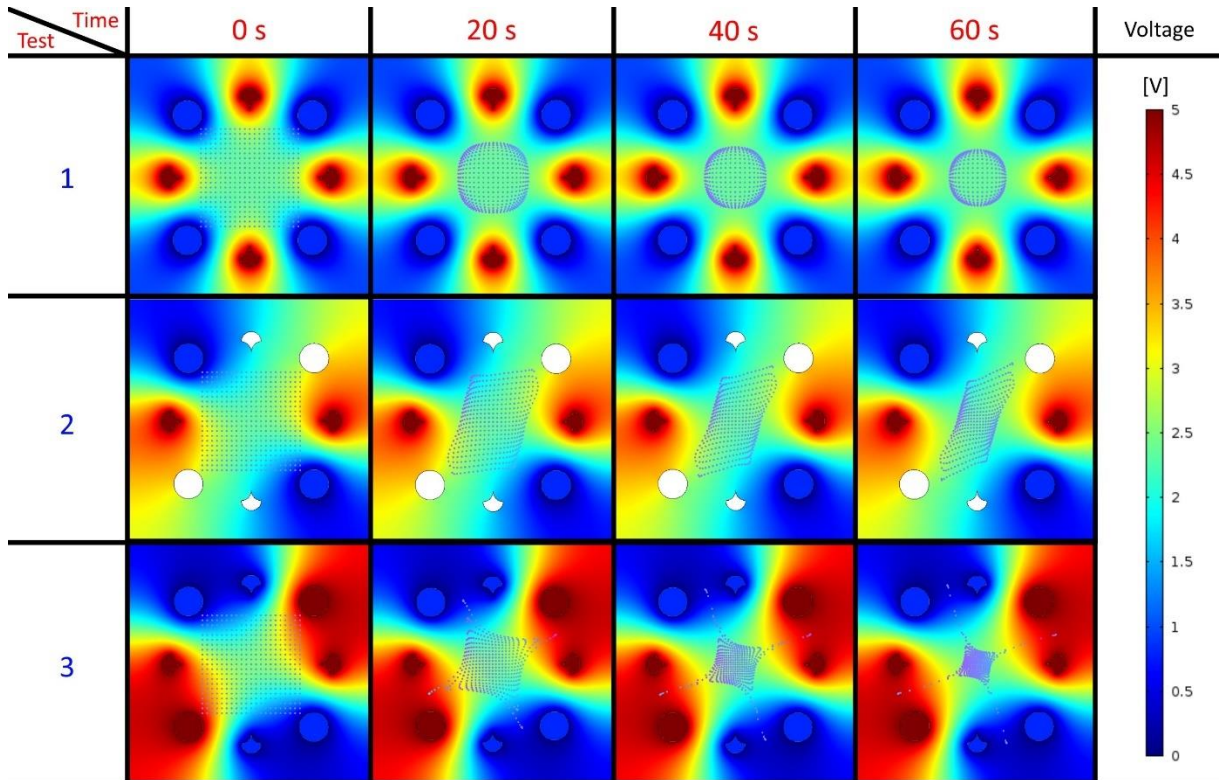


Fig. 16: Snapshots of a 60 second simulation of particle movement along the substrate plane for three configurations of selected 3D microelectrodes. Particle sizes were scaled to 1/10 their size for clarity. No particle-particle interaction was simulated.

Fig. 17 shows the gradient of the squared electric field generated by a two-electrode experiment. Note that the arrow vectors are indicative of the vector of movement of microparticles actuated by this electric field. It should be noted that these vectors remain mainly parallel to the xy-plane, only having a significant z-axis component if the vector is above a microelectrode. Finally, it was confirmed that the squared intensity of the electric field inside this microvolume fits the approximation value obtained in the design goals ($|\nabla E^2| \sim 10^{12} \frac{V^2}{m^3}$).

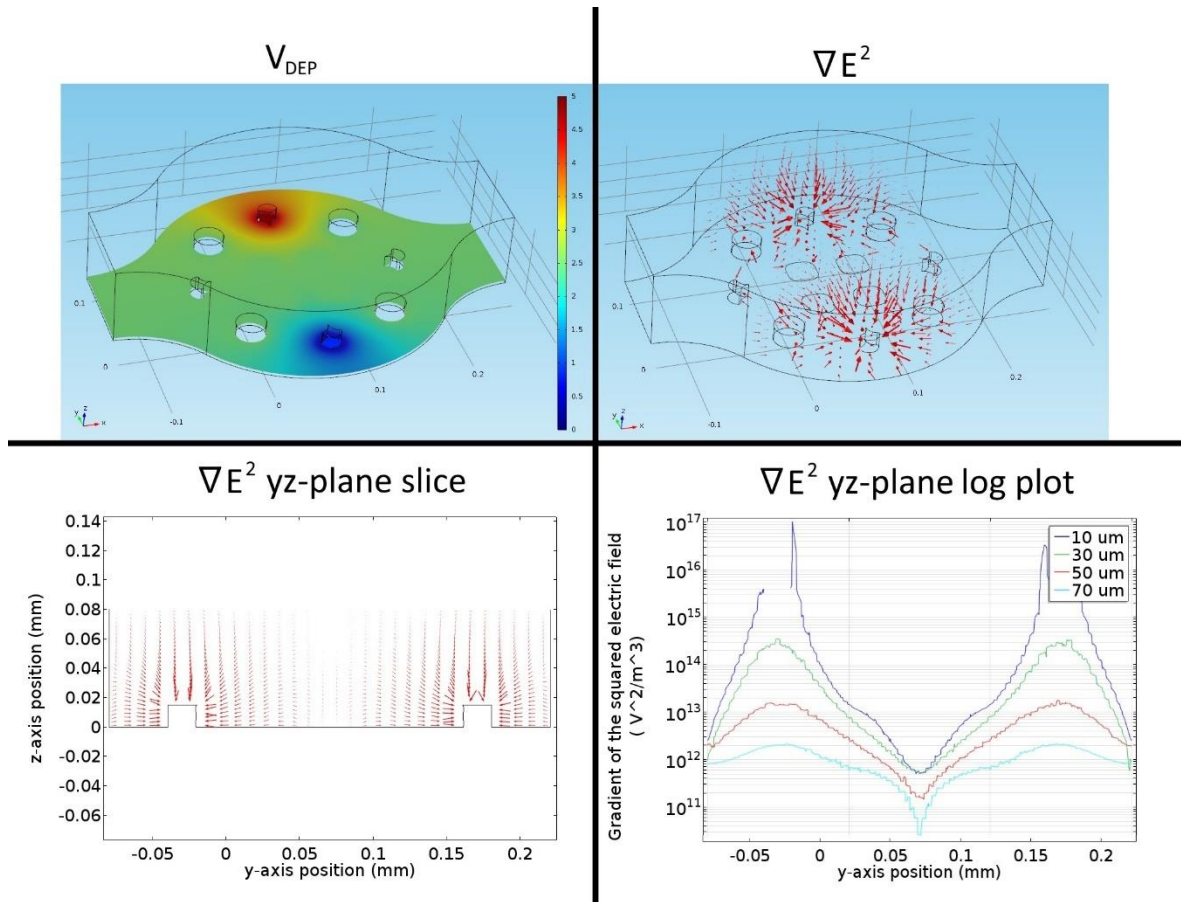


Fig. 17: Simulated electric field strength using a two-electrode configuration. (Top left) Electric potential applied. Resulting gradient of the squared electric field in the volume (top right) and in the yz-plane (bottom left) represented by red vectors. Vector size is proportional to field intensity. (bottom right) Numerical values for the yz-plane electric field at four different distances above the microelectrode array base.

From these simulations it was concluded that the designed microelectrode array would perform the manipulation of bioparticles in the intended fashion.

3.2.2 Microfluidics

The microfluidics module purpose is to house the counter electrode that actuates the particles in the direction perpendicular to the substrate and to contain the particles and medium in a microchannel. An interest was found in developing a microfluidic chip that could be interfaced to the microelectrode array temporally, allowing the use of specific microfluidic designs tailored by application without the need to fabricate an array of microelectrodes for each one application. The conceptual idea is shown in Fig. 18.

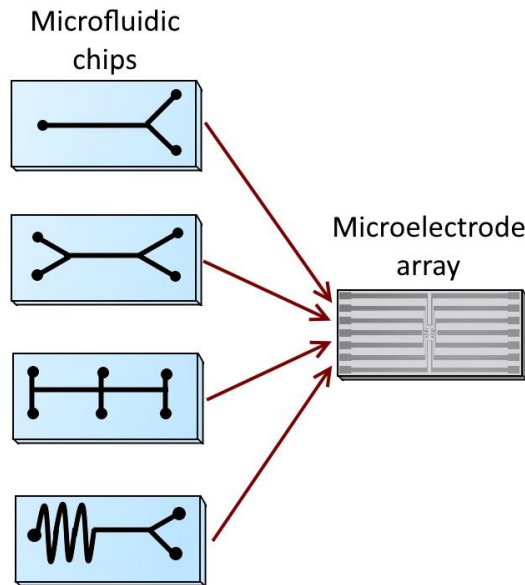


Fig. 18: Conceptual use of multiple microfluidic chip designs with a single microelectrode array chip. For this to be possible, a temporal interface strategy had to be developed.

To enable the temporal use of a microfluidic chip, a combination of the natural adhesion of the polymeric material used to fabricate the chip and mechanical pressure was explored.

The microfluidic chip needed to meet three criteria to be useful:

- Allow fluid flow of the suspension containing the target microparticles.
- Prevent the formation of leaks caused by the temporary nature of the bond between this module and the microelectrode array module.
- Embed the counter electrode needed to actuate the microparticles in the z-axis direction.

A minimalistic microfluidic chip fabricated using soft lithography of polydimethylsiloxane (PDMS) in combination with the microchannel (layer 5) built directly in the microelectrode array module can be used to solve these criteria (Fig. 19). It is possible to embed a glass slide coated with a small indium thin oxide (ITO) electrically conducting layer, which would act as a counter electrode for the 2D microelectrodes enabling z-axis micromanipulation while maintaining optical transparency for observation of the microelectrode zone.

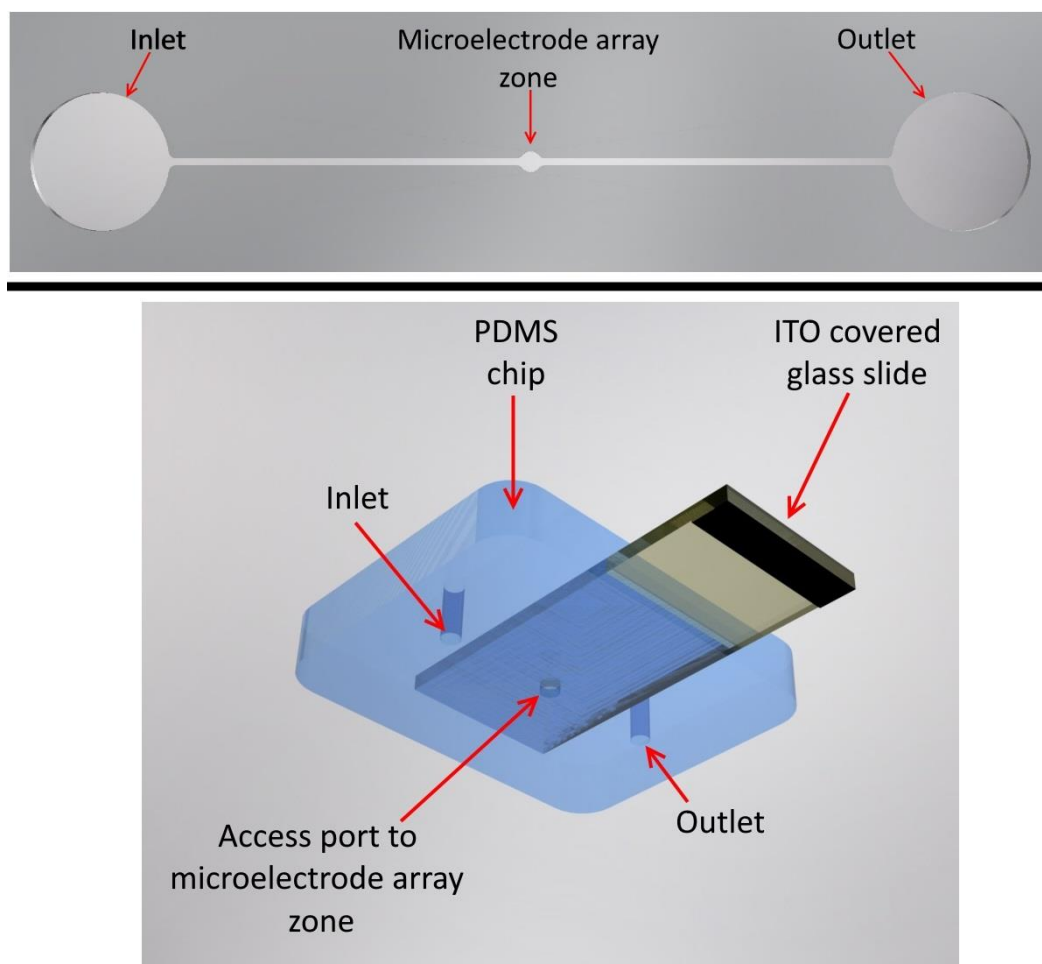


Fig. 19: (Top) Microchannel layer built in the microelectrode array module, and (bottom) PDMS chip that adds the counter electrode (ITO covered slide) for micromanipulation in the z-axis and seals the microchannel.

Finally, a support structure was designed to exert a mechanical force to the microfluidic chip, pushing it against the microelectrode array generating a hermetic seal (Fig. 20). Designs and fabrication protocols of this chip can be found in Appendix D: Microfluidic module designs and fabrication protocols.

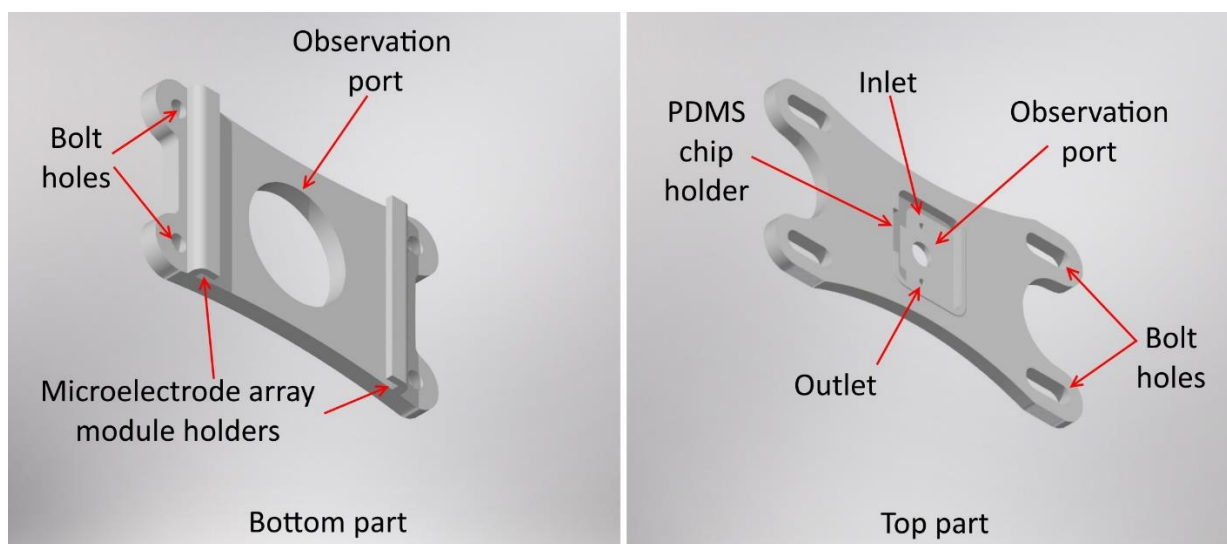


Fig. 20: Microfluidic module support structure. Bottom part slides in the microelectrode array interface board and functions as an anchor support for the top part. The top part holds the PDMS chip and is mechanically secured to the bottom part using four bolts.

3.2.3 Control electronics

The control electronics module function is to allow selective control of the potential applied to individual electrodes. Three main voltage states for the actuation of the electrodes were required: DEP signal, reference potential and high impedance (High-Z, electrically disconnected). To achieve this degree of control an analog switch array operated by a microcontroller was employed. The microcontroller was operated remotely by a graphic user interface (GUI) deployed on a PC. A block diagram describing this module is presented in Fig. 21.

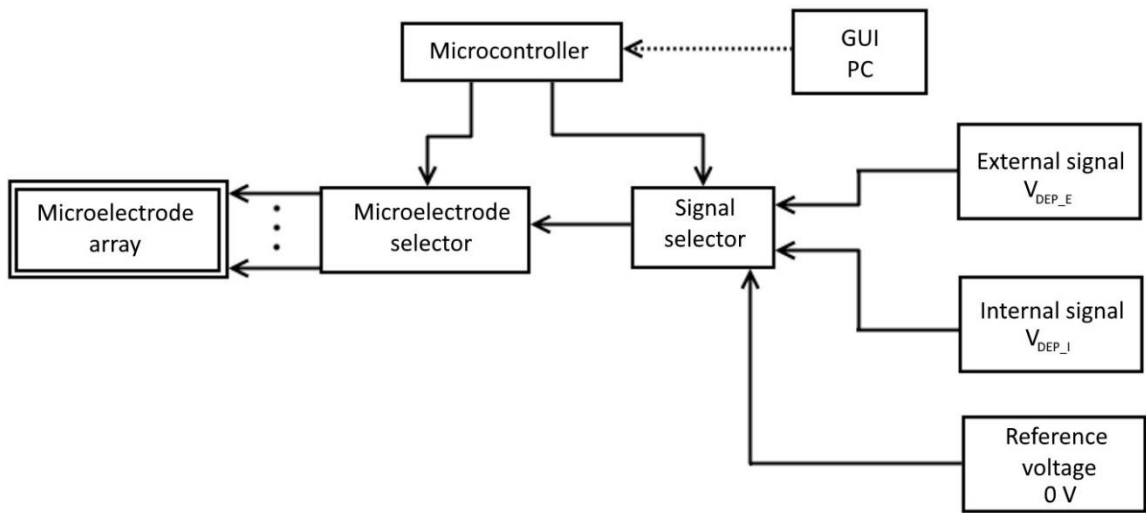


Fig. 21: Block diagram of the electronic submodules and electric signals used in the control electronics module.

A Raspberry Pi (RasPI) module was selected for the microcontroller due to its easy implementation for remote control using MATLAB software, which was used to develop the GUI used to control each microelectrode (Fig. 22). A HV2801 32-channel high voltage analog switch was used for the microelectrode selector and signal selector blocks. Additionally, a $\pm 22\text{ V}$ oscillator at 250 kHz, a BNC input connector and a stable ground (GND) rail were designed as internal, external and reference voltage source signals for V_{DEP} .

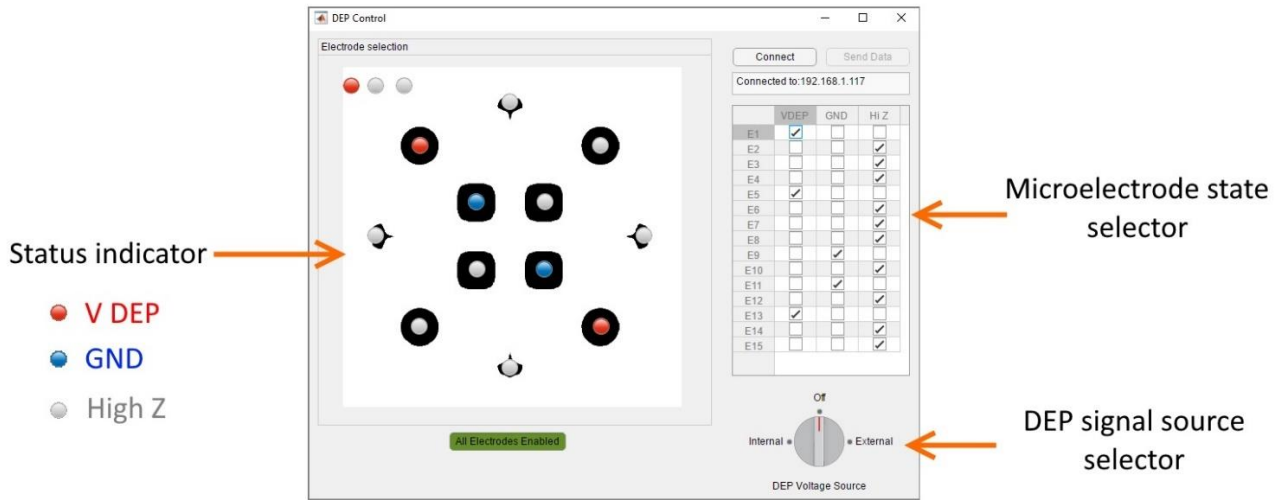


Fig. 22: Graphic user interface (GUI) that controls the electrical state of each microelectrode.

First, the user must use the “Connect” button to attempt a connection with the control electronics module. If the connection results successful, the “Send Data” button becomes enabled.

Afterwards, the user should select in the GUI the voltage source for the DEP signal (external, internal or off), and the electrical state applied to each electrode (V_{DEP} , GND or High-Z) guided by the designator shown in Fig. 23. The corresponding status indicators light up with the appropriate color code for a quick and easy way to confirm the microelectrode configuration. At this point the user can push the “Send Data” button to configure the actual microelectrodes.

After pressing “Send Data”, the GUI sends the appropriate configuration strings to the RasPI module through a wireless network connection. After receiving the string, the RasPI module relays the information via SPI protocol to the analog switch array, configuring each switch state for each microelectrode (Fig. 24). The control electronics module physically connects to the microelectrode module using a custom twisted-pair cable.

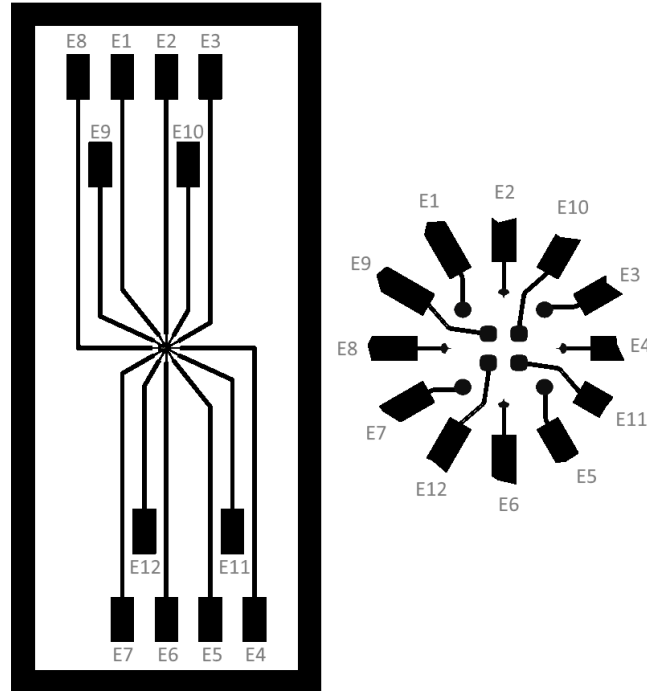


Fig. 23: Pinout and designator names for each microelectrode.

Standard GST40A 40W 48V and SPN5993A 15W 5V modules were used as power supplies for the main electronics board and RasPI respectively. Detailed electrical schematics and PCB designs of each electronics submodule, software code for the GUI and RasPI firmware, and design schematics of the module support structure are supplied in Appendix E: Control electronics module designs and software. The final control electronics module is shown in Fig. 25.

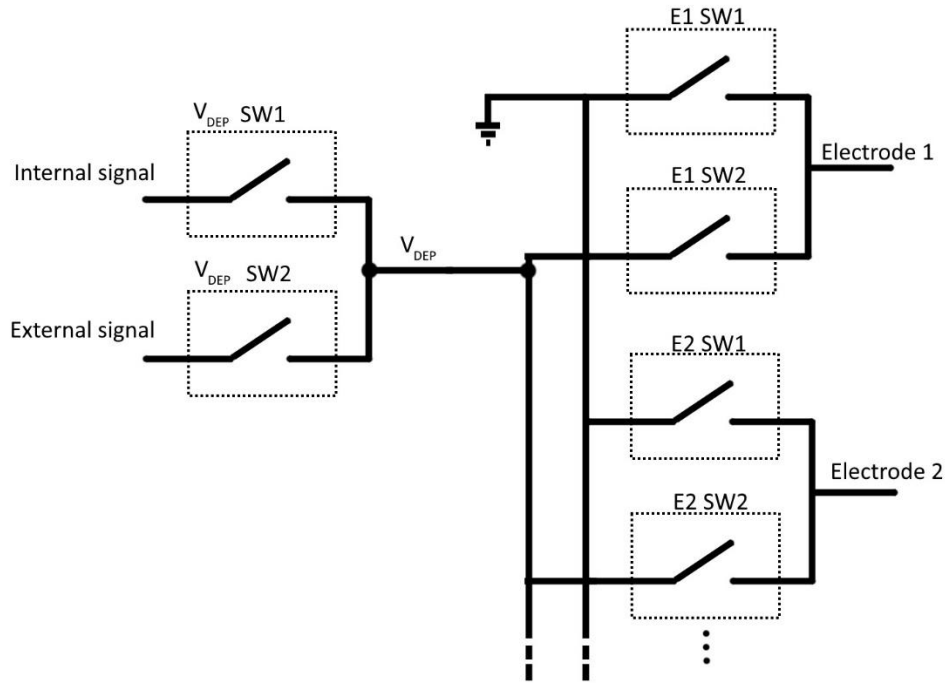


Fig. 24: Electrical connections for the signal rails interfacing with each microelectrode. Switches on the left side select the DEP voltage source while switches in the right side select the electrode state (VDEP, GND or High-z).

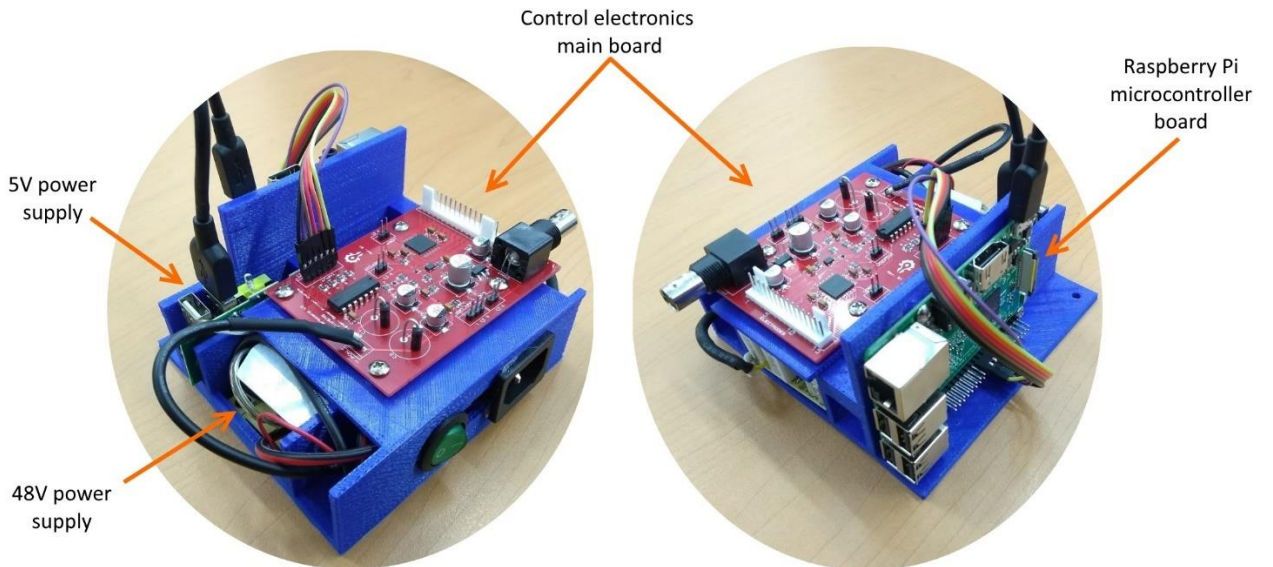


Fig. 25: Control electronics module mounted in a minimalistic custom support.

4 MICRO PLATFORM TESTS AND RESULTS

The produced micro platform and its components were thoroughly tested. First, the carbon microelectrodes produced by C-MEMS technology were fully characterized by optical and scanning electron microscopy, optical profilometry and Raman microscopy. Afterwards, electrical resistivity and adhesion to substrate were measured. Then, the intended experimental array for bioparticle micromanipulation was assembled. At this point the microfluidic chip was tested for leaks and the control electronics were tested for selective electric potential application. Finally, particle image velocimetry and optical microscopy were used to characterize actuated particle movement inside the microvolume

4.1 MICROELECTRODE ARRAY METROLOGY

4.1.1 Optical microscopy

Optical photographs were taken of the microelectrode array during each step of its fabrication. This process is shown in Fig. 26. Fig. 27 shows the full transducer after pyrolysis.

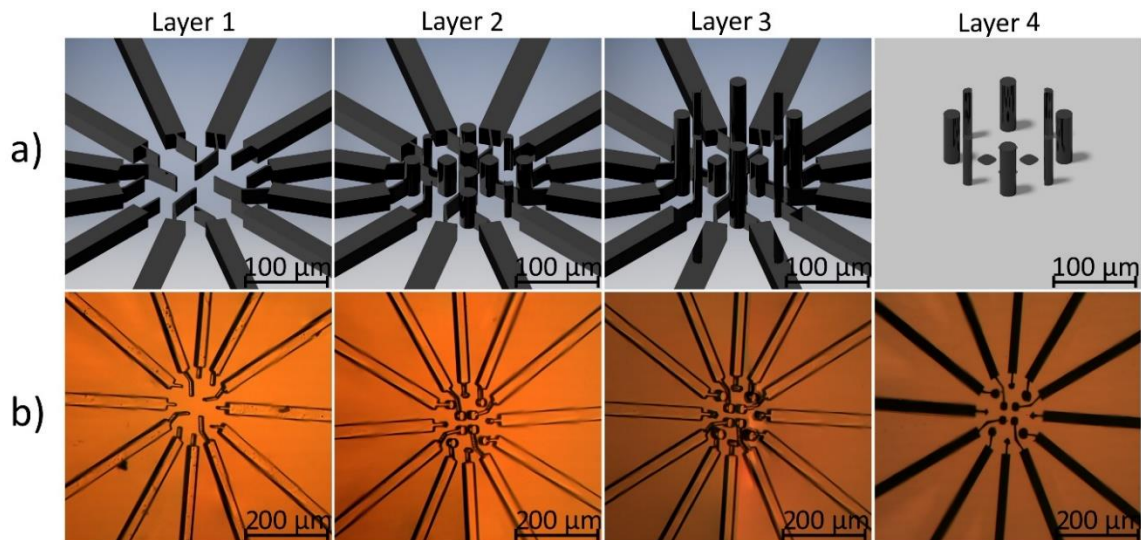


Fig. 26: Step by step graphical renders (a) and photographs (b) of the microelectrode array fabrication process. Layers 1 through 3 were patterned before pyrolysis and layer 4 after pyrolysis.

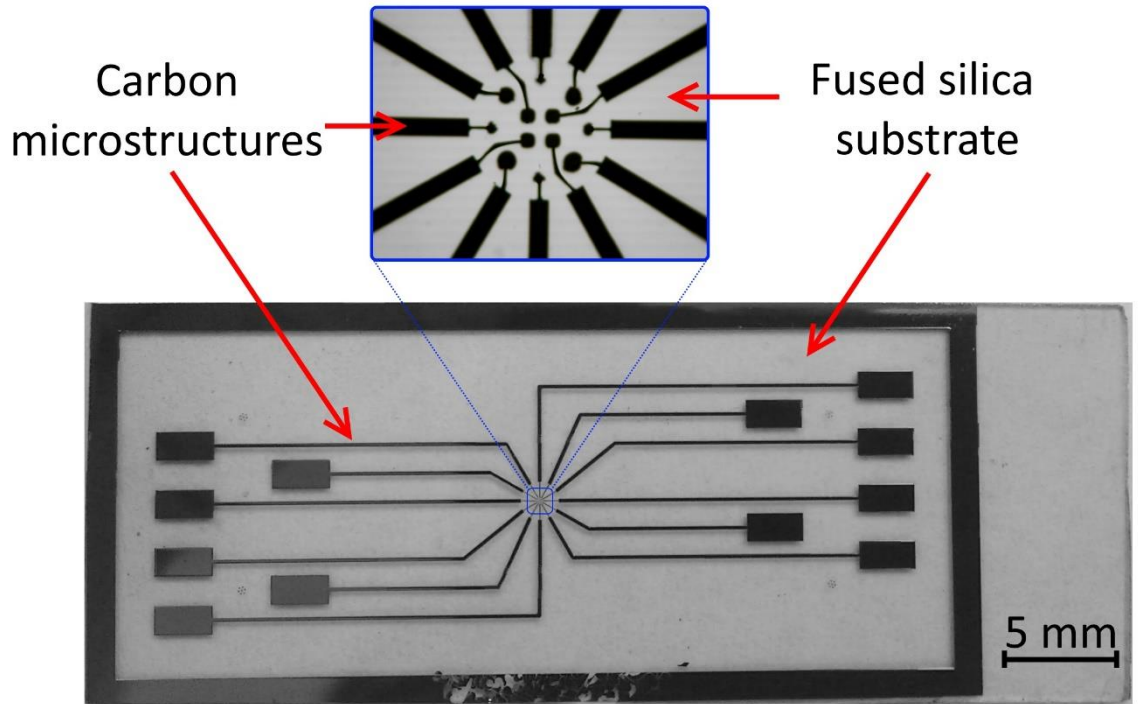


Fig. 27: Photograph of the full microelectrode C-MEMS chip after pyrolysis.



Fig. 28: Photograph of the complete electronics interface board with C-MEMS microelectrodes connected to the PCB.

4.1.2 Scanning electron microscopy (SEM)

SEM images were acquired to inspect the produced carbon porosity and microstructure shapes after pyrolysis. Images were acquired with a JSM-7800F Schottky Field Emission Scanning Electron Microscope. Some distortion at the interface between layer 2 and 3 was observed through a mismatch between the circular microelectrode diameters, and defects in the smallest diameter microelectrodes. Finally, no porosity was observed in images taken up to a 4000x magnification.

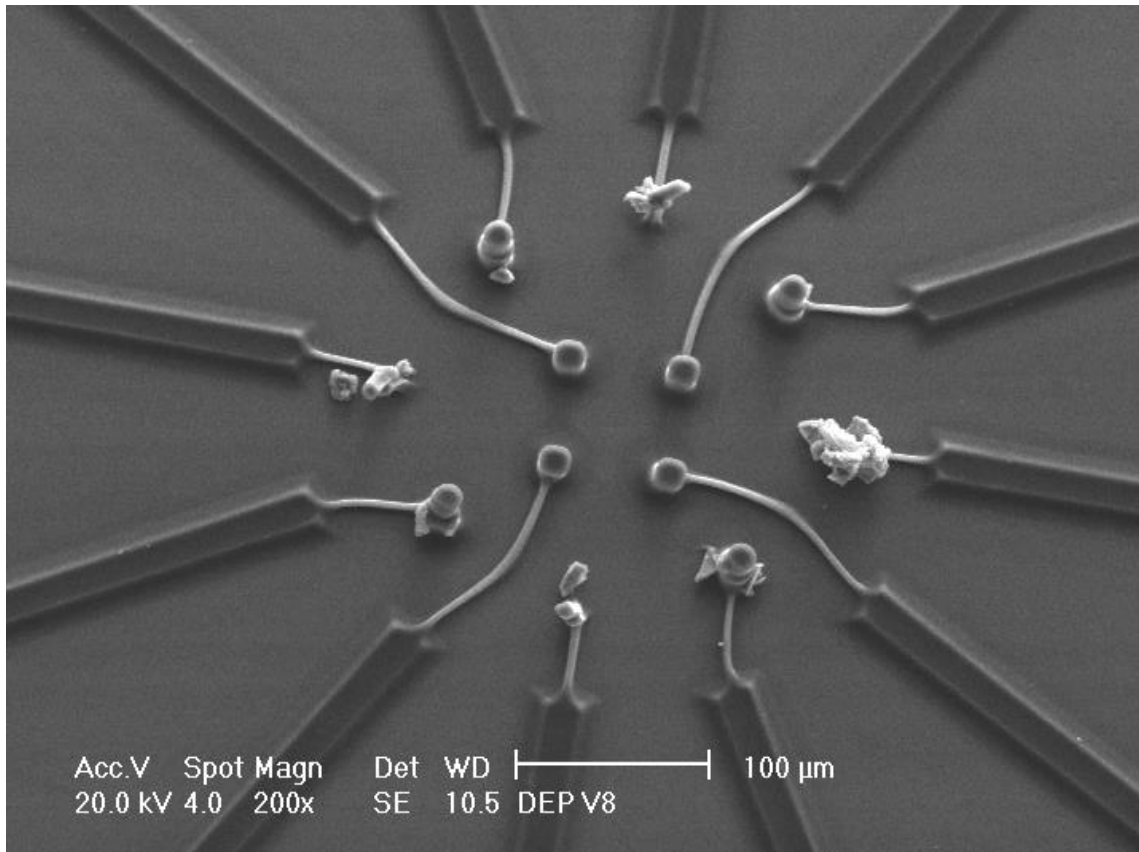


Fig. 29: 200x SEM image of the carbon microelectrode array after pyrolysis.

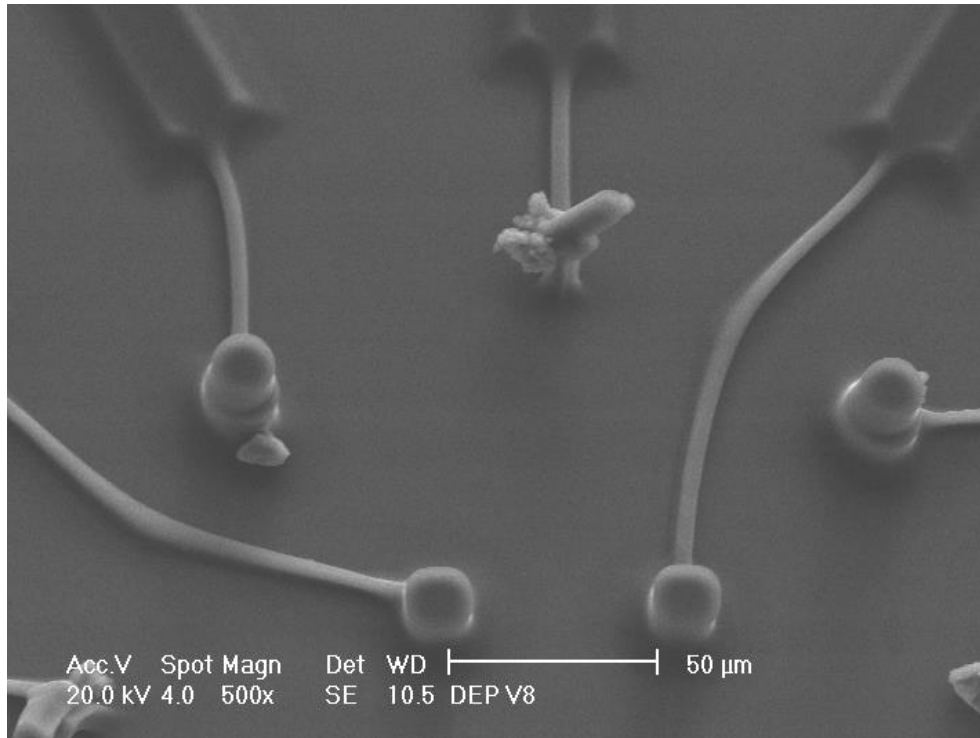


Fig. 30: 500x SEM image of the 2D and 3D microelectrodes. Some distortion at the interface between layer 2 and 3 is observed. Also, there is a deformation on the smallest diameter microelectrode structures.

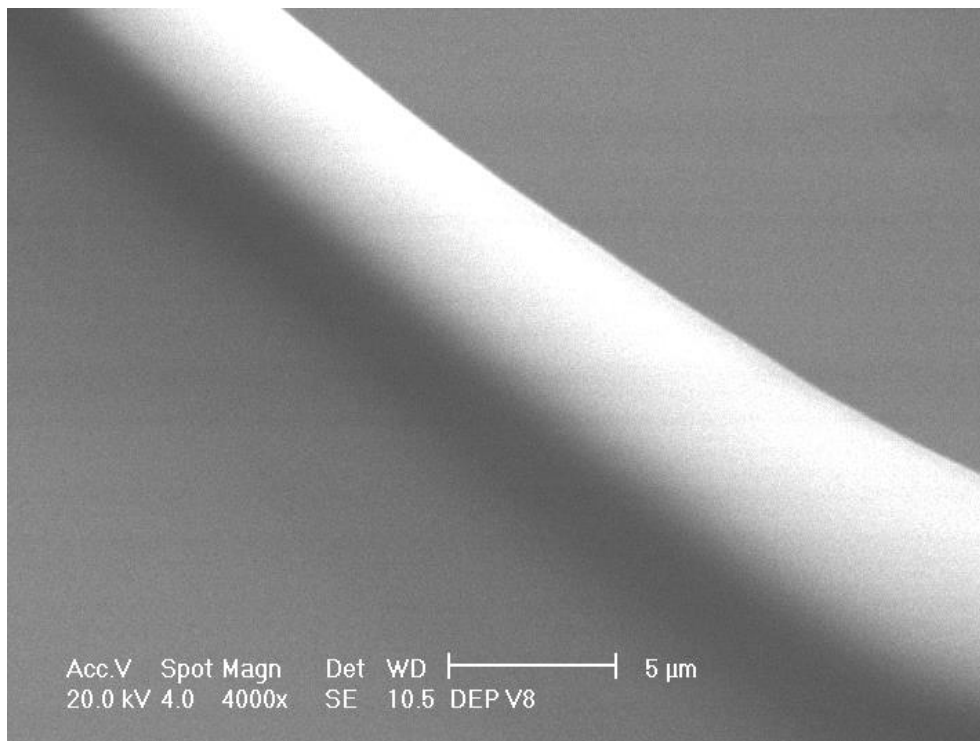


Fig. 31: 4000x SEM image of the carbon microstructures. Top right corner is substrate while bottom left is a carbon microstructure. No appreciable pores were found at this scale.

4.1.3 Optical profilometry

A Zygo Nexview optical profilometer was employed to characterize the height of the carbon microelectrodes. Mean structure heights measured from the substrate were:

- Electrical traces: $10.3 \pm 0.18 \mu\text{m}$
- 2D microelectrodes: $15.3 \pm 0.32 \mu\text{m}$
- 3D microelectrodes: $33.5 \pm 0.54 \mu\text{m}$

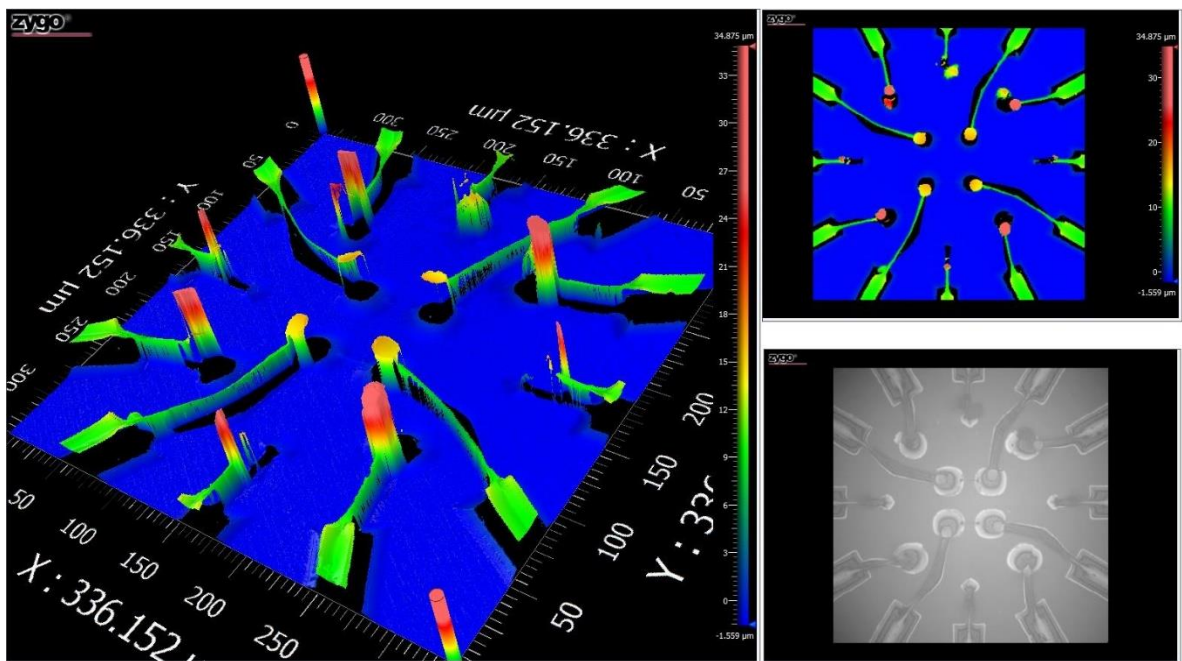


Fig. 32: Optical profilometry of the microelectrode array. (Left) 3D perspective, (top right) top perspective and (bottom right) photograph of the measured zone.

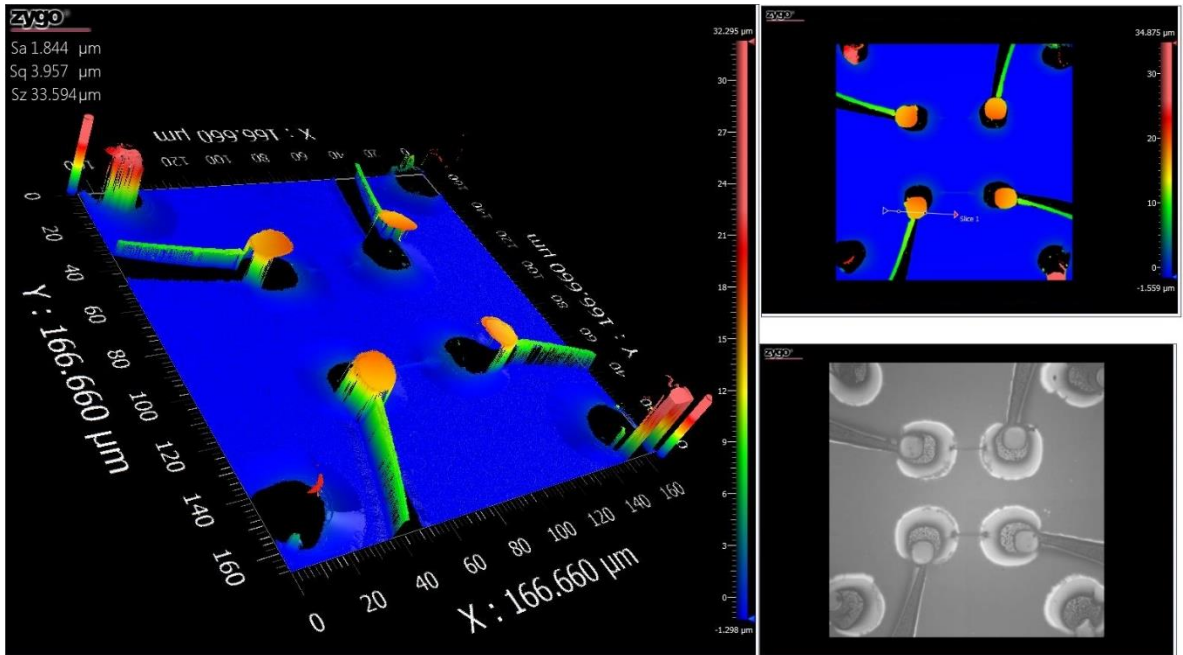


Fig. 33: Optical profilometry of the 2D microelectrodes. (Left) 3D perspective, (top right) top perspective and (bottom right) photograph of the measured zone.

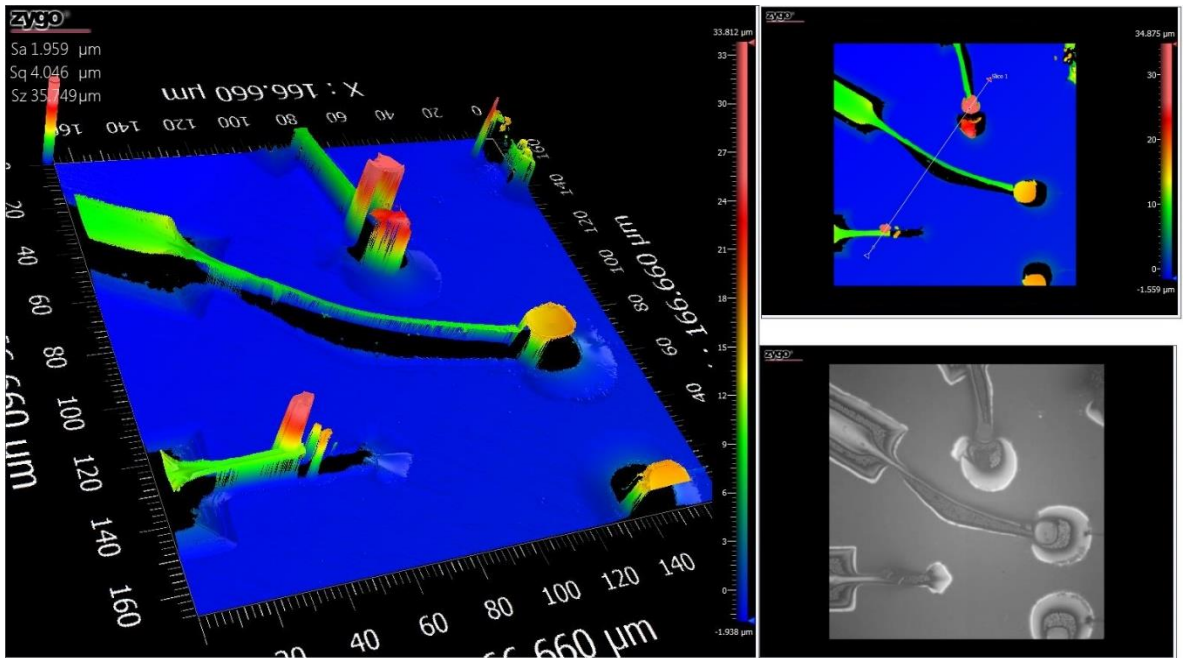


Fig. 34: Optical profilometry of the 3D microelectrodes. Note the aberration due to a diameter mismatch between layers 2 and 3. (Left) 3D perspective, (top right) top perspective and (bottom right) photograph of the measured zone.

4.1.4 Raman spectra

Raman spectra of the carbon produced by both pyrolysis process (95% N / 5% H forming gas, and vacuum) was measured by Raman spectroscopy (DXR, Thermo Scientific). Spectra are shown in Fig. 35.

Both spectra show the characteristic peaks exhibited by pyrolytic carbon. The peaks of gas treated samples were found at $1333.5 \pm 2.25 \text{ cm}^{-1}$ and $1591.7 \pm 2.55 \text{ cm}^{-1}$. Peaks of vacuum treated samples were found at $1350 \pm 1.4 \text{ cm}^{-1}$ and $1585 \pm 0.4 \text{ cm}^{-1}$.

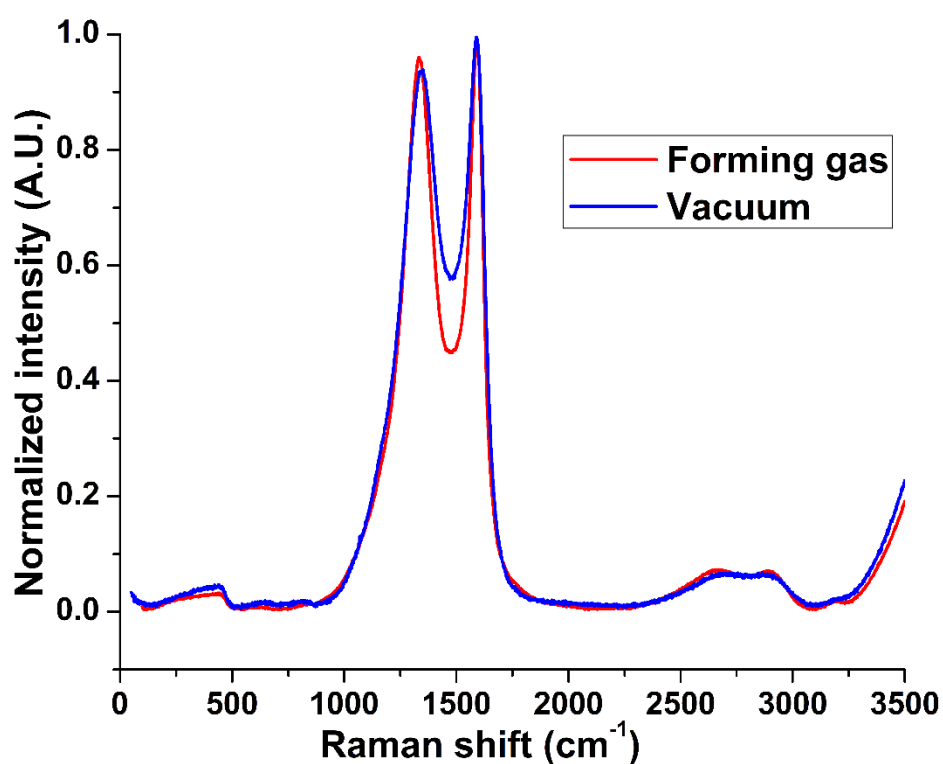


Fig. 35: Raman spectra of the produced carbon microstructures. Both spectra show the characteristic peaks of pyrolytic carbon close to the 1350 cm^{-1} and 1580 cm^{-1} bands.

4.1.5 Electrical resistivity

Van der Pauw's method was employed to characterize the electrical resistivity (ρ). Using equation (38) it is possible to obtain the electrical resistivity of the material from the thickness of the carbon layer (t) and the trans-resistances (R_{ABCD} and R_{BCDA}) formed between the four electrical probes (A, B, C and D) placed along the surface of the material.

$$e^{-\pi t \frac{R_{ABCD}}{\rho}} = 1 - e^{-\pi t \frac{R_{BCDA}}{\rho}} \quad (38)$$

Cloverleaf-shaped carbon samples were fabricated using the photolithography and pyrolysis processes described previously (same design used in Appendix I). Four wire contacts were attached in each corner of the sample using a conductive carbon cement (Leit-C, SPI-CHEM). Measurements were carried out using a SMU (Keithley 2450) in air at ambient pressure.

A known electrical current was applied to two of the wire contacts while the resulting electrical potential generated in the other two contacts was measured. Two sets of measurements were performed using these parameters: one for the voltage between points A and B (V_{AB}) induced by a current flowing from point C to D (I_{CD}), and another for the voltage between points B and C (V_{BC}) induced by a current flowing from point D to A (I_{DA}). Linear regressions of the resulting curves were calculated to obtain their slopes which represent the transresistances R_{ABCD} ($4.962 \pm 0.003 \Omega$) and R_{BCDA} ($4.961 \pm 0.004 \Omega$). Eq. (38) was numerically solved using a computer program (Appendix G: MATLAB programs) for ρ using an average measured thickness of $17 \mu m$, giving an electrical resistivity of $0.382 \pm 0.003 m\Omega m$.

4.1.6 Adhesion to substrate

The adhesion force to the substrate was measured using a micro-scratch tribometer (Nanovea, PB1000) with a steel ball as the counter body (1.58 mm diameter), and a variable-load scratch tests performed for each sample, with a 7.5 N loading rate and a 0.2 N - 15 N range.

It was found that spallation happened on the forming gas treated carbon at an applied force of 1.661 ± 0.102 N whilst the carbon formed on a vacuum showed this failure with an applied force of 3.212 ± 0.322 N.

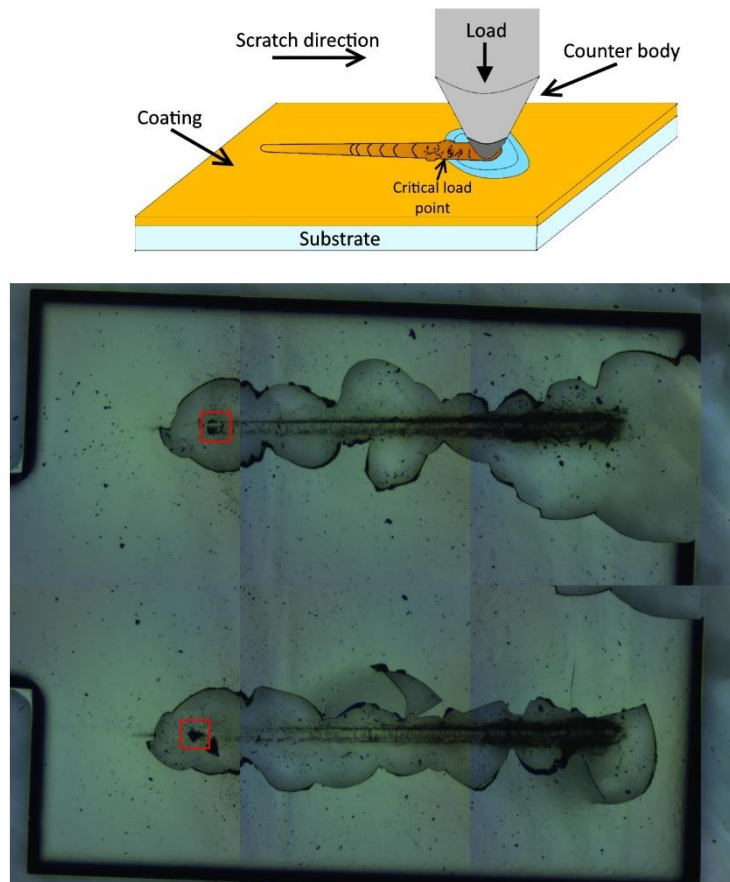


Fig. 36: (Top) Scratch test representative schematic and (Bottom) a pair of scratch test measurements. Loading tip traveled from left to right. Spallation force was reached at the marked spots.

4.2 EXPERIMENTAL ARRAY

4.2.1 Complete micro-platform

The micro platform was assembled as shown in Fig. 37. The ITO counter electrode was electrically connected to the microelectrode array module through a toothless alligator clip.

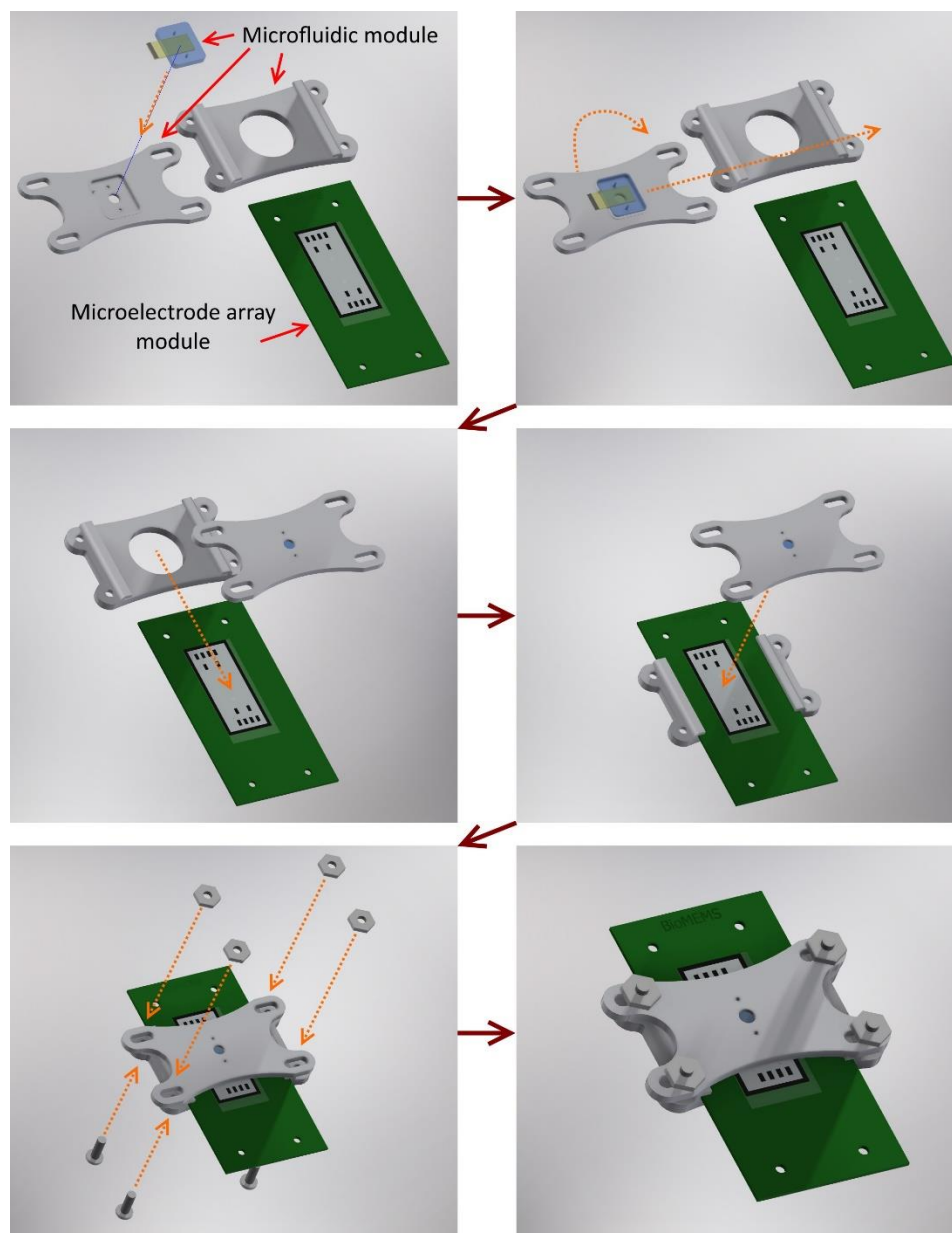


Fig. 37: Assembly of the micro platform.

Two suspensions with fluorescent microparticles were prepared for experimentation:

- 1 μm particle suspension
 - Polystyrene microparticles (Fluospheres F13080)
 - Density $\rho = 1040 \frac{\text{kg}}{\text{m}^3}$
 - Diameter $\phi = 1 \mu\text{m}$
 - Electrical conductivity $\sigma_p = 6.7 \times 10^{-14} \frac{\text{S}}{\text{m}}$
 - Electrical permittivity $\epsilon_p = 2.6$
 - Concentration $C_0 = 2 \times 10^8 \frac{\text{particles}}{\text{ml}}$
 - Medium (1.6 M NaCl solution)
 - Electrical conductivity $\sigma_m = 12.6 \frac{\text{S}}{\text{m}}$
 - Electrical permittivity $\epsilon_m = 60$
 - Dynamic viscosity $\mu = 9 \times 10^{-4} \text{ Pa s}$
- 10 μm particle suspension
 - Polyamide 12 with rhodamine B microparticles
 - Density $\rho = 1010 \frac{\text{kg}}{\text{m}^3}$
 - Diameter $\phi = 10 \mu\text{m}$
 - Electrical conductivity $\sigma_p = 1 \times 10^{-10} \frac{\text{S}}{\text{m}}$
 - Electrical permittivity $\epsilon_p = 3.5$
 - Concentration $C_0 = 1 \times 10^6 \frac{\text{particles}}{\text{ml}}$
 - Medium (Deionized water + 2% NaCl + 2% Tween 20)
 - Electrical conductivity $\sigma_m = 5 \times 10^{-6} \frac{\text{S}}{\text{m}}$
 - Electrical permittivity $\epsilon_m = 80$

4.2.2 Proof of concept experiment

The 1 μm particle suspension was employed in a preliminary set of experiments with simple microelectrode configurations to confirm the expected motion of the particles inside the control volume. For this experiment, the micro platform was mounted in an inverted fluorescence microscope and a high-speed camera (Phantom MIRO 310) was used to record the movement of particles.

- Electric signal applied
 - Electric potential $V_{DEP} = 60\text{ V}$
 - Signal source = external
 - Signal type = sine
 - Signal frequency $f = 100\text{ kHz}$

Due to the electrical properties of the particles and medium, nDEP was expected, that is, particles closer to the electrodes should move away from them. This was confirmed as shown in Fig. 38.

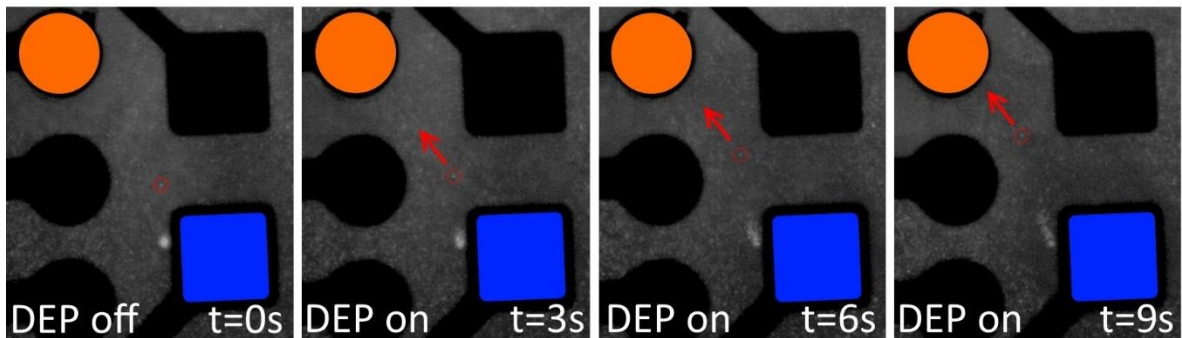


Fig. 38: Snapshots of a 9 second 1 μm particle suspension experiment. Orange electrode is connected to V_{DEP} while blue electrode is connected to ground. A particle and its motion are highlighted in red. Note its movement in a vector colinear to the applied electric field, and away of the closest electrically active microelectrode indicating nDEP.

Particle image velocimetry (PIV) was used to investigate the vectors of movement of the actuated particles. It was found that the vectors converge to a line located in between of the actuating electrodes (Fig. 39). Upon reaching this point, the microparticles moved away from the focal point of the microscope, indicating a change in their z-axis position. These results were published in ECS transactions [108] with the manuscript presented in Appendix H: Article “Micro Device for Bioparticle Positioning in a 3D Space Based on Carbon MEMS and Dielectrophoretic Forces”.

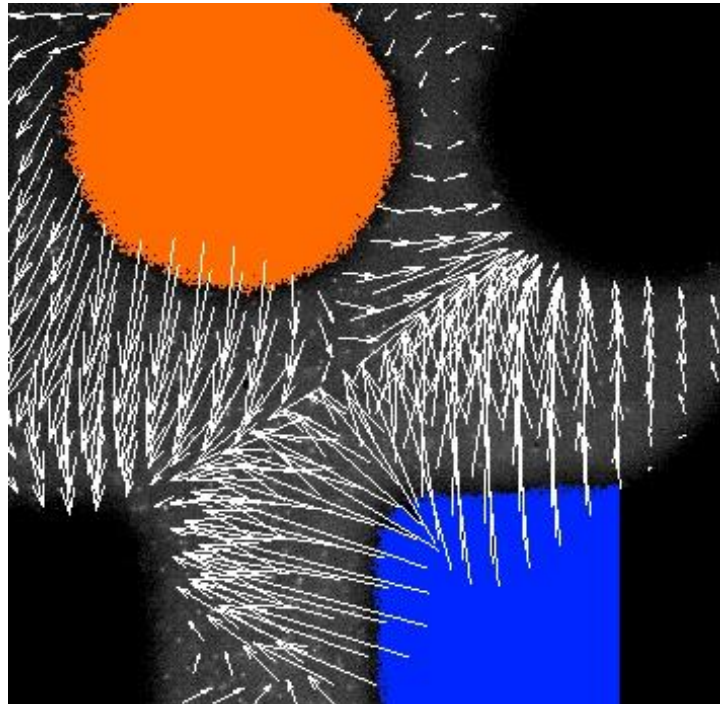


Fig. 39: Particle image velocimetry of the experiment described in Fig. 38. The white arrows represent the velocity vectors of the microparticles and are indicative of microparticle movement.

4.2.3 Micromanipulation experiment

The micro platform was mounted in a TCM 400 fluorescence inverted microscope for observation and then connected to the control electronics module. A M2 camera (Pixelink) was used to record the experiment (Fig. 40). Several microelectrode configurations were used to test the micromanipulation capabilities of the micro platform. The 10 μm particle suspension and the following electrical signal characteristics were used for this experiment.

- Electric signal applied
 - Electric potential $V_{DEP} = 15\text{ V}$
 - Signal source = external
 - Signal type = sine
 - Signal frequency $f = 1\text{ MHz}$

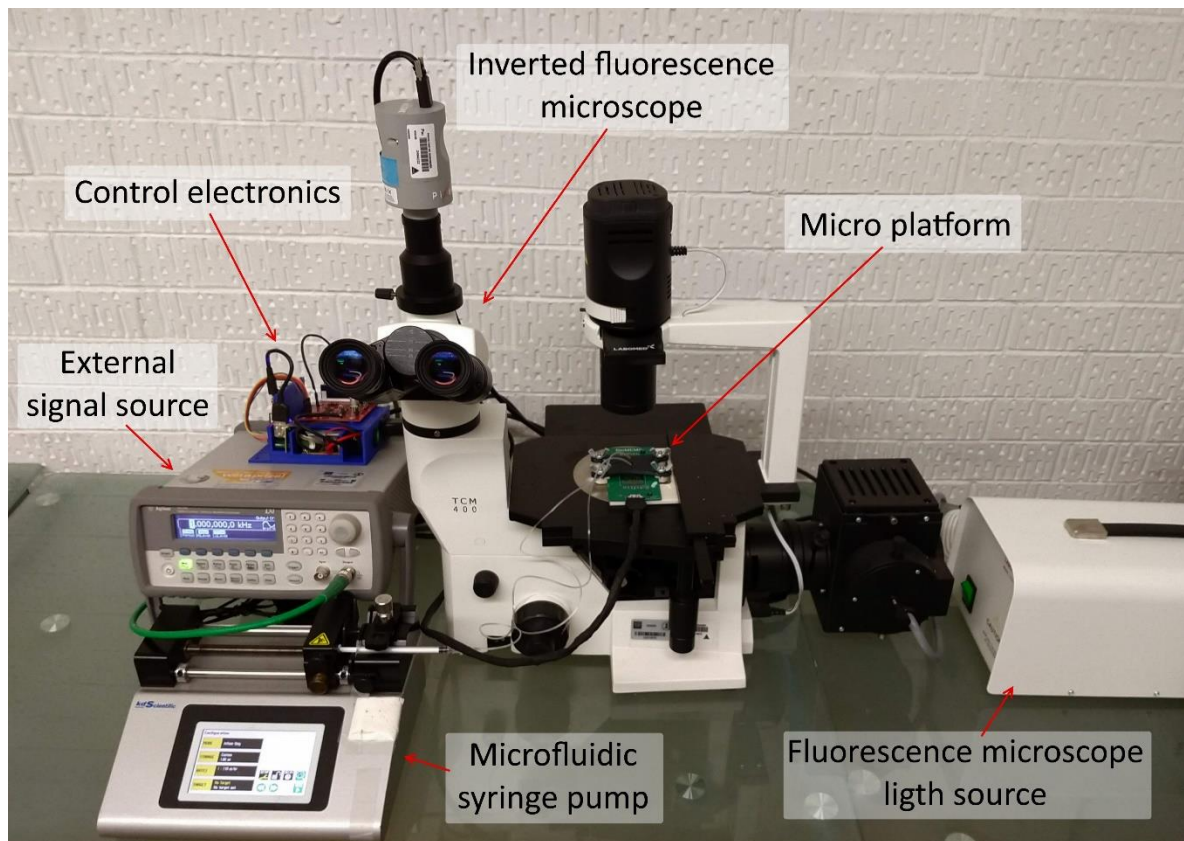


Fig. 40: Experimental setup for the micromanipulation experiment with the micro platform.

It was observed that tridimensional micromanipulation was achievable with the micro platform (Fig. 41 and Fig. 42). By selecting specific microelectrode electrical configurations, it was possible to predict and direct microparticle movement inside the control volume to a desired destination.

One limitation found was the available motion directions imposed by which type of DEP force (positive or negative) was exerted in the particle-medium system. In this experiment for example, due to the electrical characteristics of the medium and particle, only nDEP was possible in all frequency ranges, therefore to move the particles in a desired fashion this limitation in motion had to be considered. Another difficulty resulted from the sedimentation of particles. Once a particle touched a surface the force exerted by DEP was insufficient to keep moving it due to the no slip condition.

Above all, these experiments demonstrated the potential for precise micromanipulation of bioparticles inside a control microvolume by the proposed micro platform.

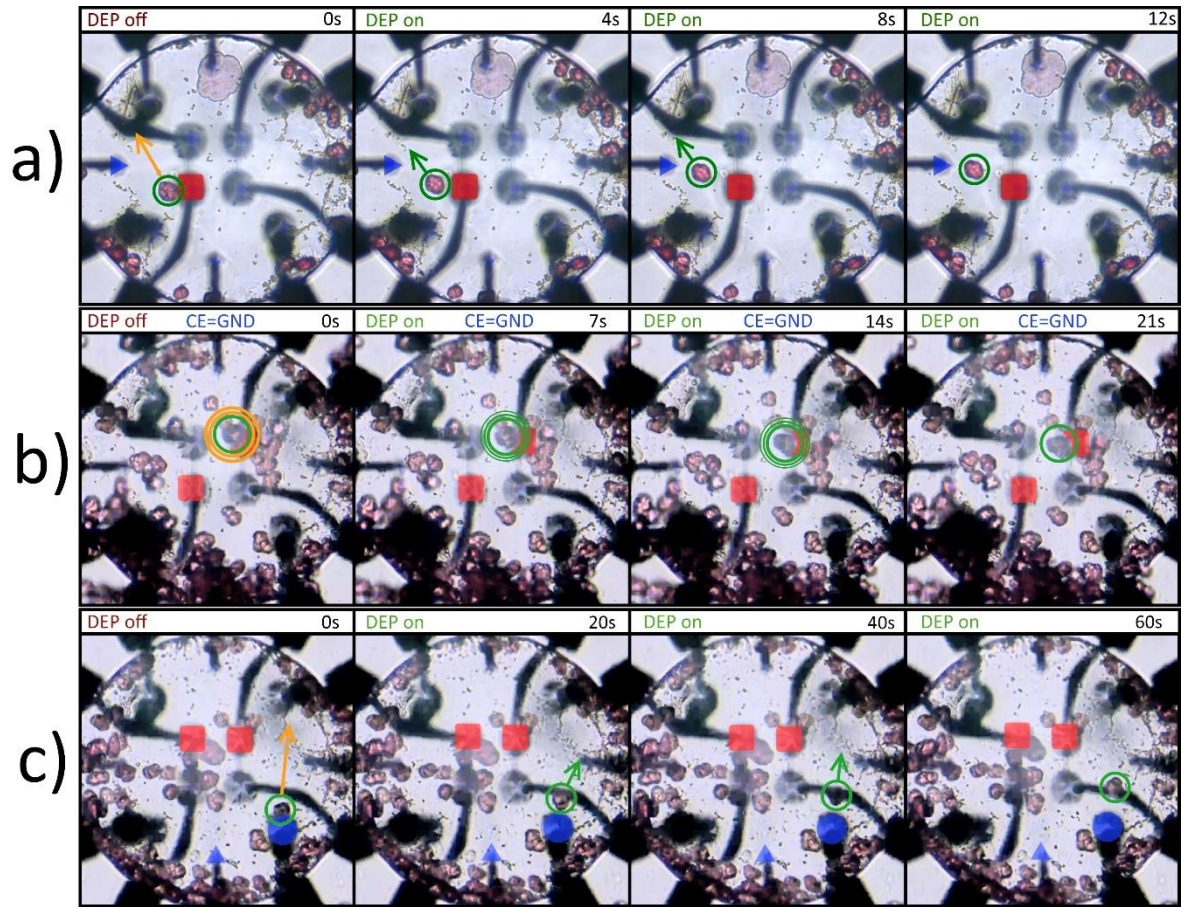


Fig. 41: Snapshots of single particle micromanipulation experiments along the xy-plane (a and c) and in the z-axis directions (b). In sequence b, note how the particle enters and exits the focal plane of the microscope. Orange arrows denote intended particle motion before the experiment. Green arrows denote actual particle movement during the experiment. Concentric circles denote movement perpendicular to the focal plane (z-axis). Working electrodes (red = V_{DEP} and blue = GND) and particle movement (green circle) are highlighted.

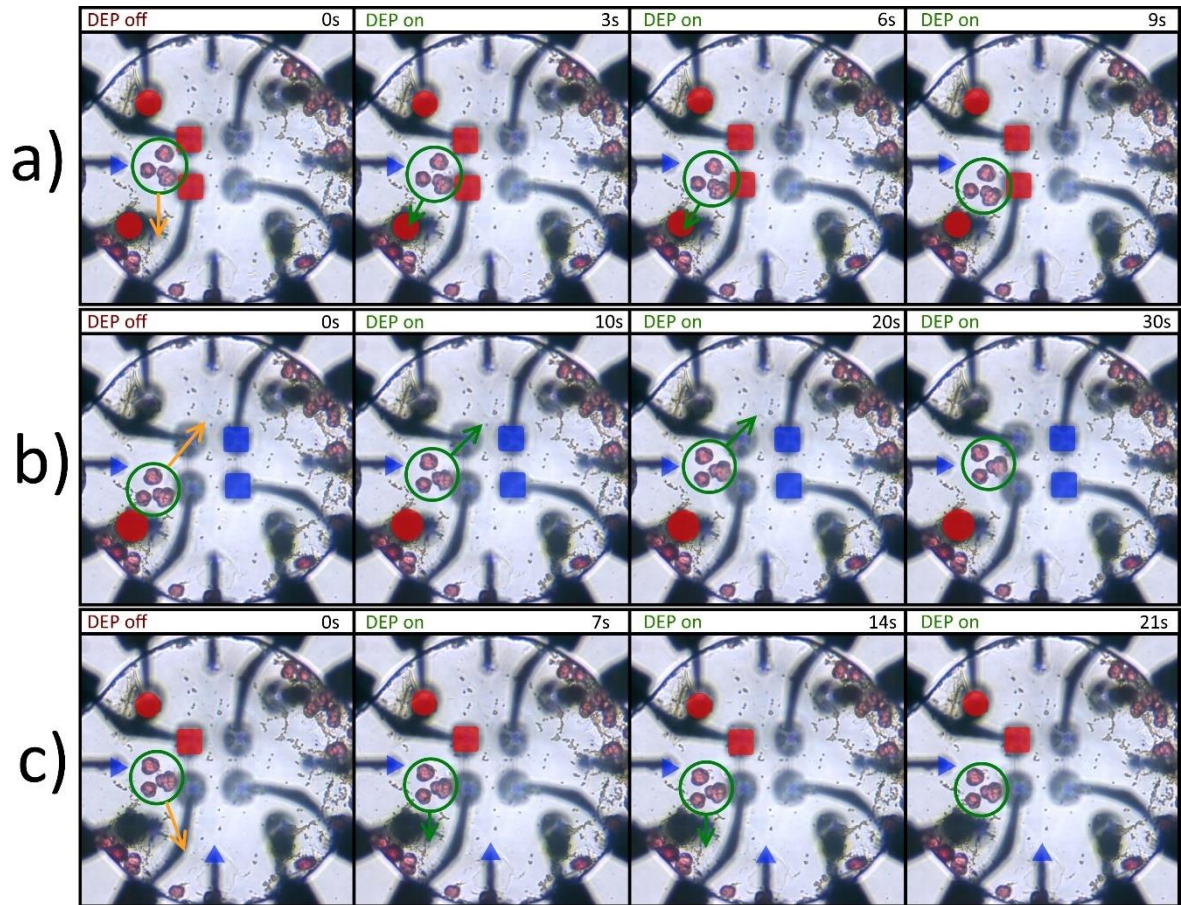


Fig. 42: Snapshots of multiple particle micromanipulation experiments along the xy-plane (a-c). Orange arrows denote intended particle motion before the experiment. Green arrows denote actual particle movement during the experiment. Working electrodes (red = V_{DEP} and blue = GND) and particle movement (green circle) are highlighted.

5 CONCLUSIONS

The design and construction of a micro platform that enables the micromanipulation of bioparticles in a microvolume was explored. Current micromanipulation techniques were reviewed and an electrokinetic approach using the dielectrophoretic effect was selected due to its miniaturization advantages.

DEP force and relevant fluid dynamic forces were mathematically obtained to predict the movement of a dielectric particle suspended in a liquid medium due the application of an electric field.

Microelectrode configurations and operating strategies directed toward DEP micromanipulation were compared and an array combination of 2D and 3D electrodes was deemed optimal to exert movements in microparticles inside an microvolume. This was confirmed by finite element simulations.

The micro platform was divided in three main modules: a microelectrode array, a microfluidic chip and a control electronics module. C-MEMS technology was used for the fabrication of the microelectrode array module because the resulting material (glassy carbon) has clear advantages for biological applications, such as electrochemical stability and biocompatibility. Soft lithography of PDMS was employed to fabricate the microfluidic chip for the same reasons. A control electronics and GUI software were developed to easily allow the user to apply a DEP force in whichever combination of microelectrodes was deemed necessary.

The produced carbon microelectrodes were methodically characterized, finding that the produced material was indeed glassy carbon with Raman spectra peaks found at $1350 \pm 1.4 \text{ cm}^{-1}$ and $1585 \pm 0.4 \text{ cm}^{-1}$, an electrical resistivity of $0.382 \pm 0.003 \text{ m}\Omega \text{ m}$, an adhesion force to the substrate of $3.212 \pm 0.32 \text{ N}$, and average electrical trace heights of $10.3 \pm 0.18 \mu\text{m}$, 2D electrode heights of $15.3 \pm 0.32 \mu\text{m}$ and 3D electrode heights of $33.5 \pm 0.54 \mu\text{m}$.

The complete micro platform was assembled and tested using fluorescent microparticles as comparable substitutes for bioparticles. A negative DEP force was observed for the proposed experiment (Clausius-Mossotti factor ~ -0.5) at relatively low applied voltages ($\sim 15 V$). That is, particles were repelled from regions with high electrical field gradients. Above all, particle micromanipulation in the microvolume was achieved.

Although these experiments showed that the micro platform has potential for the precise micromanipulation of particles throughout the control volume, the observation strategy that was used was insufficient to correctly assess the changes in position of the particles along the z-axis. Therefore, a better observation strategy would be invaluable to study the possible precision of the platform.

Furthermore, the implementation of a closed loop control scheme with real time feedback of the position of a target particle would allow the user (or a trained artificial intelligence) to dynamically change the configuration of the microelectrodes that apply the DEP signal to give even greater precision.

The possible use of this micro platform to solve micromanipulation problems, such as the generation of custom samples of engineered biological tissue or the precise positioning of critical cell types in specific places of a micro scaffold, turns this technology in an exciting opportunity for the development of next generation tools aimed to aid the sciences of life.

▪ REFERENCES

- [1] B. F. Brehm-stecher and E. A. Johnson, "Single-Cell Microbiology: Tools, Technologies, and Applications," *Microbiol. Mol. Biol. Rev.*, vol. 68, no. 3, pp. 538–559, 2004.
- [2] R. Martinez-Duarte, P. Renaud, and M. J. Madou, "A novel approach to dielectrophoresis using carbon electrodes," *Electrophoresis*, vol. 32, no. 17, pp. 2385–2392, 2011.
- [3] C. Qian *et al.*, "Dielectrophoresis for bioparticle manipulation," *Int. J. Mol. Sci.*, vol. 15, no. 10, pp. 18281–18309, 2014.
- [4] H. Morgan, M. P. Hughes, and N. G. Green, "Separation of submicron bioparticles by dielectrophoresis," *Biophys. J.*, vol. 77, no. 1, pp. 516–525, 1999.
- [5] R. Pethig and G. H. Markx, "Applications of dielectrophoresis in biotechnology," *Trends Biotechnol.*, vol. 15, no. 10, pp. 426–432, 1997.
- [6] B. H. Lapizco-Encinas, B. a. Simmons, E. B. Cummings, and Y. Fintschenko, "Dielectrophoretic Concentration and Separation of Live and Dead Bacteria in an Array of Insulators," *Anal. Chem.*, vol. 76, no. 6, pp. 1571–1579, 2004.
- [7] C. H. Tai, S. K. Hsiung, C. Y. Chen, M. L. Tsai, and G. Bin Lee, "Automatic microfluidic platform for cell separation and nucleus collection," *Biomed. Microdevices*, vol. 9, no. 4, pp. 533–543, 2007.
- [8] D. F. Chen, H. Du, and W. H. Li, "Bioparticle separation and manipulation using dielectrophoresis," *Sensors Actuators, A Phys.*, vol. 133, no. 2 SPEC. ISS., pp. 329–334, 2007.
- [9] R. S. Thomas, H. Morgan, and N. G. Green, "Negative DEP traps for single cell immobilisation," *Lab Chip*, vol. 9, no. 11, pp. 1534–1540, 2009.
- [10] F. Grom, J. Kentsch, T. Müller, T. Schnelle, and M. Stelzle, "Accumulation and trapping of hepatitis A virus particles by electrohydrodynamic flow and dielectrophoresis," *Electrophoresis*, vol. 27, no. 7, pp. 1386–1393, 2006.
- [11] J. Voldman, R. a Braff, M. Toner, M. L. Gray, and M. a Schmidt, "Holding forces of single-particle dielectrophoretic traps," *Biophys. J.*, vol. 80, no. 1, pp. 531–541, 2001.
- [12] S. Bhattacharya *et al.*, "Selective trapping of single mammalian breast cancer cells by insulator-based dielectrophoresis," *Anal. Bioanal. Chem.*, vol. 406, no. 7, pp. 1855–65, Mar. 2014.
- [13] T. P. Hunt, D. Issadore, and R. M. Westervelt, "Integrated circuit/microfluidic chip to programmably trap and move cells and droplets with dielectrophoresis," *Lab Chip*, vol. 8, no. 1, pp. 81–87, 2008.
- [14] J. Suehiro and R. Pethig, "1998-The dielectrophoretic movement and positioning of a biological cell using a three-dimensional grid electro.pdf," vol. 3298.

- [15] J. Suehiro and R. Pethig, "The dielectrophoretic movement and positioning of a biological cell using a three-dimensional grid electrode system," *J. Phys. D. Appl. Phys.*, vol. 31, no. 22, pp. 3298–3305, 1998.
- [16] D. Das, K. Biswas, and S. Das, "A microfluidic device for continuous manipulation of biological cells using dielectrophoresis.," *Med. Eng. Phys.*, vol. 36, no. 6, pp. 726–31, Jun. 2014.
- [17] P. Tathireddy, Y. H. Choi, and M. Skliar, "Particle AC electrokinetics in planar interdigitated microelectrode geometry," *J. Electrostat.*, vol. 66, no. 11–12, pp. 609–619, 2008.
- [18] A. Ramos, *Electrokinetics and electrohydrodynamics in microsystems*. 2011.
- [19] H. A. Pohl, "The Motion and Precipitation of Suspensoids in Divergent Electric Fields," *Appl. Phys.*, 1951.
- [20] T. B. Jones, "Basic Theory of Dielectrophoresis and Electrorotation," *IEE Eng. Med. Biol. Mag.*, no. December, pp. 33–42, 2003.
- [21] K. Khoshmanesh *et al.*, "Dielectrophoretic manipulation and separation of microparticles using curved microelectrodes," *Electrophoresis*, vol. 30, no. 21, pp. 3707–3717, 2009.
- [22] H. A. Pohl, *Dielectrophoresis: The Behavior of Neutral Matter in Nonuniform Electric Fields*. Cambridge University Press, 1978.
- [23] Z. R. Gagnon, "Cellular dielectrophoresis: Applications to the characterization, manipulation, separation and patterning of cells," *Electrophoresis*, vol. 32, no. 18, pp. 2466–2487, 2011.
- [24] J. A. Stratton, *Electromagnetic Theory*. 1941.
- [25] E. Kreyszig, *Advanced Engineering Mathematics*, 9th ed. 2006.
- [26] G. James, *Matematicas Avanzadas para Ingenieria*. 2002.
- [27] C.-T. Tai, *General Vector and Dyadic Analysis: Applied Mathematics in Field Theory*, 2nd ed. 1997.
- [28] T. B. Jones and M. Washizu, "Multipolar dielectrophoretic and electrorotation theory," *J. Electrostat.*, vol. 37, no. 1–2, pp. 121–134, 1996.
- [29] R. Pethig, "Dielectrophoresis: status of the theory, technology, and applications," *Biomicrofluidics*, vol. 4, no. 2, pp. 1–35, Jan. 2010.
- [30] R. Pethig, A. Menachery, S. Pells, and P. De Sousa, "Dielectrophoresis: A review of applications for stem cell research," *J. Biomed. Biotechnol.*, vol. 2010, p. 182581, Jan. 2010.
- [31] L. Wang, *Advances in Transport Phenomena 2011*. 2011.
- [32] T. B. Jones, *Electromechanics of Particles*. Cambridge University Press, 2005.

- [33] J. Kirby, Brian, *Micro - and Nanoscale Fluid Mechanics*. Cambridge, 2010.
- [34] F. White, *Fluid Mechanics*. 2010.
- [35] H.-H. Cui, J. Voldman, X.-F. He, and K.-M. Lim, "Separation of particles by pulsed dielectrophoresis," *Lab Chip*, vol. 9, no. 16, p. 2306, 2009.
- [36] F. F. Becker, X. B. Wang, Y. Huang, R. Pethig, J. Vykoukal, and P. R. Gascoyne, "Separation of human breast cancer cells from blood by differential dielectric affinity.," *Proc. Natl. Acad. Sci. U. S. A.*, vol. 92, no. 3, pp. 860–864, 1995.
- [37] P. R. C. Gascoyne, X. B. Wang, Y. Huang, and R. F. Becker, "Dielectrophoretic separation of cancer cells from blood," *IEEE Trans. Ind. Appl.*, vol. 33, no. 3, pp. 670–678, 1997.
- [38] E. Choi, B. Kim, and J. Park, "High-throughput microparticle separation using gradient traveling wave dielectrophoresis," *J. Micromechanics Microengineering*, vol. 19, no. 12, p. 125014, Dec. 2009.
- [39] P. R. C. Gascoyne and J. V. Vykoukal, "Dielectrophoresis-based sample handling in general-purpose programmable diagnostic instruments," *Proc. IEEE*, vol. 92, no. 1, pp. 22–42, 2004.
- [40] I. Doh and Y. H. Cho, "A continuous cell separation chip using hydrodynamic dielectrophoresis (DEP) process," *Sensors Actuators, A Phys.*, vol. 121, no. 1, pp. 59–65, 2005.
- [41] K. Khoshmanesh, C. Zhang, S. Nahavandi, S. Baratchi, A. Mitchell, and K. Kalantar-zadeh, "Dielectrophoretically patterned carbon nanotubes to sort microparticles," *Electrophoresis*, vol. 31, no. 20, pp. 3380–3390, 2010.
- [42] D. S. Gray, J. L. Tan, J. Voldman, and C. S. Chen, "Dielectrophoretic registration of living cells to a microelectrode array," *Biosens. Bioelectron.*, vol. 19, no. 7, pp. 771–780, 2004.
- [43] L. Yang *et al.*, "A multifunctional micro-fluidic system for dielectrophoretic concentration coupled with immuno-capture of low numbers of *Listeria monocytogenes.*," *Lab Chip*, vol. 6, no. 7, pp. 896–905, 2006.
- [44] L. Wang, L. a Flanagan, E. Monuki, N. L. Jeon, and A. P. Lee, "Dielectrophoresis switching with vertical sidewall electrodes for microfluidic flow cytometry.," *Lab Chip*, vol. 7, no. 9, pp. 1114–1120, 2007.
- [45] Y. Huang, X. B. Wang, F. F. Becker, and P. R. Gascoyne, "Introducing dielectrophoresis as a new force field for field-flow fractionation.," *Biophys. J.*, vol. 73, no. 2, pp. 1118–1129, 1997.
- [46] K. Khoshmanesh *et al.*, "Size based separation of microparticles using a dielectrophoretic activated system," *J. Appl. Phys.*, vol. 108, no. 3, 2010.
- [47] M. Urdaneta and E. Smela, "Multiple frequency dielectrophoresis," *Electrophoresis*, vol. 28, no. 18, pp. 3145–3155, 2007.

- [48] M. D. Vahey and J. Voldman, “High-Throughput Cell and Particle High-Throughput Cell and Particle Characterization,” *Electr. Eng.*, vol. 81, no. 7, pp. 2446–2455, 2009.
- [49] X. Hu, P. H. Bessette, J. Qian, C. D. Meinhart, P. S. Daugherty, and H. T. Soh, “Marker-specific sorting of rare cells using dielectrophoresis.,” *Proc. Natl. Acad. Sci. U. S. A.*, vol. 102, no. 44, pp. 15757–15761, 2005.
- [50] Y. Huang, R. Hölzel, R. Pethig, and X. B. Wang, “Differences in the AC electrodynamics of viable and non-viable yeast cells determined through combined dielectrophoresis and electrorotation studies.,” *Phys. Med. Biol.*, vol. 37, no. 7, pp. 1499–1517, 1992.
- [51] K. Khoshmanesh, S. Nahavandi, S. Baratchi, A. Mitchell, and K. Kalantar-zadeh, “Dielectrophoretic platforms for bio-microfluidic systems,” *Biosens. Bioelectron.*, vol. 26, no. 5, pp. 1800–1814, Jan. 2011.
- [52] J. Auerswald and H. F. Knapp, “Quantitative assessment of dielectrophoresis as a micro fluidic retention and separation technique for beads and human blood erythrocytes,” *Microelectron. Eng.*, vol. 67–68, pp. 879–886, 2003.
- [53] W. Choi, J. S. Kim, D. H. Lee, K. K. Lee, D. B. Koo, and J. K. Park, “Dielectrophoretic oocyte selection chip for in vitro fertilization,” *Biomed. Microdevices*, vol. 10, no. 3, pp. 337–345, 2008.
- [54] W. Mike Arnold and N. R. Franich, “Cell isolation and growth in electric-field defined micro-wells,” *Curr. Appl. Phys.*, vol. 6, no. 3, pp. 371–374, 2006.
- [55] F. E. H. Tay, L. Yu, A. J. Pang, and C. Iliescu, “Electrical and thermal characterization of a dielectrophoretic chip with 3D electrodes for cells manipulation,” *Electrochim. Acta*, vol. 52, no. 8 SPEC. ISS., pp. 2862–2868, 2007.
- [56] C. Zhang, K. Khoshmanesh, F. J. Tovar-Lopez, a. Mitchell, W. Wlodarski, and K. Klantar-Zadeh, “Dielectrophoretic separation of carbon nanotubes and polystyrene microparticles,” *Microfluid. Nanofluidics*, vol. 7, no. 5, pp. 633–645, 2009.
- [57] C.-F. Chou *et al.*, “Electrodeless dielectrophoresis of single- and double-stranded DNA.,” *Biophys. J.*, vol. 83, no. 4, pp. 2170–2179, 2002.
- [58] N. Demierre, T. Braschler, R. Muller, and P. Renaud, “Focusing and continuous separation of cells in a microfluidic device using lateral dielectrophoresis,” *TRANSDUCERS EUROSENSORS '07 - 4th Int. Conf. Solid-State Sensors, Actuators Microsystems*, vol. 132, pp. 1777–1780, 2007.
- [59] B. H. Lapizco-Encinas, R. V. Davalos, B. a. Simmons, E. B. Cummings, and Y. Fintschenko, “An insulator-based (electrodeless) dielectrophoretic concentrator for microbes in water,” *J. Microbiol. Methods*, vol. 62, no. 3 SPEC. ISS., pp. 317–326, 2005.
- [60] P. Zellner, T. Shake, M. Agah, A. Sahari, and B. Behkam, “Off-chip electrode insulator based dielectrophoresis,” *Proc. IEEE Sensors*, pp. 3–6, 2012.
- [61] S. B. Asokan, L. Jawerth, R. L. Carroll, R. E. Cheney, S. Washburn, and R. Superfine,

- “Two-dimensional manipulation and orientation of actin-myosin systems with dielectrophoresis,” *Nano Lett.*, vol. 3, no. 4, pp. 431–437, 2003.
- [62] M. P. Hughes, H. Morgan, F. J. Rixon, J. P. Burt, and R. Pethig, “Manipulation of herpes simplex virus type 1 by dielectrophoresis.,” *Biochim. Biophys. Acta*, vol. 1425, no. 1, pp. 119–126, 1998.
- [63] K. C. Lan and L. S. Jang, “Integration of single-cell trapping and impedance measurement utilizing microwell electrodes,” *Biosens. Bioelectron.*, vol. 26, no. 5, pp. 2025–2031, 2011.
- [64] M. Washizu, T. B. Jones, and K. V Kaler, “Higher-order dielectrophoretic effects: levitation at a field null.,” *Biochim. Biophys. Acta*, vol. 1158, no. 1, pp. 40–46, 1993.
- [65] K. Khoshmanesh *et al.*, “Particle trapping using dielectrophoretically patterned carbon nanotubes,” *Electrophoresis*, vol. 31, no. 8, pp. 1366–1375, 2010.
- [66] K. Khoshmanesh *et al.*, “Dielectrophoretic-activated cell sorter based on curved microelectrodes,” *Microfluid. Nanofluidics*, vol. 9, no. 2–3, pp. 411–426, 2010.
- [67] F. Aldaeus, Y. Lin, G. Amberg, and J. Roeraade, “Multi-step dielectrophoresis for separation of particles,” *J. Chromatogr. A*, vol. 1131, no. 1–2, pp. 261–266, 2006.
- [68] P. R. C. Gascoyne and Jody Vykoukal, “Particle separation by dielectrophoresis,” *Electrophoresis*, vol. 23, no. 13, pp. 1973–1983, 2002.
- [69] H. Li and R. Bashir, “Dielectrophoretic separation and manipulation of live and heat-treated cells of *Listeria* on microfabricated devices with interdigitated electrodes,” *Sensors Actuators, B Chem.*, vol. 86, no. 2–3, pp. 215–221, 2002.
- [70] R. Krishnan, B. D. Sullivan, R. L. Mifflin, S. C. Esener, and M. J. Heller, “Alternating current electrokinetic separation and detection of DNA nanoparticles in high-conductance solutions,” *Electrophoresis*, vol. 29, no. 9, pp. 1765–1774, 2008.
- [71] D. Issadore, T. Franke, K. a Brown, T. P. Hunt, and R. M. Westervelt, “High Voltage Dielectrophoretic and Magnetophoretic Hybrid Integrated Circuit / Microfluidic Chip.,” *J. Microelectromech. Syst.*, vol. 18, no. 6, pp. 1220–1225, 2009.
- [72] M. Bocchi *et al.*, “Dielectrophoretic trapping in microwells for manipulation of single cells and small aggregates of particles,” *Biosens. Bioelectron.*, vol. 24, no. 5, pp. 1177–1183, 2009.
- [73] N. Mittal, A. Rosenthal, and J. Voldman, “nDEP microwells for single-cell patterning in physiological media.,” *Lab Chip*, vol. 7, no. 9, pp. 1146–1153, 2007.
- [74] L. S. Jang, P. H. Huang, and K. C. Lan, “Single-cell trapping utilizing negative dielectrophoretic quadrupole and microwell electrodes,” *Biosens. Bioelectron.*, vol. 24, no. 12, pp. 3637–3644, 2009.
- [75] A. Rosenthal and J. Voldman, “Dielectrophoretic traps for single-particle patterning.,” *Biophys. J.*, vol. 88, no. 3, pp. 2193–2205, 2005.
- [76] M. S. Pommer *et al.*, “Dielectrophoretic separation of platelets from diluted whole

- blood in microfluidic channels,” *Electrophoresis*, vol. 29, no. 6, pp. 1213–1218, 2008.
- [77] N. Lewpiriyawong and C. Yang, “AC-dielectrophoretic characterization and separation of submicron and micron particles using sidewall AgPDMS electrodes,” *Biomicrofluidics*, vol. 6, no. 1, 2012.
- [78] N. Lewpiriyawong, C. Yang, and Y. C. Lam, “Continuous sorting and separation of microparticles by size using AC dielectrophoresis in a PDMS microfluidic device with 3-D conducting PDMS composite electrodes,” *Electrophoresis*, vol. 31, no. 15, pp. 2622–2631, 2010.
- [79] D. F. Chen, H. Du, and W. H. Li, “A 3D paired microelectrode array for accumulation and separation of microparticles,” *J. Micromechanics Microengineering*, vol. 16, no. 7, pp. 1162–1169, 2006.
- [80] M. Dürr, J. Kentsch, T. Müller, T. Schnelle, and M. Stelzle, “Microdevices for manipulation and accumulation of micro- and nanoparticles by dielectrophoresis,” *Electrophoresis*, vol. 24, no. 4, pp. 722–731, 2003.
- [81] U. Kim, J. Qian, S. a. Kenrick, P. S. Daugherty, and H. T. Soh, “Multitarget dielectrophoresis activated cell sorter,” *Anal. Chem.*, vol. 80, no. 22, pp. 8656–8661, 2008.
- [82] F. Aldaeus, Y. Lin, J. Roeraade, and G. Amberg, “Superpositioned dielectrophoresis for enhanced trapping efficiency,” *Electrophoresis*, vol. 26, no. 22, pp. 4252–4259, 2005.
- [83] H. Shafiee, J. L. Caldwell, M. B. Sano, and R. V Davalos, “Contactless dielectrophoresis: a new technique for cell manipulation.,” *Biomed. Microdevices*, vol. 11, no. 5, pp. 997–1006, Oct. 2009.
- [84] H. Shafiee, M. B. Sano, E. a Henslee, J. L. Caldwell, and R. V Davalos, “Selective isolation of live/dead cells using contactless dielectrophoresis (cDEP).,” *Lab Chip*, vol. 10, no. 4, pp. 438–445, 2010.
- [85] J. Voldman, M. L. Gray, M. Toner, and M. A. Schmidt, “A Microfabrication-Based Dynamic Array Cytometer parallel luminescent single-cell assays that can sort popu-,” vol. 74, no. 16, pp. 3984–3990, 2016.
- [86] T. P. Hunt, H. Lee, and R. M. Westervelt, “Addressable micropost array for the dielectrophoretic manipulation of particles in fluid,” *Appl. Phys. Lett.*, vol. 85, no. 26, pp. 6421–6423, 2004.
- [87] J. Voldman, M. Toner, M. L. Gray, and M. a. Schmidt, “Design and analysis of extruded quadrupolar dielectrophoretic traps,” *J. Electrostat.*, vol. 57, no. 1, pp. 69–90, 2003.
- [88] P. Dixit and J. Miao, “High Aspect Ratio Vertical Through-Vias for 3D MEMS Packaging Applications by Optimized Three-Step Deep RIE,” *J. Electrochem. Soc.*, vol. 155, no. 2, p. H85, 2008.
- [89] D. Belavic, M. Hrovat, J. Holc, M. S. Zarnik, M. Kosec, and M. Pavlin, “The

- application of thick-film technology in C-MEMS,” *J. Electroceramics*, vol. 19, no. 4, pp. 363–368, 2007.
- [90] R. Martinez-Duarte, R. a Gorkin, K. Abi-Samra, and M. J. Madou, “The integration of 3D carbon-electrode dielectrophoresis on a CD-like centrifugal microfluidic platform,” *Lab Chip*, vol. 10, no. 8, pp. 1030–1043, 2010.
- [91] H. a Rouabah, B. Y. Park, R. B. Zaouk, H. Morgan, M. J. Madou, and N. G. Green, “Design and fabrication of an ac-electro-osmosis micropump with 3D high-aspect-ratio electrodes using only SU-8,” *J. Micromechanics Microengineering*, vol. 21, no. 3, p. 035018, 2011.
- [92] C. Wang and M. Madou, “From MEMS to NEMS with carbon,” *Biosens. Bioelectron.*, vol. 20, no. 10 SPEC. ISS., pp. 2181–2187, 2005.
- [93] S. Ranganathan, R. McCreery, S. M. Majji, and M. Madou, “Photoresist-Derived Carbon for Microelectromechanical Systems and Electrochemical Applications,” *J. Electrochem. Soc.*, vol. 147, no. 1, p. 277, 2000.
- [94] I. C. Gebeshuber, H. Stachelberger, B. A. Ganji, D. C. Fu, J. Yunas, and B. Y. Majlis, “Exploring the Innovational Potential of Biomimetics for Novel 3D MEMS,” *Adv. Mater. Res.*, vol. 74, pp. 265–268, 2009.
- [95] N. L. Pocard, D. C. Alsmeyer, R. L. McCreery, T. X. Neenan, and M. R. Callstrom, “Feature articles. Doped glassy carbon: a new material for electrocatalysis,” *J. Mater. Chem.*, vol. 2, no. 8, p. 771, 1992.
- [96] J. a Lee, S. W. S. S. Lee, K.-C. Lee, S. Il Park, and S. W. S. S. Lee, “Fabrication and characterization of freestanding 3D carbon microstructures using multi-exposures and resist pyrolysis,” *J. Micromechanics Microengineering*, vol. 18, no. 3, p. 035012, 2008.
- [97] C. Wang, G. Jia, L. H. Taherabadi, and M. J. Madou, “A novel method for the fabrication of high-aspect ratio C-MEMS structures,” *J. Microelectromechanical Syst.*, vol. 14, no. 2, pp. 348–358, 2005.
- [98] A. Rammohan, P. K. Dwivedi, R. Martinez-Duarte, H. Katepalli, M. J. Madou, and A. Sharma, “One-step maskless grayscale lithography for the fabrication of 3-dimensional structures in SU-8,” *Sensors Actuators, B Chem.*, vol. 153, no. 1, pp. 125–134, 2011.
- [99] L. Mosher, C. M. Waits, B. Morgan, and R. Ghodssi, “Double-exposure grayscale photolithography,” *J. Microelectromechanical Syst.*, vol. 18, no. 2, pp. 308–315, 2009.
- [100] K. Totsu, K. Fujishiro, S. Tanaka, and M. Esashi, “Fabrication of three-dimensional microstructure using maskless gray-scale lithography,” *Sensors Actuators, A Phys.*, vol. 130–131, no. SPEC. ISS., pp. 387–392, 2006.
- [101] J. Kim, X. Song, K. Kinoshita, M. Madou, and B. White, “Electrochemical Studies of Carbon Films from Pyrolyzed Photoresist,” *J. Electrochem. Soc.*, vol. 145, no. 7, p. 2314, 1998.

- [102] A. Singh, J. Jayaram, M. Madou, and S. Akbar, "Pyrolysis of Negative Photoresists to Fabricate Carbon Structures for Microelectromechanical Systems and Electrochemical Applications," *J. Electrochem. Soc.*, vol. 149, no. 3, p. E78, 2002.
- [103] R. Natu, M. Islam, J. Gilmore, and R. Martinez-Duarte, "Shrinkage of SU-8 microstructures during carbonization," *J. Anal. Appl. Pyrolysis*, vol. 131, pp. 17–27, 2018.
- [104] M. Ghazinejad, S. Holmberg, O. Pilloni, L. Oropeza-Ramos, and M. Madou, "Graphitizing Non-graphitizable Carbons by Stress-induced Routes," *Sci. Rep.*, vol. 7, no. 1, 2017.
- [105] R. Pörtner, "Characteristics of Mammalian Cells and Requirements for Cultivation," in *Cell and Tissue Reaction Engineering: With a Contribution by Martin Fussenegger and Wilfried Weber*, Berlin, Heidelberg: Springer Berlin Heidelberg, 2009, pp. 13–53.
- [106] A. Ramos, H. Morgan, N. G. Green, and A. Castellanos, "Ac electrokinetics: a review of forces in microelectrode structures Dielectrophoretic investigations of sub-micrometre latex spheres N G Green and H Morgan - Ac electrokinetics: a survey of sub- micrometre particle dynamics," *J. Phys. D. Appl. Phys.*, vol. 31, pp. 2338–2353, 1998.
- [107] N. Crews, J. Darabi, P. Voglewede, F. Guo, and a. Bayoumi, "An analysis of interdigitated electrode geometry for dielectrophoretic particle transport in microfluidics," *Sensors Actuators, B Chem.*, vol. 125, no. 2, pp. 672–679, 2007.
- [108] O. Pilloni *et al.*, "Micro Device for Bio-Particle Positioning in a 3D space based on Carbon MEMS and Dielectrophoretic Forces," *ECS Trans.*, vol. 72, no. 31, pp. 17–24, 2016.

▪ APPENDIX A: ELECTRIC POTENTIAL INDUCED BY CHARGE DISTRIBUTION

We start by defining a point charge q placed on the z -axis at a distance ζ from the origin ($q = q(0,0, \zeta)$) of a tridimensional coordinate system, illustrated in Fig. 43. The electric potential $\phi(\mathbf{r}, \theta)$ of an arbitrary point in space \mathbf{P} induced by q is given by eq. (39) due to field symmetry.

$$\phi(\mathbf{r}, \theta) = \left(\frac{q}{4\pi\epsilon}\right) \left(\frac{1}{r_2}\right) \quad (39)$$

The distance from q to \mathbf{P} (r_2) can be expressed in terms of \mathbf{r} as eq. (40).

$$r_2 = \sqrt{r^2 + \zeta^2 - 2r\zeta \cos \theta} \quad (40)$$

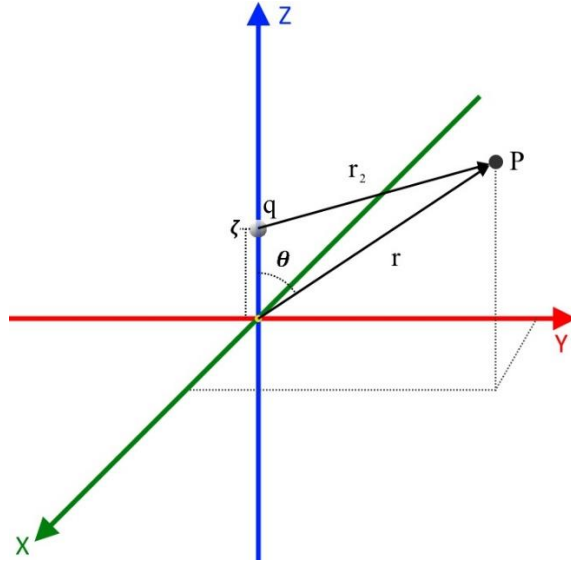


Fig. 43: Point charge q placed on the z -axis and arbitrary point \mathbf{P} where the electric potential needs to be calculated.

Now, if we define a sphere that represents a dielectric particle with center in the origin and radius ζ . Two cases arise depending if the electric potential needed lies inside or outside the particle.

The case of an electric potential inside the particle is of little interest in the present work due to the dipole moment being mainly affected by the external potentials induced by the particle. The reader can find more information about this case in the text about electromagnetic theory by J. Stratton [24].

In the case where \mathbf{P} resides outside the particle ($r > \zeta$), eq. (40) can be rewritten to obtain the reciprocal $\frac{1}{r_2}$, giving eq. (41).

$$\frac{1}{r_2} = \frac{1}{\sqrt{r^2 \left(1 + \frac{\zeta^2}{r^2} - \frac{2r\zeta}{r^2} \cos \theta\right)}} = \frac{1}{r} \left[1 + \left(\frac{\zeta}{r}\right)^2 - 2\left(\frac{\zeta}{r}\right) \cos \theta\right]^{-\frac{1}{2}} \quad (41)$$

Eq. (41) can be expanded by the binomial theorem if eq. (42) holds true, which gives eq. (43).

$$\left| \left(\frac{\zeta}{r}\right)^2 - 2\left(\frac{\zeta}{r}\right) \cos \theta \right| < 1 \quad (42)$$

$$\frac{1}{r_2} = \frac{1}{r} \sum_{n=0}^{\infty} P_n(\cos \theta) \left(\frac{\zeta}{r}\right)^n \quad (43)$$

The coefficients $P_n(\cos \theta)$ in eq. (43) are given by the Legendre polynomials [25]:

$$P_0(\cos \theta) = 1$$

$$P_1(\cos \theta) = \cos \theta$$

$$P_2(\cos \theta) = \frac{1}{2}(3 \cos^2 \theta - 1)$$

$$P_3(\cos \theta) = \frac{1}{2}(5 \cos^3 \theta - 3 \cos \theta)$$

$$P_4(\cos \theta) = \frac{1}{8}(35 \cos^4 \theta - 30 \cos^2 \theta + 3)$$

$$P_5(\cos \theta) = \dots$$

Substituting eq. (43) into eq. (39) gives eq. (44), which describes the electric potential at a point \mathbf{P} outside the particle.

$$\phi = \left(\frac{q}{4\pi\epsilon}\right) \frac{1}{r} \sum_{n=0}^{\infty} P_n(\cos\theta) \left(\frac{\zeta}{r}\right)^n \quad (44)$$

It is possible to obtain an expression that more closely resembles a real particle by replacing the point charge by a line charge placed at the z-axis, with length l , and a charge density $\rho = \rho(\zeta)$ with a total charge distribution q described by eq. (45). Substituting this expression in eq. (44) gives eq. (46).

$$q = \int_0^l \rho(\zeta) d\zeta \quad (45)$$

$$\phi = \left(\frac{1}{4\pi\epsilon}\right) \sum_{n=0}^{\infty} \int_0^l \rho(\zeta) \zeta^n d\zeta \frac{1}{r^{n+1}} P_n(\cos\theta) \quad (46)$$

Equation (46) represents the electric potential in a point of space outside a particle due to a net charge composed of n multipoles. Another way to interpret this result is by expressing it as the individual electric potential contribution by each $P_n(\cos\theta)$ element (eq. (47)).

$$\phi_n = \left(\frac{1}{4\pi\epsilon}\right) \frac{P_n(\cos\theta)}{r^{n+1}} \int_0^l \rho(\zeta) \zeta^n d\zeta = \left(\frac{1}{4\pi\epsilon}\right) \frac{P_n(\cos\theta)}{r^{n+1}} \mathbf{p}_n \quad (47)$$

From eq. (47) we define the quantity \mathbf{p}_n which represents the n th-order axial multipole (eq. (48)).

$$\mathbf{p}_n = \int_0^l \rho(\zeta) \zeta^n d\zeta \quad (48)$$

To generalize eq. (47) for a charge element localized in an arbitrary location $\bar{\delta}(\xi, \eta, \zeta)$ inside the particle, we substitute the position vector $\bar{\mathbf{r}}$ by $\bar{\mathbf{r}} - \bar{\delta}$ noting that $\mathbf{r} = \sqrt{\mathbf{x}^2 + \mathbf{y}^2 + \mathbf{z}^2}$, $\delta = \sqrt{\xi^2 + \eta^2 + \zeta^2}$, and a differential part of the electric potential is described by eq. (49).

$$d\phi = \left(\frac{1}{4\pi\epsilon} \right) \frac{dq}{\sqrt{(x - \xi)^2 + (y - \eta)^2 + (z - \zeta)^2}} \quad (49)$$

The denominator of eq. (49) can be expanded by the Taylor series [26] to obtain a series of coefficients \mathbf{p}'_n . By integrating this expression its evident that the electric potential is $\int d\phi = \phi = \sum_{n=0}^{\infty} \phi_n$, where each ϕ_n element is given by eq. (50).

$$\phi_n = \left(\frac{1}{4\pi\epsilon} \right) \mathbf{p}'_n \quad (50)$$

The \mathbf{p}'_n coefficients of eq. (50) are given by:

$$\mathbf{p}'_0 = \int \left(\frac{1}{\mathbf{r}} \right) dq = \frac{1}{\mathbf{r}} \int \rho dv$$

$$\begin{aligned} \mathbf{p}'_1 &= - \int \left[\xi \frac{\partial}{\partial x} \left(\frac{1}{\mathbf{r}} \right) + \eta \frac{\partial}{\partial y} \left(\frac{1}{\mathbf{r}} \right) + \zeta \frac{\partial}{\partial z} \left(\frac{1}{\mathbf{r}} \right) \right] dq \\ &= - \left[\frac{\partial}{\partial x} \left(\frac{1}{\mathbf{r}} \right) \int [\xi \rho] dv + \frac{\partial}{\partial y} \left(\frac{1}{\mathbf{r}} \right) \int [\eta \rho] dv + \frac{\partial}{\partial z} \left(\frac{1}{\mathbf{r}} \right) \int [\zeta \rho] dv \right] \end{aligned}$$

$$\begin{aligned} \mathbf{p}'_2 &= \frac{1}{2} \int \left[\xi^2 \frac{\partial^2}{\partial x^2} \left(\frac{1}{\mathbf{r}} \right) + \eta^2 \frac{\partial^2}{\partial y^2} \left(\frac{1}{\mathbf{r}} \right) + \zeta^2 \frac{\partial^2}{\partial z^2} \left(\frac{1}{\mathbf{r}} \right) + 2\xi\eta \frac{\partial^2}{\partial x \partial y} \left(\frac{1}{\mathbf{r}} \right) + 2\eta\zeta \frac{\partial^2}{\partial y \partial z} \left(\frac{1}{\mathbf{r}} \right) \right. \\ &\quad \left. + 2\zeta\xi \frac{\partial^2}{\partial z \partial x} \left(\frac{1}{\mathbf{r}} \right) \right] dq \\ &= \frac{1}{2} \left[\frac{\partial^2}{\partial x^2} \left(\frac{1}{\mathbf{r}} \right) \int [\xi^2 \rho] dv + \frac{\partial^2}{\partial y^2} \left(\frac{1}{\mathbf{r}} \right) \int [\eta^2 \rho] dv + \frac{\partial^2}{\partial z^2} \left(\frac{1}{\mathbf{r}} \right) \int [\zeta^2 \rho] dv \right. \\ &\quad \left. + \frac{\partial^2}{\partial x \partial y} \left(\frac{1}{\mathbf{r}} \right) \int [2\xi\eta \rho] dv + \frac{\partial^2}{\partial y \partial z} \left(\frac{1}{\mathbf{r}} \right) \int [2\eta\zeta \rho] dv \right. \\ &\quad \left. + \frac{\partial^2}{\partial z \partial x} \left(\frac{1}{\mathbf{r}} \right) \int [2\zeta\xi \rho] dv \right] \end{aligned}$$

$$\mathbf{p}'_3 = -\frac{1}{6} \dots$$

The handle of these coefficients can be simplified by using the concept of interacting pairs or dyadics. The dyadic tensor of any two vectors $[\bar{a}(a_x, a_y, a_z), \bar{b}(b_x, b_y, b_z)]$ has the following structure:

$$\bar{a}\bar{b} = \begin{bmatrix} a_x b_x & a_x b_y & a_x b_z \\ a_y b_x & a_y b_y & a_y b_z \\ a_z b_x & a_z b_y & a_z b_z \end{bmatrix}$$

For the charge position vector $\bar{\delta}(\xi, \eta, \zeta)$, we have the following dyadic tensor:

$$\bar{\delta}\bar{\delta} = \begin{bmatrix} \xi^2 & \xi\eta & \xi\zeta \\ \eta\xi & \eta^2 & \eta\zeta \\ \zeta\xi & \zeta\eta & \zeta^2 \end{bmatrix}$$

The dyadic form of the Taylor series [27] is shown in eq. (51). The operation “:” is defined as $\bar{A}\bar{B}:\bar{C}\bar{D} \equiv \bar{A} \cdot \bar{B}\bar{C} \cdot \bar{D} = (\bar{A} \cdot \bar{C})(\bar{B} \cdot \bar{D})$.

$$\bar{f}(\bar{r} - \bar{\delta}) = \bar{f}(\bar{r}) - \bar{\delta} \cdot \nabla \bar{f}(\bar{r}) + \frac{1}{2!} \bar{\delta}\bar{\delta}:\nabla\nabla\bar{f}(\bar{r}) - \frac{1}{3!} \bar{\delta}\bar{\delta}\bar{\delta}:\nabla\nabla\nabla\bar{f}(\bar{r}) \dots \quad (51)$$

Applying eq. (51) to the position function $\bar{f}(\bar{r}) = \frac{1}{\bar{r}}$ when $\bar{r} \rightarrow \bar{r} - \bar{\delta}$ we obtain that the coefficients \mathbf{p}'_n can be rewritten in the form of eq. (52) [28], [29].

$$\mathbf{p}'_n = \frac{(-1)^n}{n!} \mathbf{p}_n [\cdot]^n (\nabla)^n \left(\frac{1}{\bar{r}} \right) \quad (52)$$

The operation $[\cdot]^n$ in eq. (52) represents the nth application of the dot product to the dyadic tensor, and $(\nabla)^n$ represents the application of n ∇ operators to the factor $\left(\frac{1}{\bar{r}}\right)$. Finally, eq. (53) is obtained by substituting eq. (52) in eq. (50) which gives the potential contribution of the nth-order multipole.

$$\phi_n = \frac{(-1)^n}{4\pi\epsilon n!} \frac{\mathbf{p}_n}{\bar{r}^{n+1}} [\cdot]^n (\nabla)^n \left(\frac{1}{\bar{r}} \right) \quad (53)$$

▪ APPENDIX B: VISCOSITY

Dynamic viscosity

The dynamic viscosity (μ) measures the resistance of the fluid to deformation. It also determines the speed of deformation that exists in the fluid, generated from the application of a shear stress.

When a shearing stress τ is applied to a plane of the fluid oriented on the x-axis, it will move at a speed u , generating a deformation angle θ with respect to another plane parallel to the previous one and separated by a distance dy . If the shear stress continues to be applied, the change in time of the deformation angle must be proportional to it (eq. (54)) A diagram of the variables involved is given in Fig. 44.

$$\tau \propto \frac{d\theta}{dt} \quad (54)$$

It is possible to demonstrate that this relationship is also affected by the change in velocity with respect to the position between both planes [34], obtaining an exact relation when using the dynamic viscosity as a constant of proportionality (eq. (55)).

$$\tau = \mu \frac{d\theta}{dt} = \mu \frac{du}{dy} \quad (55)$$

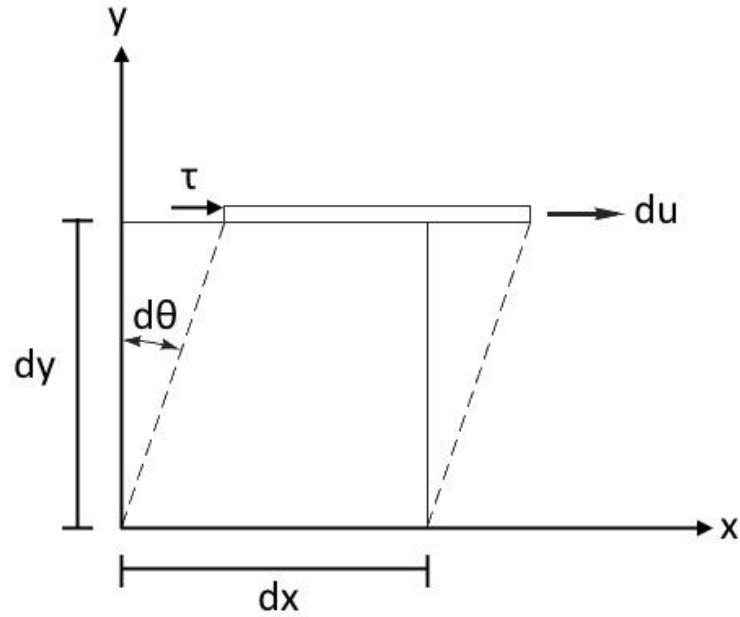


Fig. 44: Diagram of the variables involved in the definition of dynamic viscosity.

A useful example of the physical implications of the dynamic viscosity arises from considering two parallel plates of area A separated by a distance d with a fluid in between. If one of the plates is fixed and the other is subjected to a force \bar{F} in the x direction, the moving plate will move at a speed \bar{u} . This effect can be calculated using eq. (56) and is depicted in Fig. 45.

$$\bar{u} = \frac{\bar{F}d}{\mu A} \quad (56)$$

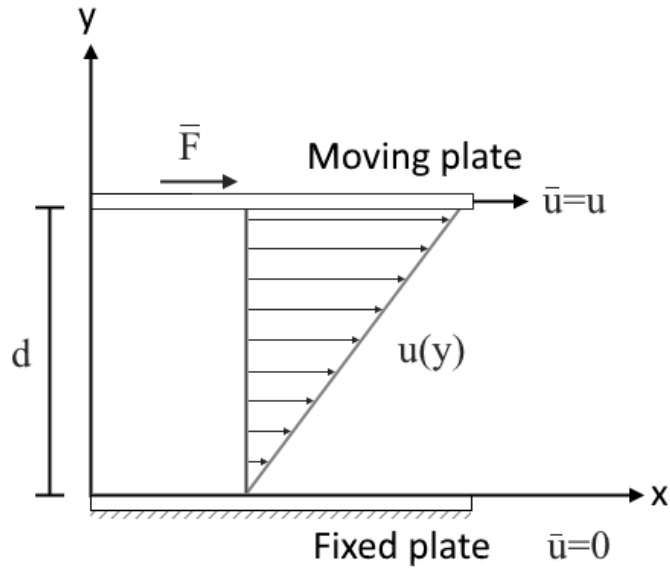


Fig. 45: Velocity profile of a fluid trapped in between a fixed and a moving plate.

Kinematic viscosity and specific weight

There are some quantities related to the density of the fluid which are useful in the study of flows for the simplification of expressions, two of them are the kinematic viscosity and the specific weight.

The kinematic viscosity (ν) is defined as the relationship between the dynamic viscosity of the fluid and its density (ρ).

$$\nu = \frac{\mu}{\rho} \quad (57)$$

The specific weight (γ) of a fluid results from the product of its density by the gravitational force (g) to which it is subjected.

$$\gamma = \rho g \quad (58)$$

■ APPENDIX C: MICROELECTRODE ARRAY DESIGNS AND FABRICATION PROTOCOLS

○ Design schematics

Layer 1: Electrical traces and pads

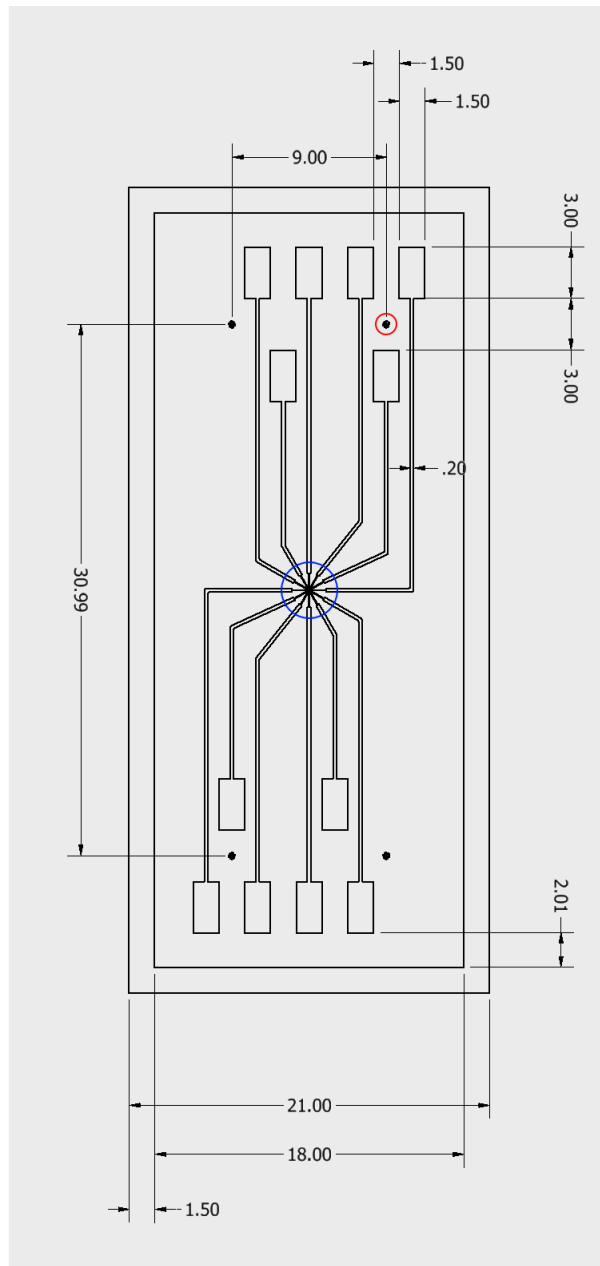


Fig. 46: Layer 1 [mm].

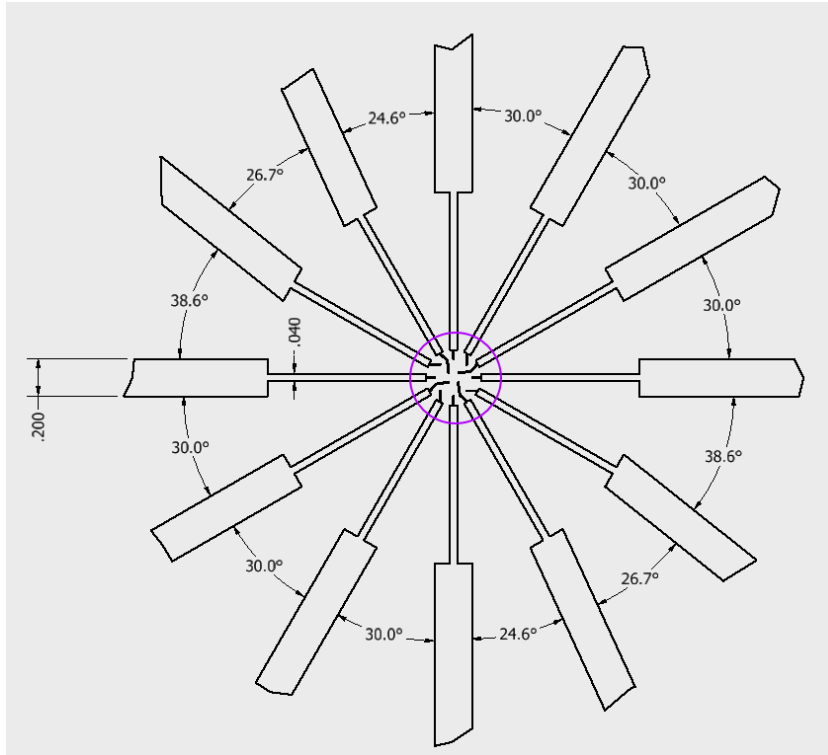


Fig. 47: Blue detail from layer 1 [mm].

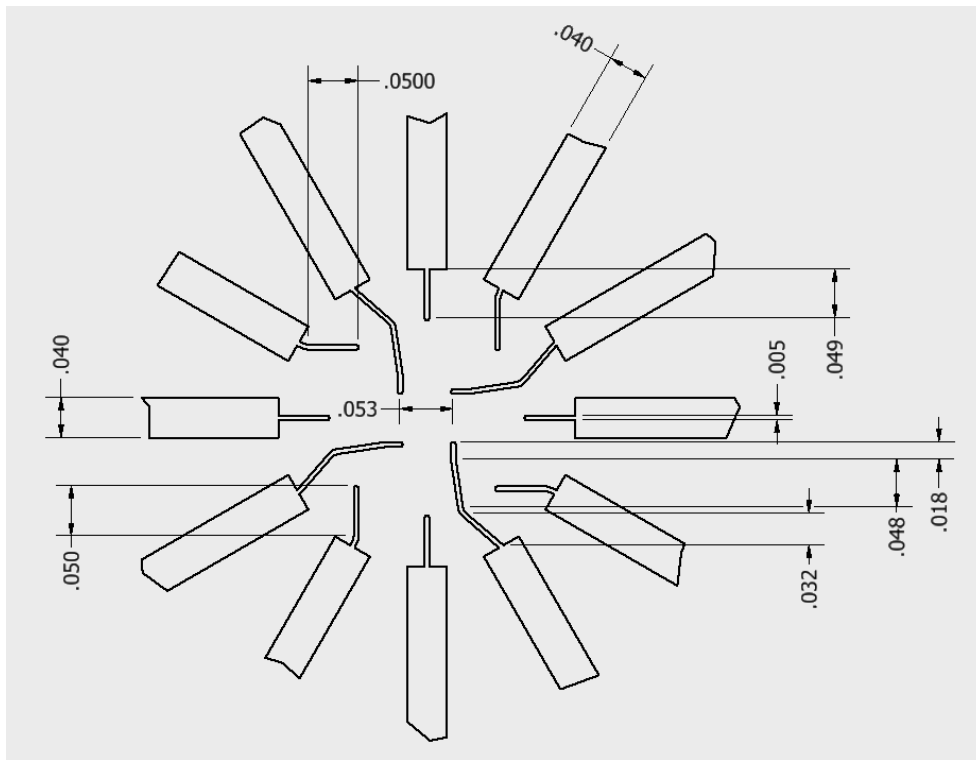


Fig. 48: Purple detail from Fig. 47 [mm].

Layer 2: 2D and 3D microelectrode bases

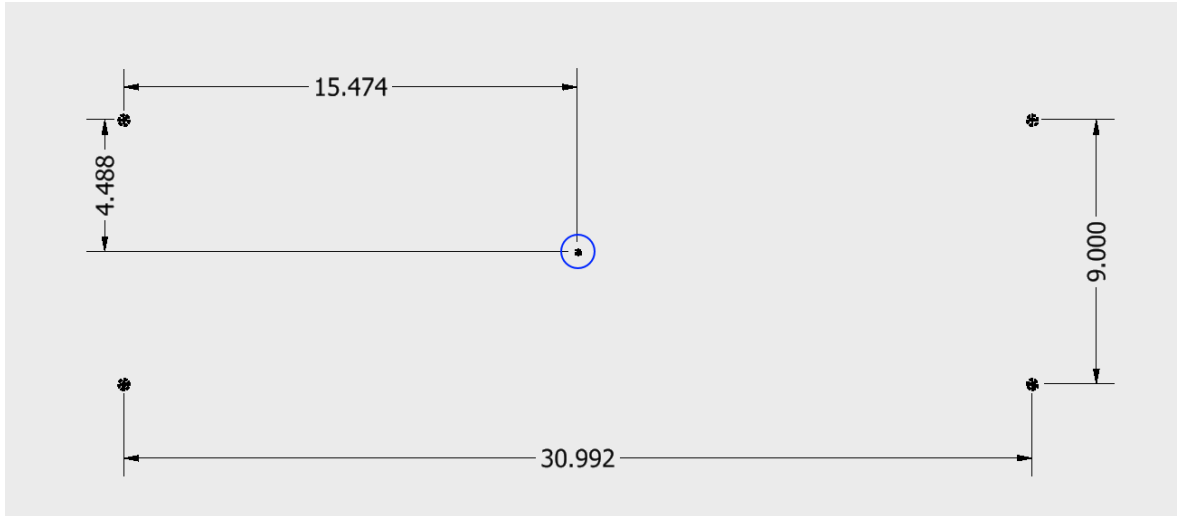


Fig. 49: Layer 2 [mm].

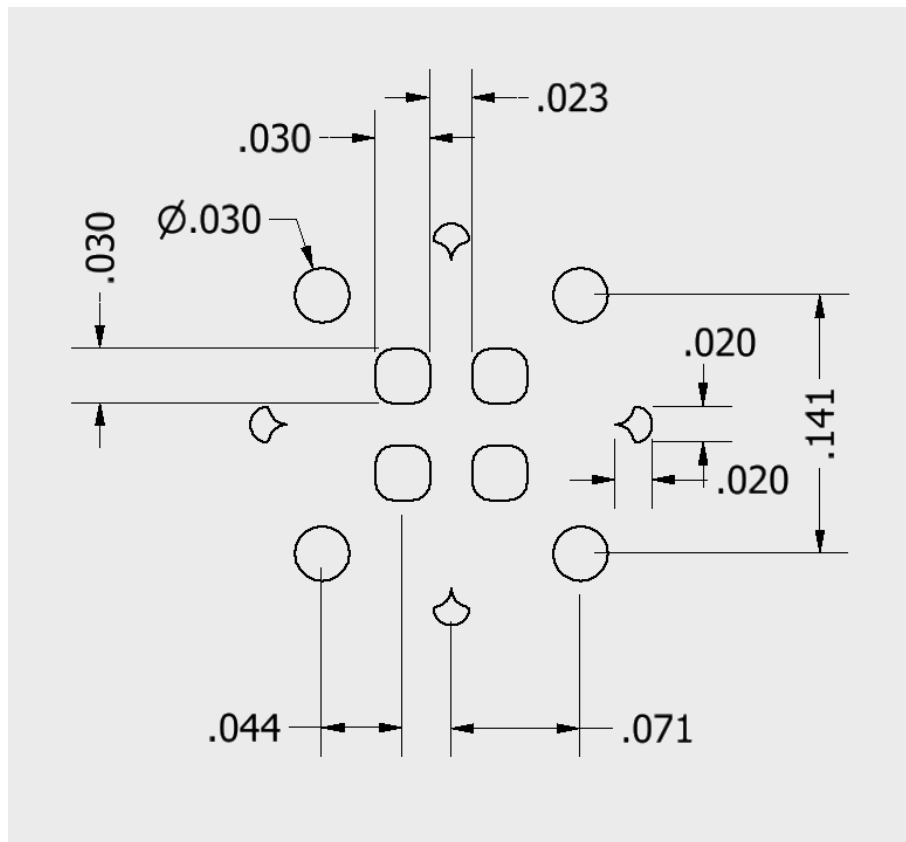


Fig. 50: Blue detail from layer 2 [mm].

Layer 3: 3D microelectrodes

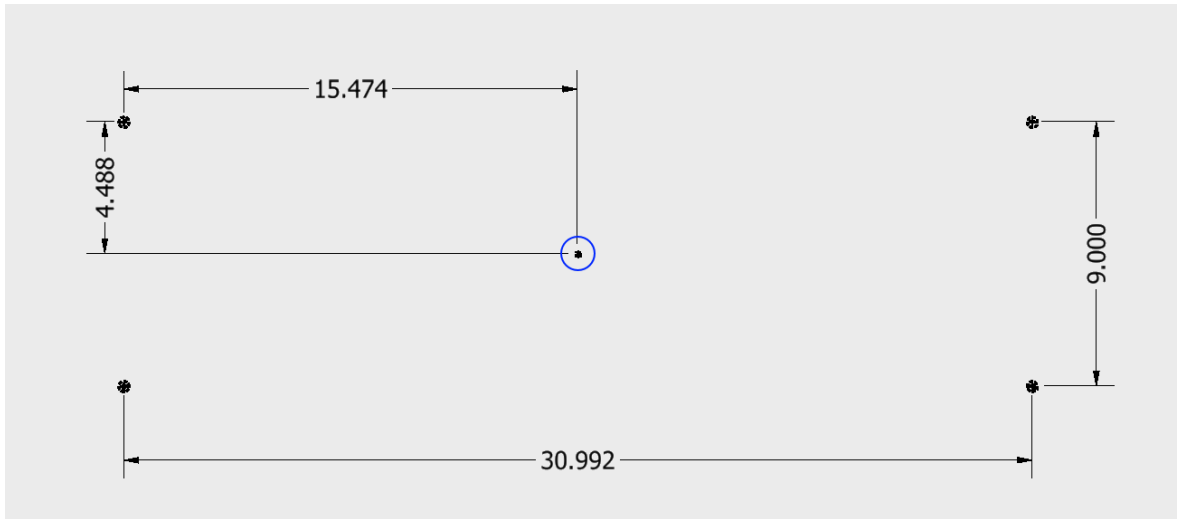


Fig. 51: Layer 3 [mm].

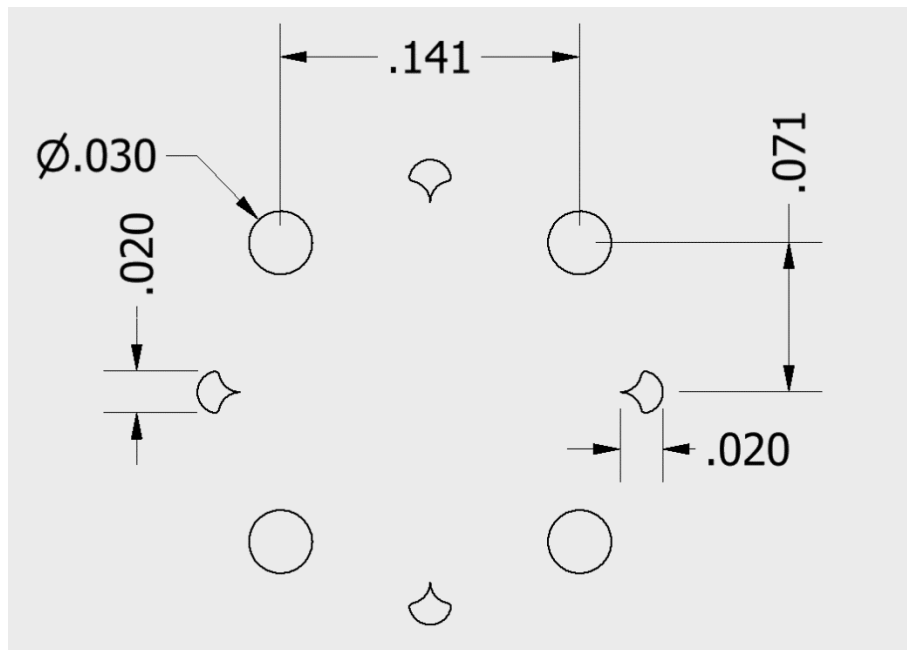


Fig. 52: Blue detail from layer 3 [mm].

Layer 4: Passivation

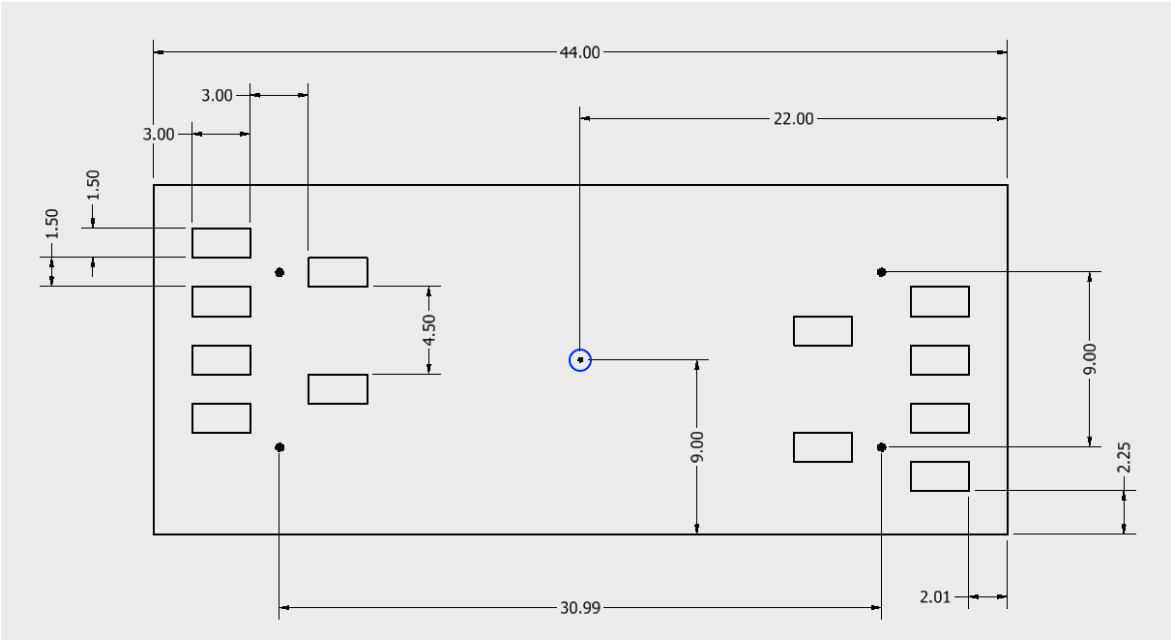


Fig. 53: Layer 4 [mm].

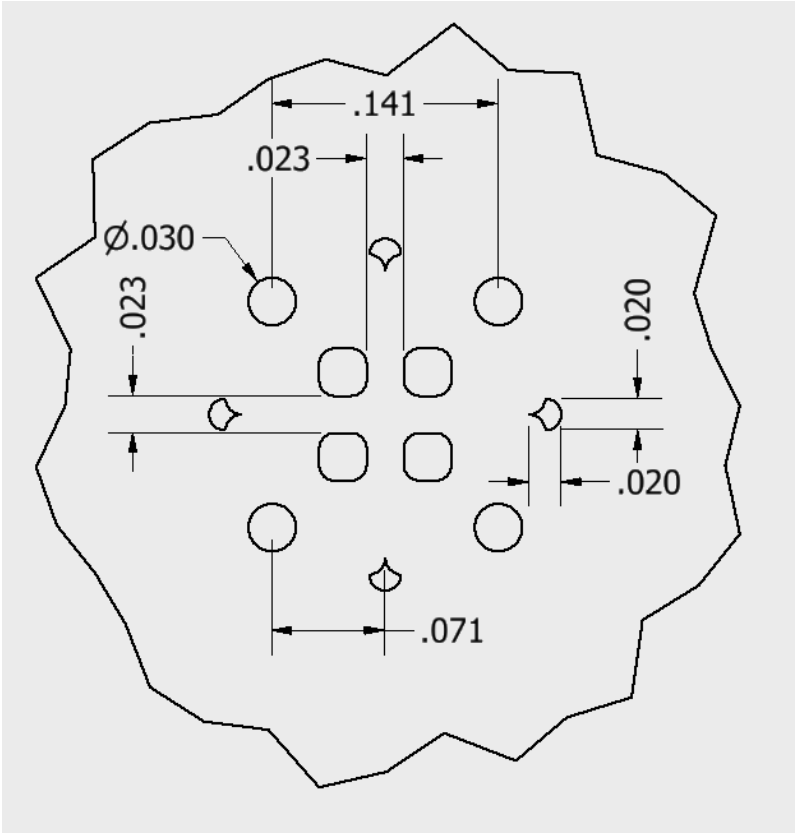


Fig. 54: Blue detail of layer 4 [mm]

Layer 5: Microchannel

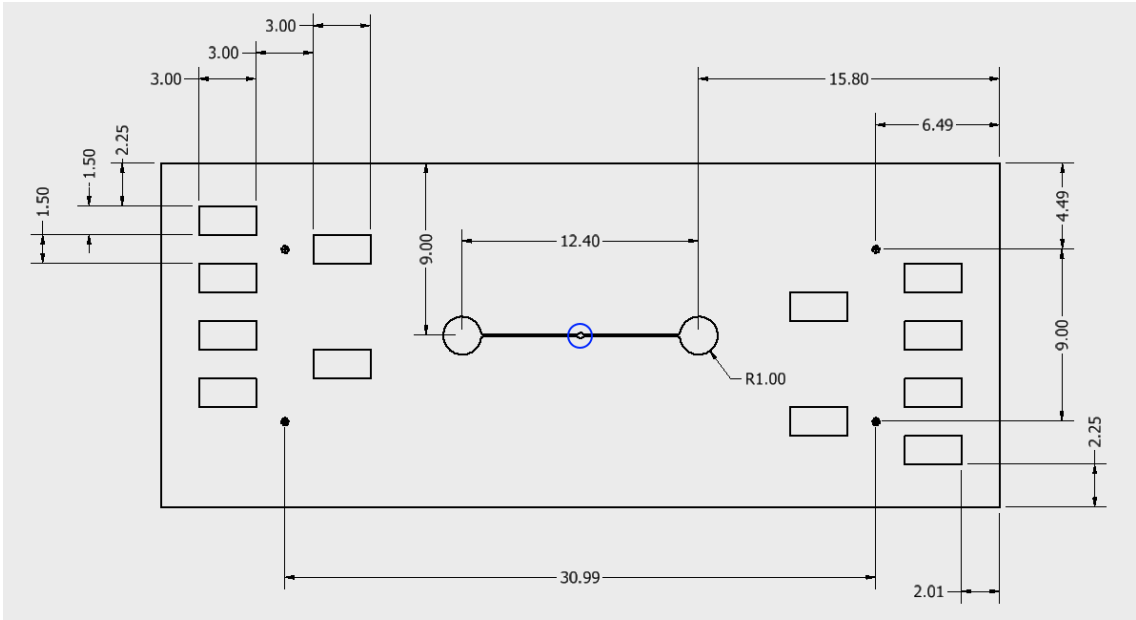


Fig. 55: Layer 5 [mm].

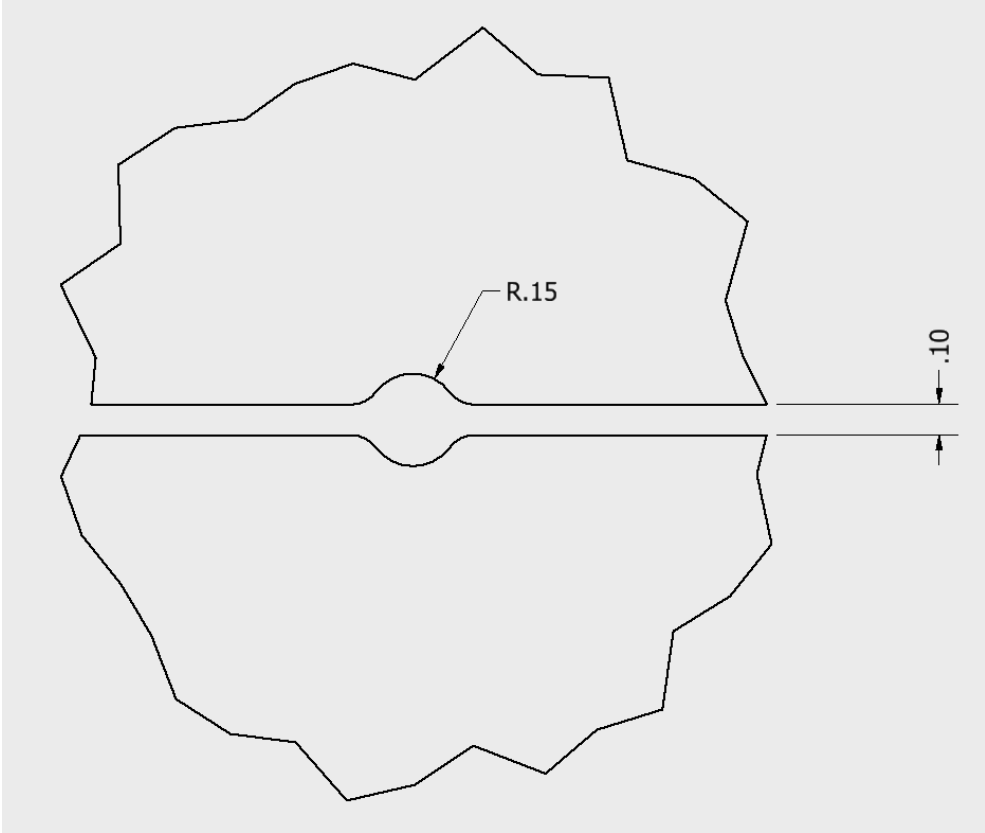


Fig. 56: Blue detail from layer 5 [mm].

○ Photolithography

A multilayer photolithography process was employed to fabricate the microelectrode array. This process is outlined in Fig. 57 and described in detail in this section.

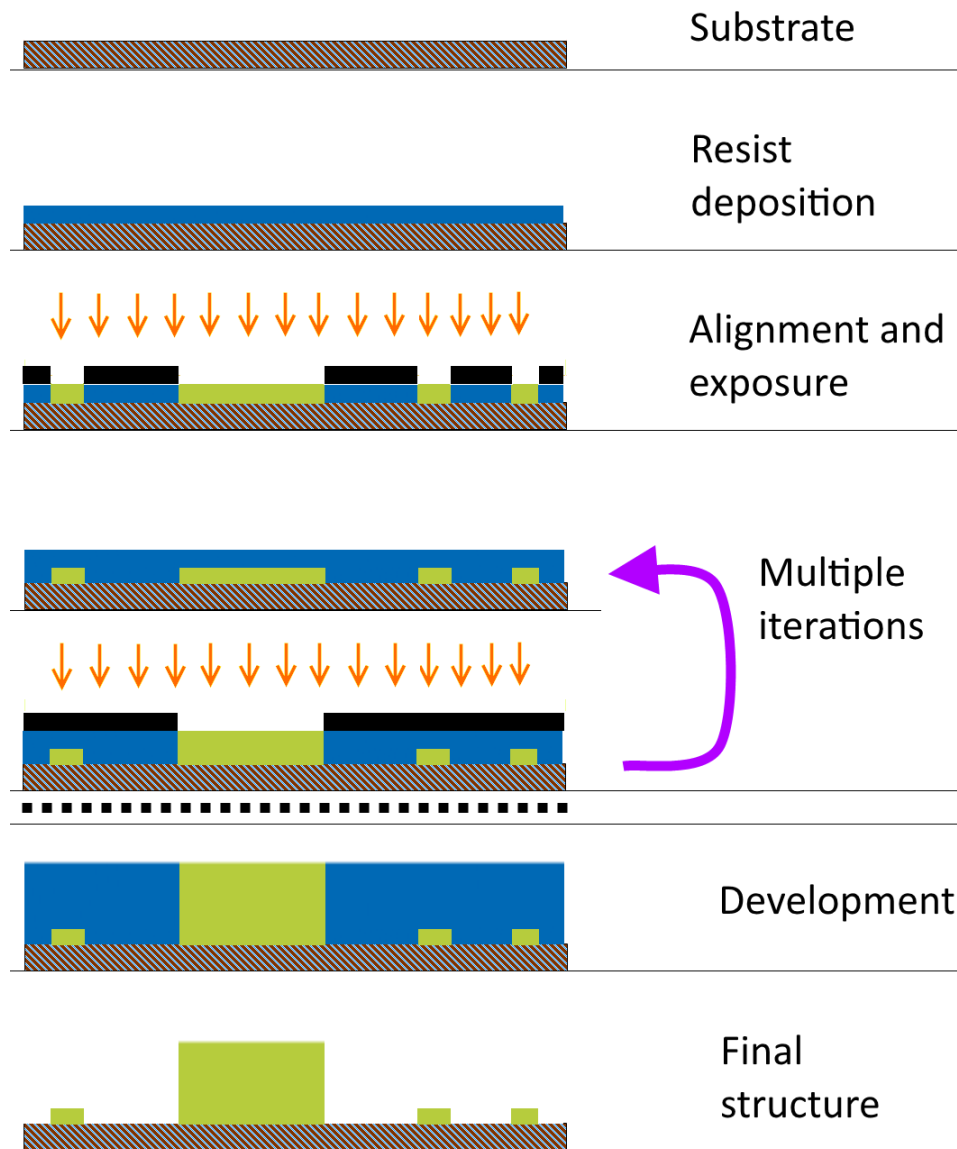


Fig. 57: Multilayer photolithography process.

Substrate Cleaning

To clean the substrate, a layer of acetone was sprayed on the surface of the substrate and then a spin coater was used to spin it at 2000 RPM. This process was repeated using isopropyl alcohol. The substrate was then placed on a hot plate at 230 °C for one hour to dehydrate it.

Finally, the substrate was removed from the hot plate and was placed directly on a Laurel spin coater and it was allowed to cool to room temperature (18 °C).

Photoresist deposition

The substrate was spin coated with SU-8 3035 using a two-step spin velocity program. Velocity was selected to produce the film thickness required by each design layer (Table IV).

Table IV: Spin coater parameters for photoresist deposition.

Layer	Thickness [μm]	Step 1	Step 2
1	35	15s @ 500 RPM	45s @ 4000 RPM
2	35	15s @ 500 RPM	45s @ 4000 RPM
3	100	15s @ 500 RPM	45s @ 1000 RPM
4	40	15s @ 500 RPM	45s @ 3000 RPM
5	100	15s @ 500 RPM	45s @ 1000 RPM

Soft bake

Soft bake was performed by placing the substrate on a hot plate (HP131534, Thermo Scientific), preheated to 65 °C and then heated at a rate of 10 °C/min to a temperature of 95 °C. The substrate was left to bake at this temperature for 30 min. (35-40 μm layers) or 60 min (100 μm layers) depending on deposited film thickness. Then, the hot plate temperature was decreased at a rate of 10 °C/min until room temperature was reached.

Exposure

A SF-100 Intelligent Microsystems mask-less exposure machine was used to expose the desired pattern. It was configured to use a wavelength of 365 nm. Exposure lens, time and offset per layer are described in Table V.

Table V: Layer exposure parameters for the mask-less exposure machine.

Layer	Lens	Time [s]	Offset [mm]
1	4x	7.1	+0.043
2	20x	0.71	-0.001
3	20x	0.8	-0.001
4	4x	7.1	+0.043
5	4x	7.1	+0.043

Post exposure bake

In a similar way to the soft bake, the post exposure bake was performed by placing the substrate on a hot plate, preheated to 65 °C, temperature that was increased to 95 °C at a rate of 10 °C/min. The substrate was held at this temperature for 5 min. (35-40 µm layers) or 10 min (100 µm layers) depending on deposited film thickness. Afterwards, the substrate was cooled at a rate of 10 °C until room temperature was reached.

Development

The substrate was immersed in a crystallizer with enough developer (Microposit SU8 Developer) to completely cover its surface. It was subsequently subjected to moderate agitation by hand for 3-8 minutes depending on layer thickness. After this, the substrate was taken out of the developer solution and rinsed with IPA followed by a rinse with fresh developer solution. Afterwards, the substrate was rinsed again with IPA and dried using nitrogen (99.9999% pure).

Hard bake

Finally, the substrate was gradually heated on a hot plate at a rate of 10 °C/min to a temperature of 190 °C which was held constant for one hour. Then, the temperature was decreased at the same rate until it reached room temperature. This process was only done after layer 3 and layer 5 deposition.

○ **Pyrolysis**

The pyrolysis process was performed in a quartz tube placed inside a tube furnace with an inert atmosphere. This atmosphere was either a forming gas made of 95 % nitrogen (99.9999% pure) and 5% hydrogen (99.99% pure), or a 4 mTorr vacuum. The equipment used for each atmosphere was a GSL-1100X-UL-LD (MTI Corporation) tube furnace and a OTF-1200X-80-SL (MTI Corporation) tube furnace, respectively.

First, the chamber was evacuated with the chosen atmosphere for 20 minutes before turning on the furnace. After this, the furnace was heated following specific heating profiles for each atmosphere. The target temperatures, heating rates, times and gas flow rates for a forming gas atmosphere are described in Table VI. The heating profile under a vacuum atmosphere is shown in Fig. 58. Finally, after the heating profile was completed the furnace was turned off and the substrate was left inside to cool down naturally to ambient temperature before extracting it.

Table VI: Heating profile and gas flows for the pyrolysis process under a forming gas atmosphere.

Temperature [°C]	Time [min]	Heating Rate [°C/min]	Nitrogen [sccm]	Hydrogen [sccm]
0->180	18	+10	1000	0
180->180	15	0	1000	0
180->200	2	+10	1000	0
200->200	30	0	1000	0
200->230	3	+10	1000	0
230->230	15	0	1000	0
230->260	3	+10	1000	0
260->260	15	0	1000	0
260->300	4	+10	1000	0
300->300	15	0	1000	0
300->900	60	+10	1000	0
900->900	60	0	1000	19.5
900->200	70	-10	236	0
200->0	40	-5	236	0

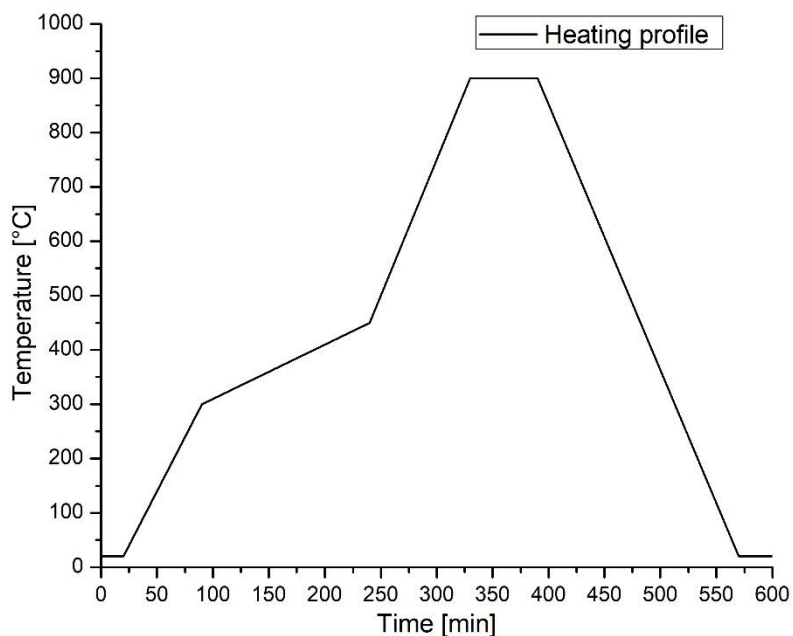


Fig. 58: Heating profile for the vacuum pyrolysis process.

○ **Electronics interface board**

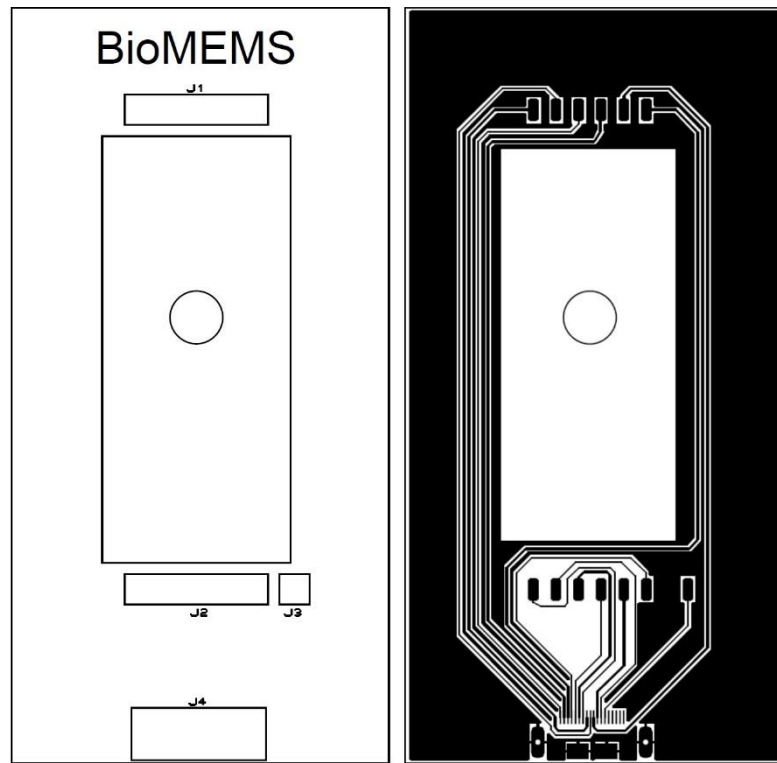


Fig. 59: (Left) Silk and (right) top copper layers of the electronics interface PCB. Actual size. Part ST60-18P was used for connector J4.

▪ **APPENDIX D: MICROFLUIDICS MODULE DESIGNS AND FABRICATION PROTOCOLS**

○ **Design schematics**

PDMS chip

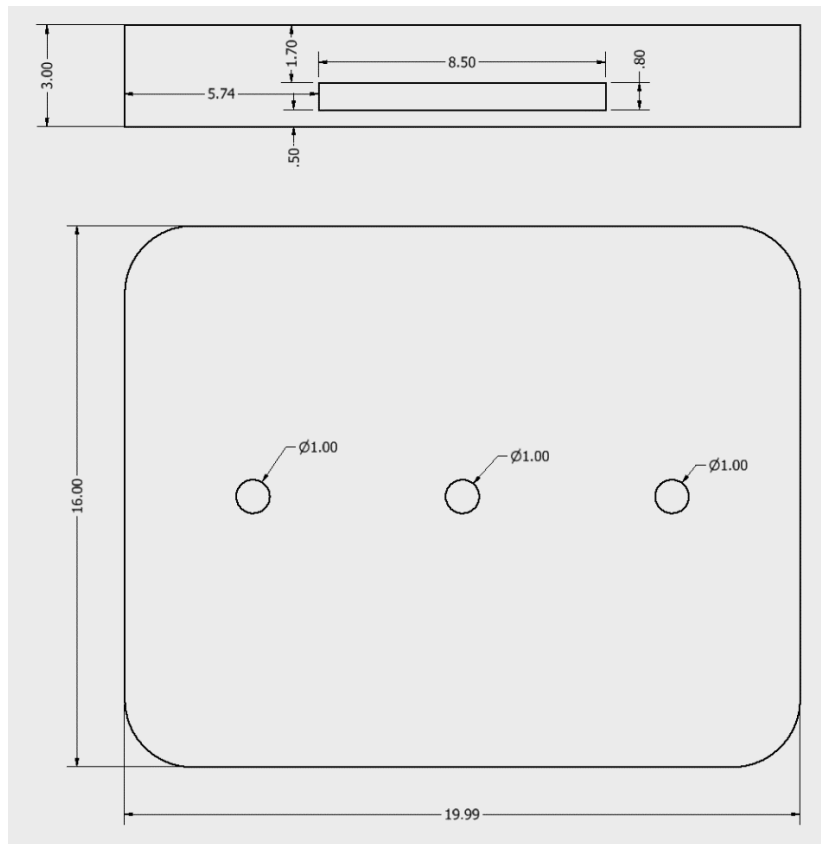


Fig. 60:PDMS chip schematics [mm].

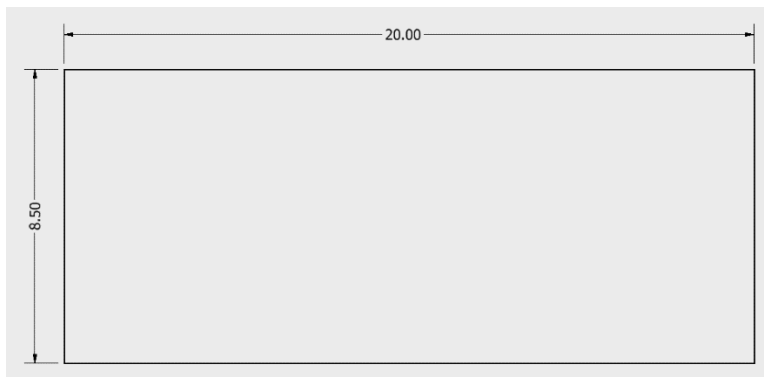


Fig. 61: ITO-covered glass slide dimensions [mm]. Thickness = 0.8 mm.

PDMS chip mold

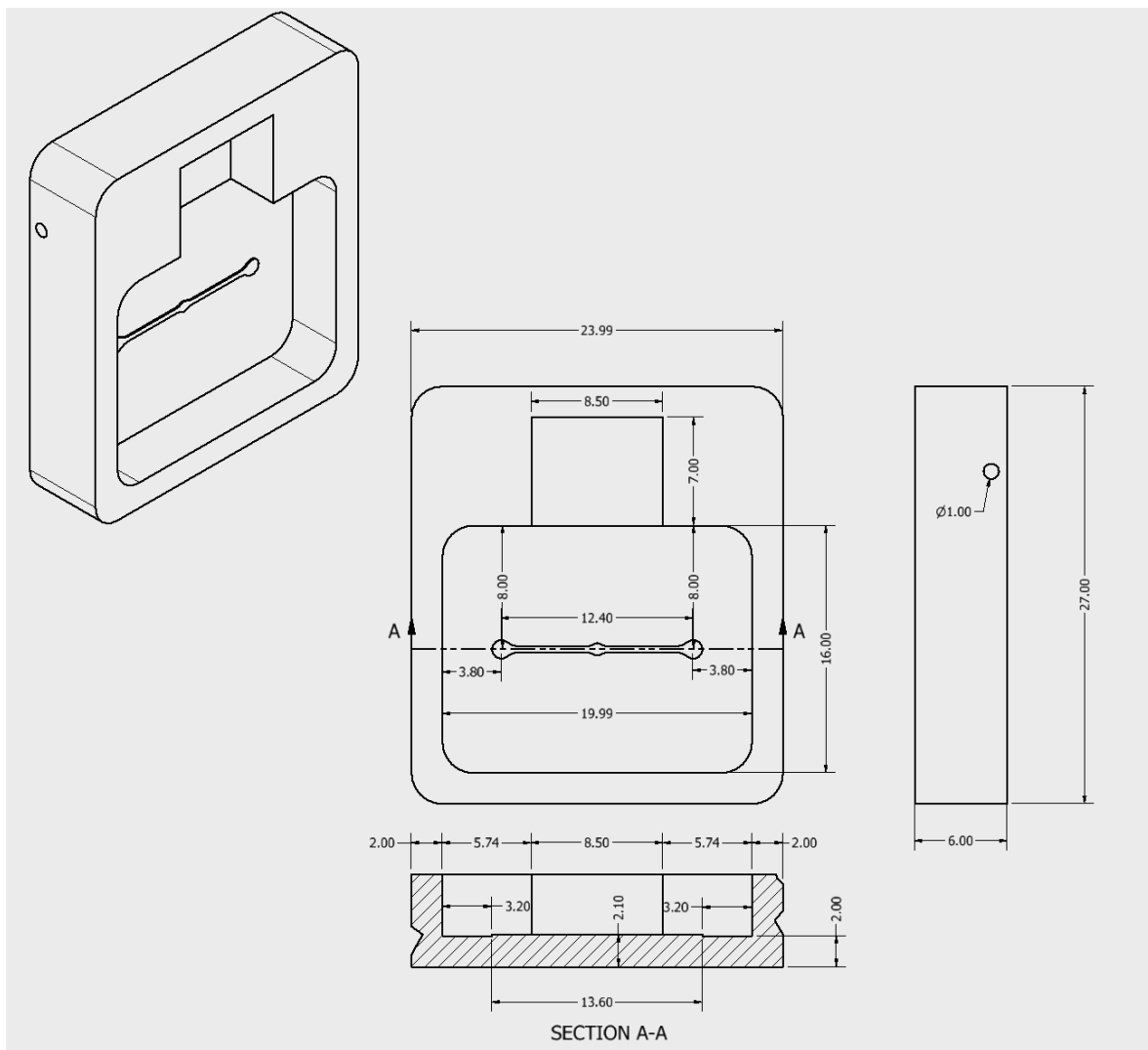


Fig. 62: PDMS chip mold schematics [mm].

○ **Soft lithography**

Soft lithography is the process of transferring a pattern to a soft polymer from a design mold, hence the name.

First, a mold of the desired microfluidic device was 3D printed (Ultimaker 2+) using PLA filament. Then, a glass slide coated with ITO was fixed in a recess built in the mold to hold it for PDMS molding. Afterwards, a batch of PDMS (Sylgard 184) was prepared with a 10 to 1 ratio polymer to polymerizing agent and mixed thoroughly for one minute. PDMS was then degasified in a vacuum chamber for 1 hour.

Following degasification, the PDMS was poured in the mold and further degasified in vacuum to eliminate trapped bubbles. This process lasted for 2 hours approximately. Then, the mold with PDMS was heated in a convection oven at 50 °C for 2 hours to end the polymerization process.

At this point, the microfluidic chip was demolded. Holes of 1 mm of diameter were punched at the location where the inlet, outlet and microelectrode zone ports of the microfluidic channel were placed. Finally, stainless-steel tube connectors with appropriate tubing were fitted in them.

○ Support structure deign schematics

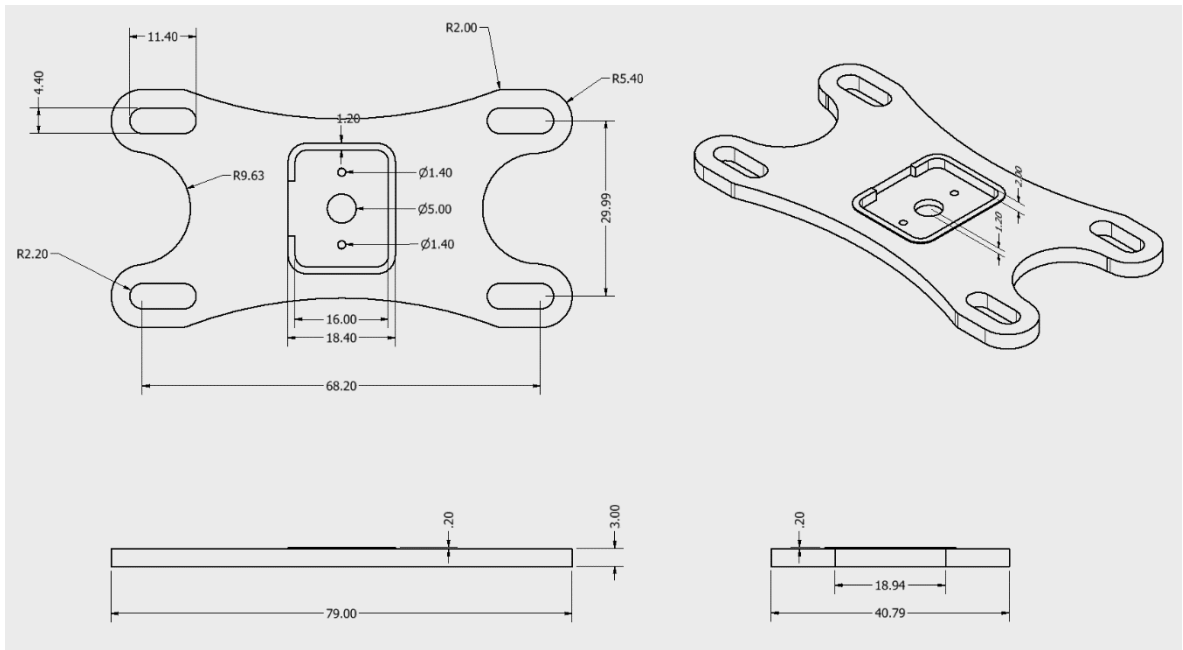


Fig. 63: Microfluidic module support structure top part [mm].

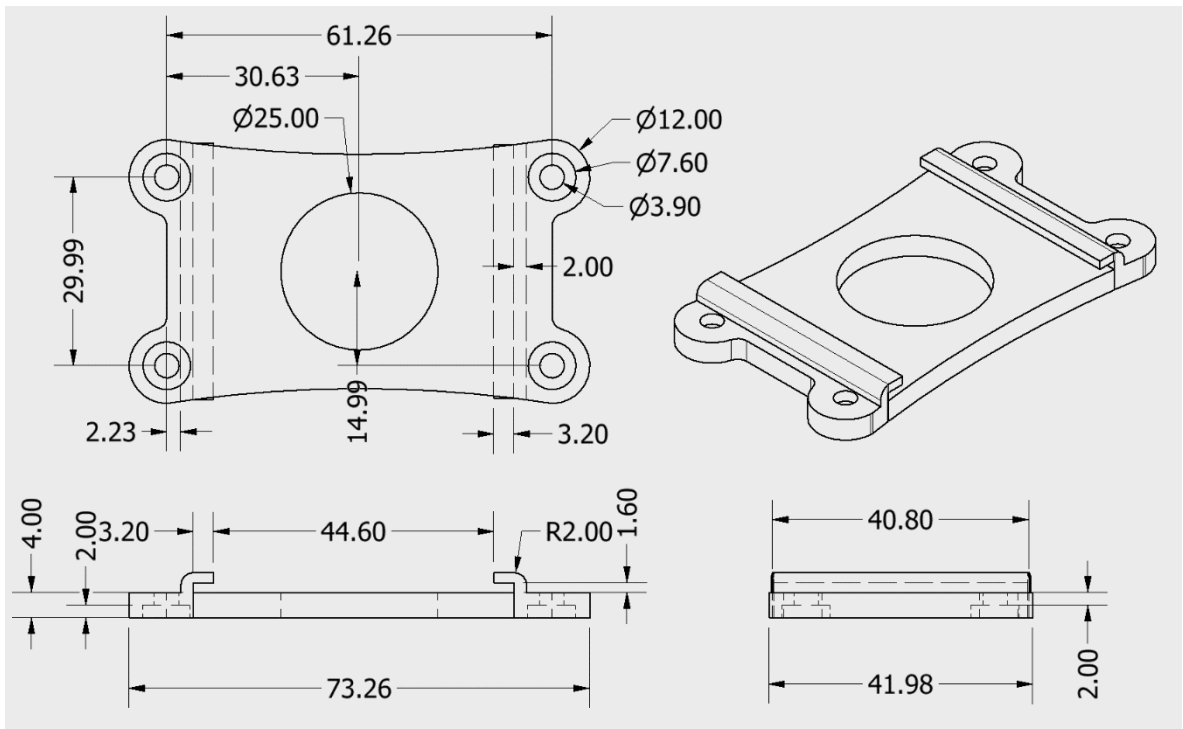


Fig. 64: Microfluidic module support structure bottom part [mm].

APPENDIX E: CONTROL ELECTRONICS MODULE DESIGNS AND SOFTWARE

Electrical schematics

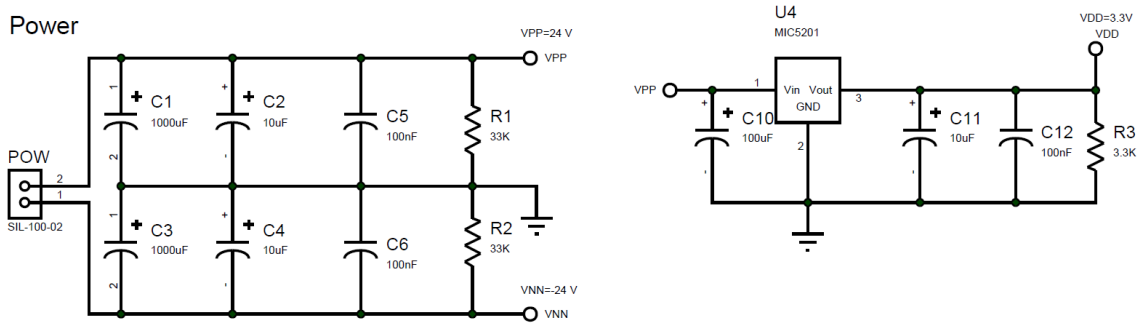


Fig. 65: Power regulation and voltage rails.

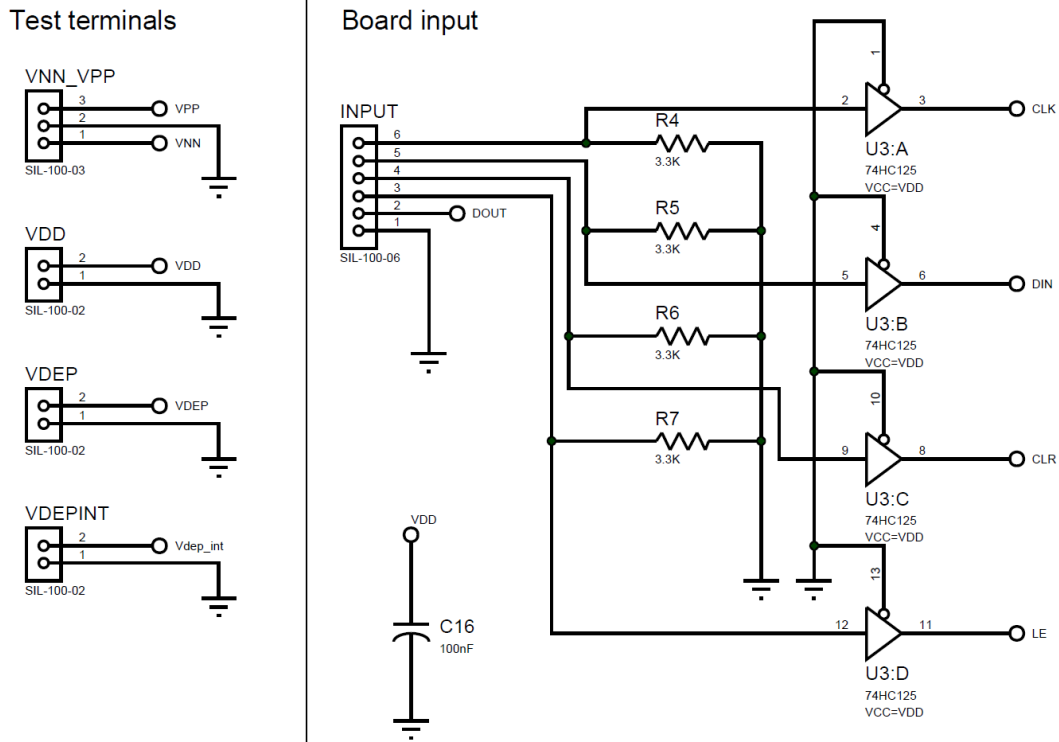


Fig. 66: Voltage test terminals (left) and protection stage for the microcontroller input signals (right).

Analog switch array

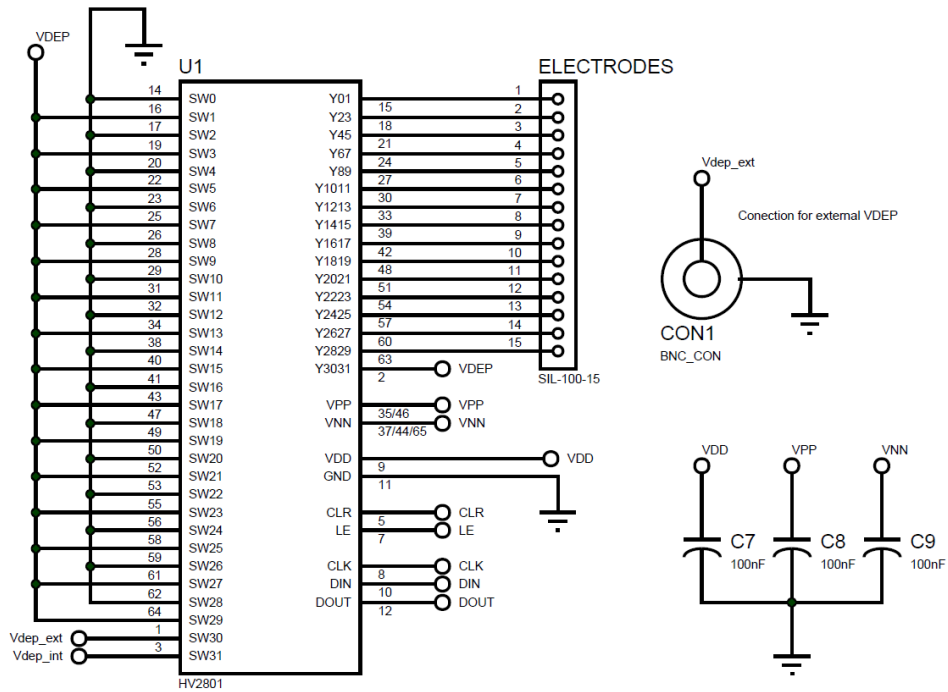


Fig. 67: Analog switch array and terminal for external DEP signals.

Internal VDEP generator

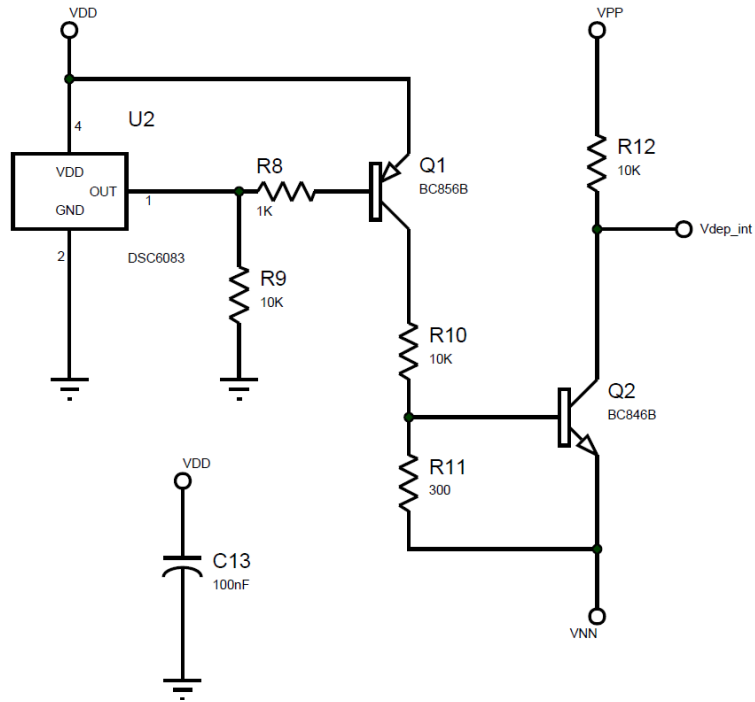


Fig. 68: Internal VDEP signal generator.

- PCB schematics

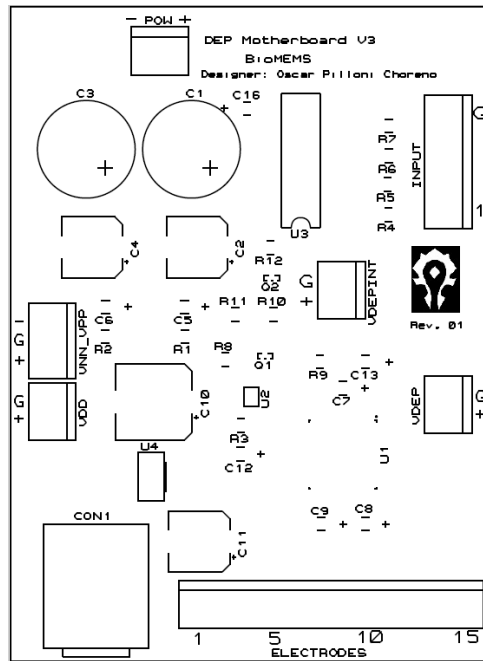


Fig. 69: Top layer silk labels. Actual size.

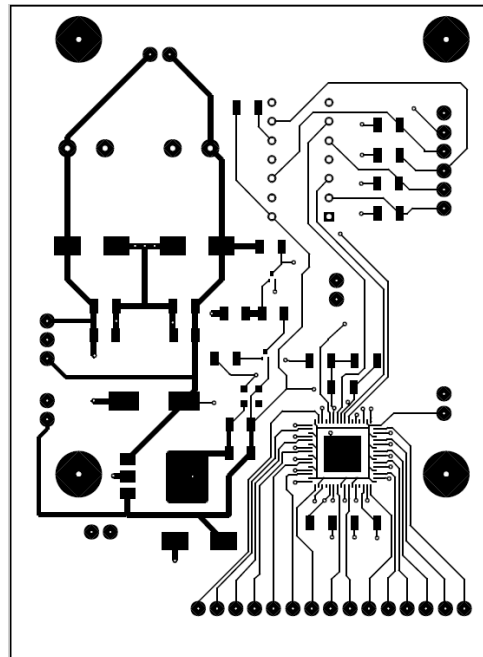


Fig. 70: Top layer PCB design. Actual size.

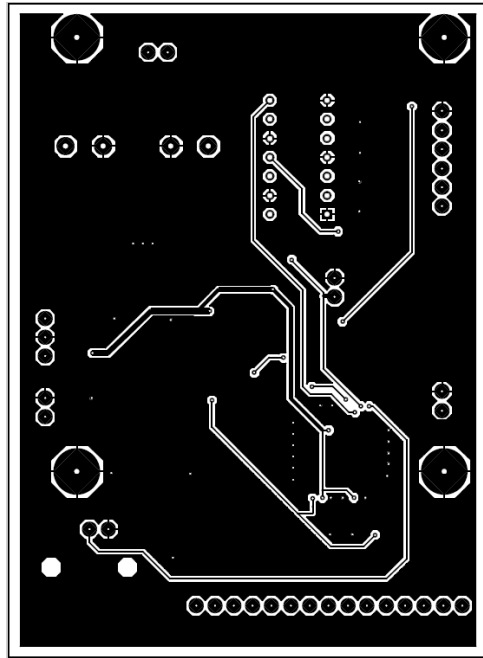


Fig. 71: Bottom layer PCB design. Actual size.

○ **Bill of materials**

Category	Quantity	References	Value	Stock Code
Capacitors	2	C1,C3	1000uF	NRWS102M50V125X25F
Capacitors	3	C2,C4,C11	10uF	EEE-FK1H100P
Capacitors	8	C5-C9,C12-C13,C16	100nF	T491A104K050AT
Capacitors	1	C10	100uF	NAZT101M50V8X10.5NBF
Resistors	2	R1-R2	33K	Digikey 311-3.3KETR-ND
Resistors	5	R3-R7	3.3K	RC1206FR-073K3L
Resistors	1	R8	1K	CRCW12061K00FKTA
Resistors	1	R9	10K	RCG120610K0FKEA
Resistors	1	R10	10K	RC1206FR-073K3L
Resistors	1	R11	300	RC1206FR-073K3L
Resistors	1	R12	10K	CRCW12061K00FKTA
Integrated Circuits	1	U1	HV2801	HV2801K6-G
Integrated Circuits	1	U2	DSC6083	DSC6083
Integrated Circuits	1	U3	74HC125	SN74HC125DR
Integrated Circuits	1	U4	MIC5201	MIC5201-3.3YS-TR
Transistors	1	Q1	BC856B	BC856BM3T5G
Transistors	1	Q2	BC846B	BC846BM3T5G
Miscellaneous	1	CON1	BNC_CON SIL-100-	bnc 0731000167
Miscellaneous	1	ELECTRODES	15 SIL-100-	22272151
Miscellaneous	1	INPUT	06 SIL-100-	SIL-100-06
Miscellaneous	1	POW	02 SIL-100-	SIL-100-02
Miscellaneous	3	VDD,VDEP,VDEPINT	02 SIL-100-	5-146277-2
Miscellaneous	1	VNN_VPP	03 SIL-100-	5-146277-3

○ **Support structure design schematics**

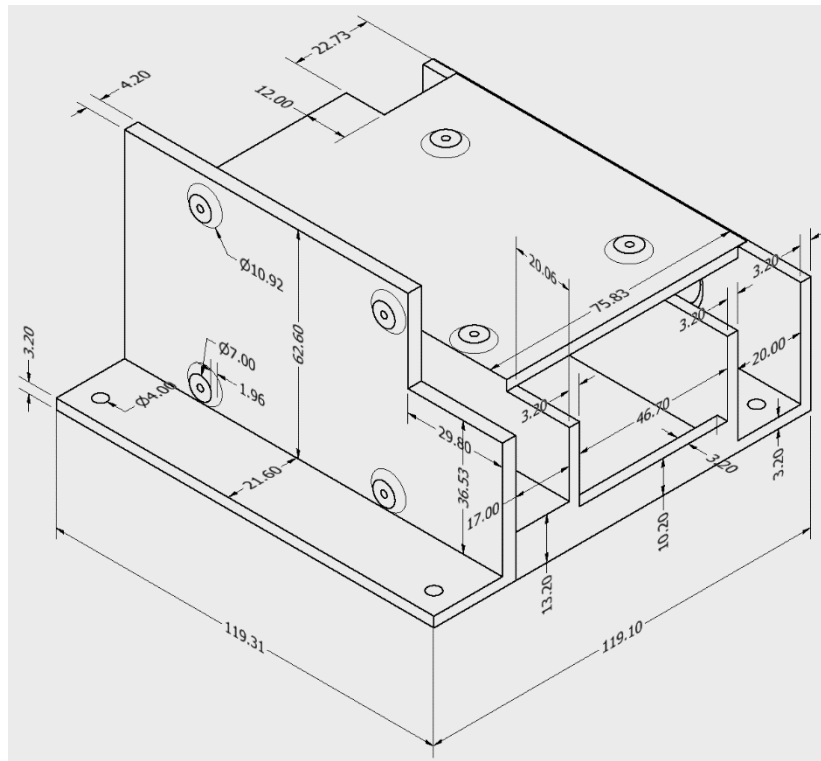


Fig. 72: Support structure for the electronics control module. Isometric front view [mm].

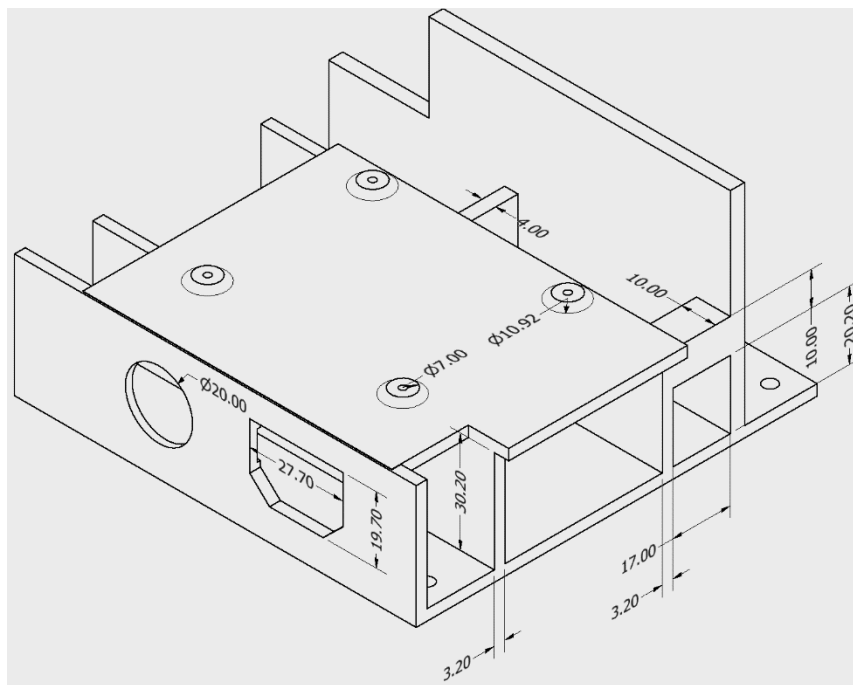


Fig. 73: Support structure for the electronics control module. Isometric back view [mm].

■ APPENDIX F: CONTROL ELECTRONICS MODULE

SOFTWARE

○ Raspberry PI firmware

The Raspberry Pi was loaded with NOOBS V2.4.4 as the operating system (OS) using the automated MATLAB R2017b configuration tool. This automatically generates an OS that can respond to remote commands sent through a secure network link. Setup of the OS was done following the information found in MATLAB repository for Raspberry PI (<https://www.mathworks.com/hardware-support/raspberry-pi-matlab.html>).

○ Computer interface software

The interface software was designed using MATLAB R2017b

Design window

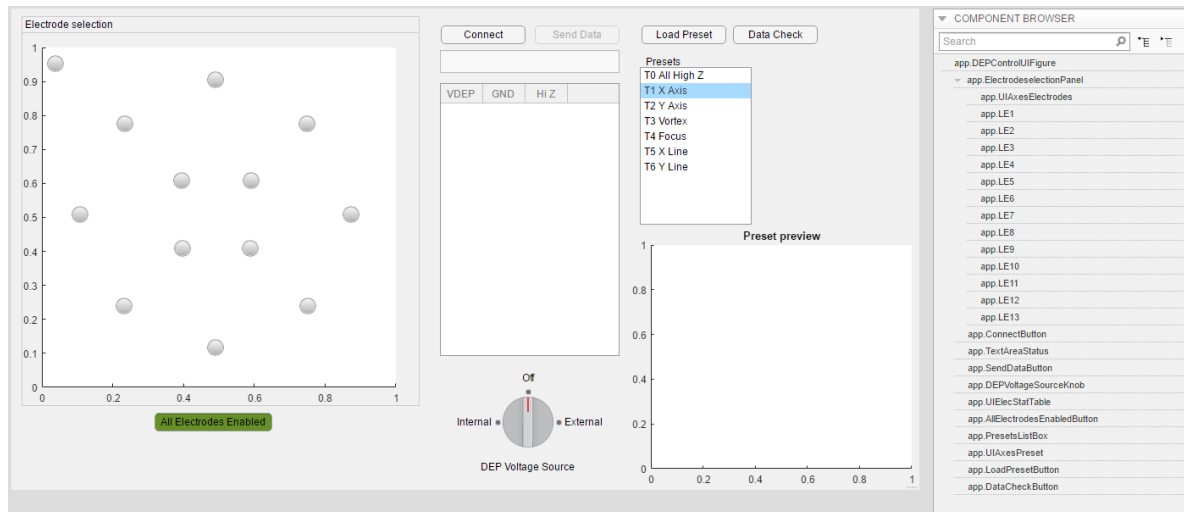


Fig. 74: (Left) Design components and (right) handler names of each element of the software window.

Code

```
classdef DEP_Con_V2 < matlab.apps.AppBase
% Properties that correspond to app components
properties (Access = public)
    DEPControlUIFigure          matlab.ui.Figure
    ElectrodeselectionPanel    matlab.ui.container.Panel
    UIAxesElectrodes           matlab.ui.control.UIAxes
    LE1                         matlab.ui.control.Lamp
    LE2                         matlab.ui.control.Lamp
    LE3                         matlab.ui.control.Lamp
    LE4                         matlab.ui.control.Lamp
    LE5                         matlab.ui.control.Lamp
    LE6                         matlab.ui.control.Lamp
    LE7                         matlab.ui.control.Lamp
    LE8                         matlab.ui.control.Lamp
    LE9                         matlab.ui.control.Lamp
    LE10                       matlab.ui.control.Lamp
    LE11                       matlab.ui.control.Lamp
    LE12                       matlab.ui.control.Lamp
    LE13                       matlab.ui.control.Lamp
    ConnectButton              matlab.ui.control.Button
    Label                      matlab.ui.control.Label
    TextAreaStatus             matlab.ui.control.TextArea
    SendDataButton             matlab.ui.control.Button
    DEPVoltageSourceKnobLabel  matlab.ui.control.Label
    DEPVoltageSourceKnob      matlab.ui.control.DiscreteKnob
    UIElecStatTable           matlab.ui.control.Table
    AllElectrodesEnabledButton matlab.ui.control.StateButton
    PresetsListBoxLabel       matlab.ui.control.Label
    PresetsListBox             matlab.ui.control.ListBox
    UIAxesPreset               matlab.ui.control.UIAxes
    LoadPresetButton          matlab.ui.control.Button
    DataCheckButton           matlab.ui.control.Button
end
properties (Access = private)
    statusText = '';          % Status handle
    sLine = 1;                % Status line handle
    hordepi = raspi;          % Interface to Raspberry pi %hordepi IP
    = 192.168.1.117
    DEPboard;                 % SPI connection handle
    statSPI = 0;              % SPI interface status 0=Disabled;
    1=Enabled
    D = zeros(1,32);          % Switches data handle
    DW = zeros(1,4);          % Data word handle
    % Number of electrodes (13 default, 15 max)
    % E15 hard coded to GND, Using E14 for E12 com (bad E12 on control
board)
    nElec = 13;
```

```

    pinCLR = 23;           % Control pin for HV2801 CLR
    pinLE = 24;           % Control pin for HV2801 nLE
    pinDOUT = 5;          % Control pin for HV2801 Dout

end
methods (Access = private)

    % Updates the status textArea
    function updateStatus(app, textString)
        app.statusText{app.sLine} = sprintf('%s', textString);
%Adds line to handler
        app.TextAreaStatus.Value = app.statusText{app.sLine};
%Updates textArea
        app.sLine=app.sLine+1;
%Advances line index
    end

    % binString formats binary a1-a8 elements into a string
    representation
    function [decCon] = binString(app,a8,a7,a6,a5,a4,a3,a2,a1)
        a(1)=a1;
        a(2)=a2;
        a(3)=a3;
        a(4)=a4;
        a(5)=a5;
        a(6)=a6;
        a(7)=a7;
        a(8)=a8;
        decCon = 0;
        for n=1:1:8
            decCon=decCon+a(n)*2^(n-1);
        end
    end

end

% updatedD updates lamp indicators and control variable D values
function updatedD(app,row,col)
    switch col
        case 1
            % Case VDEP
            eval(sprintf('app.LE%d.Color = [0.9 0.2 0.1]',row));
            if row==12
                row=14;
            end
            app.D((2*row)-1) = 0;
            app.D(2*row) = 1;
        case 2
            % Case GND
            eval(sprintf('app.LE%d.Color = [0 0.45 0.74]',row));
            if row==12
                row=14;
            end
        end
    end
end

```

```

        end
        app.D((2*row)-1) = 1;
        app.D(2*row) = 0;
    case 3
        % Case High Z
        eval(sprintf('app.LE%d.Color = [0.8 0.8 0.8]',row));
        if row==12
            row=14;
        end
        app.D((2*row)-1) = 0;
        app.D(2*row) = 0;
    end
end

% Update DW updates te dataset to be sent
function UpdateDW(app,statString)
    app.DW(1) =
binString(app,app.D(8),app.D(7),app.D(6),app.D(5),app.D(4),app.D(3),app.D(2)
,app.D(1));
    app.DW(2) =
binString(app,app.D(16),app.D(15),app.D(14),app.D(13),app.D(12),app.D(11),ap
p.D(10),app.D(9));
    app.DW(3) =
binString(app,app.D(24),app.D(23),app.D(22),app.D(21),app.D(20),app.D(19),ap
p.D(18),app.D(17));
    app.DW(4) =
binString(app,app.D(32),app.D(31),app.D(30),app.D(29),app.D(28),app.D(27),ap
p.D(26),app.D(25));
    updateStatus(app, [statString,string(app.DW(1)), '
',string(app.DW(2)), ' ',string(app.DW(3)), ' ',string(app.DW(4))])
end

end
methods (Access = private)
% Code that executes after component creation
function startupFcn(app)
    % Load HUD image
    ElecHUD =
imread('D:\Archivo\UNAM\Doctorado\Electronica\Software\Matlab\Assets\Elec.jp
g');
        image(app.UIAxesElectrodes,ElecHUD);
        axis(app.UIAxesElectrodes,'off');
        axis(app.UIAxesElectrodes,'image');

    % Load preset image
    PresetHUD =
imread('D:\Archivo\UNAM\Doctorado\Electronica\Software\Matlab\Assets\T1 X
Axis.jpg');
        image(app.UIAxesPreset,PresetHUD);
        axis(app.UIAxesPreset,'off');

```

```

axis(app.UIAxesPreset, 'image');

% Display connection status
updateStatus(app, ['Connected to:' app.hordepi.DeviceAddress]);

% Populate electrode status table
for a=1:1:app.nElec
    tempStr1(a,:)={sprintf('E%d',a)};
    tempStr(a,:)={false,false,true};
end
app.UIElecStatTable.RowName = tempStr1;
app.UIElecStatTable.Data = tempStr;

% Setup GPIO pins

configurePin(app.hordepi,app.pinCLR, 'DigitalOutput');           % CLR Pin
                        configurePin(app.hordepi,app.pinLE, 'DigitalOutput');
% nLE Pin

configurePin(app.hordepi,app.pinDOUT, 'DigitalInput');
                        writeDigitalPin(app.hordepi,app.pinCLR,0);
% Initialize as CLR enabled000
                        writeDigitalPin(app.hordepi,app.pinLE,1);
% Initialize as LE disabled
                        app.AllElectrodesEnabledButton.Value = 1;
% Initialize wuit disabled electrodes
end
% Value changed function: AllElectrodesEnabledButton
function AllElectrodesEnabledButtonValueChanged(app, event)
    value = app.AllElectrodesEnabledButton.Value;
    switch value
        case 1
            app.AllElectrodesEnabledButton.Text = 'All Electrodes
Enabled';
            app.AllElectrodesEnabledButton.BackgroundColor =
[0.47,0.67,0.19];
            writeDigitalPin(app.hordepi,app.pinCLR,0);
        case 0
            app.AllElectrodesEnabledButton.Text = 'All Electrodes
Disabled';
            app.AllElectrodesEnabledButton.BackgroundColor =
[0.9,0.4,0.1];
            writeDigitalPin(app.hordepi,app.pinCLR,1);
        end
    end
end
% Button pushed function: ConnectButton
function ConnectButtonPushed(app, event)
    if (app.statSPI == 0)
        app.ConnectButton.Enable = 'off';
        updateStatus(app, 'Enabling SPI...');

```

```

        enableSPI(app.hordepi); %Enables SPI
communication
        app.statSPI = 1; %Flag SPI status
        updateStatus(app, 'SPI Enabled');
        updateStatus(app, 'Connecting lines...');
        app.DEFboard = spidev(app.hordepi, 'CE0'); %Create
connection to DEP board
        updateStatus(app, 'Board connected')
        app.SendDataButton.Enable = 'on';
        app.ConnectButton.Text = 'Release';
        app.ConnectButton.Enable = 'on';
    else
        app.ConnectButton.Enable = 'off';
        updateStatus(app, 'Ending connection...')
        disableSPI(app.hordepi); %Disable SPI
communication
        app.statSPI = 0; %Flag SPI status
        updateStatus(app, 'Connection terminated')
        app.SendDataButton.Enable = 'off';
        app.ConnectButton.Text = 'Connect';
        app.ConnectButton.Enable = 'on';
    end
end
% Close request function: DEPControlUIFigure
function DEPControlUIFigureCloseRequest(app, event)
    if (app.statSPI==1)
        disableSPI(app.hordepi);
% End SPI connection
    end
    writeDigitalPin(app.hordepi, app.pinCLR, 1);
% Finalize as CLR disabled
    writeDigitalPin(app.hordepi, app.pinLE, 1);
% Finalize as LE disabled
    delete(app);
end
% Value changed function: DEPVoltageSourceKnob
function DEPVoltageSourceKnobValueChanged(app, event)
    value = app.DEPVoltageSourceKnob.Value;
    switch value
        case 'External'
            app.D(31) = 1;
            app.D(32) = 0;
        case 'Off'
            app.D(31) = 0;
            app.D(32) = 0;
        case 'Internal'
            app.D(31) = 0;
            app.D(32) = 1;
    end
end
end

```

```

% Button pushed function: DataCheckButton
function DataCheckButtonPushed(app, event)
    UpdateDW(app, 'DW:');
end
% Button pushed function: LoadPresetButton
function LoadPresetPushed(app, event)
    % Load preset data file
    [presets,~,raw] =
xlsread('D:\Archivo\UNAM\Doctorado\Electronica\Software\Matlab\Assets\presets.xlsx');
    [row_size,col_size] = size(raw);
    % Get preset list value
    value = app.PresetsListBox.Value;
    %Select appropriate state of each electrode
    for a=1:(col_size-1)
        if (strcmp(cell2mat(raw(1,a+1)),value))
            for b=1:(row_size-1)
                switch(presets(b,a))
                    case 2
                        % Case VDEP
                        app.UIElecStatTable.Data(b,1) = {true};
                        app.UIElecStatTable.Data(b,2) = {false};
                        app.UIElecStatTable.Data(b,3) = {false};
                        updatedD(app,b,1);

                    case 1
                        % Case GND
                        app.UIElecStatTable.Data(b,1) = {false};
                        app.UIElecStatTable.Data(b,2) = {true};
                        app.UIElecStatTable.Data(b,3) = {false};
                        updatedD(app,b,2);

                    case 0
                        % Case High Z
                        app.UIElecStatTable.Data(b,1) = {false};
                        app.UIElecStatTable.Data(b,2) = {false};
                        app.UIElecStatTable.Data(b,3) = {true};
                        updatedD(app,b,3);
                end
            end
        end
    end
end
% Value changed function: PresetsListBox
function Presets(app, event)
    value = app.PresetsListBox.Value;

    % Change preset preview

```

```

        PresetHUD =
imread(['D:\Archivo\UNAM\Doctorado\Electronica\Software\Matlab\Assets\'
value '.jpg']);
        image(app.UIAxesPreset,PresetHUD);
        axis(app.UIAxesPreset,'off');
        axis(app.UIAxesPreset,'image');

    end
    % Button pushed function: SendDataButton
    function SendDataButtonPushed(app, event)
        % Format data to be sent
        UpdateDW(app,'Sending:');
        % Send data
        writeDigitalPin(app.hordepi,app.pinLE,0);
% Enable LE

writeRead(app.DEPboard,[app.DW(4),app.DW(3),app.DW(2),app.DW(1)]); %
Send data
        writeDigitalPin(app.hordepi,app.pinLE,1);
% Disable LE
    end
    % Cell edit callback: UIElecStatTable
    function UIElecStatTableCellEdit(app, event)
        % Check for only one selection per electrode
        row = event.Indices(1,1);
        col = event.Indices(1,2);
        for a=1:1:3
            if a~=col
                app.UIElecStatTable.Data(row,a) = {false};
            end
        end
        % Update data handle and lamp indicators
        updateD(app,row,col);

    end
end
% App initialization and construction
methods (Access = private)
    % Create UIFigure and components
    function createComponents(app)
        % Create DEPControlUIFigure
        app.DEPControlUIFigure = uifigure;
        app.DEPControlUIFigure.Position = [100 100 1072 568];
        app.DEPControlUIFigure.Name = 'DEP Control';
        app.DEPControlUIFigure.CloseRequestFcn = createCallbackFcn(app,
@DEPControlUIFigureCloseRequest, true);
        % Create ElectrodeselectionPanel
        app.ElectrodeselectionPanel = uipanel(app.DEPControlUIFigure);
        app.ElectrodeselectionPanel.Title = 'Electrode selection';
        app.ElectrodeselectionPanel.Position = [13 100 470 460];
    end
end

```

```

% Create UIAxesElectrodes
app.UIAxesElectrodes = uiaxes(app.ElectrodeselectionPanel);
app.UIAxesElectrodes.GridAlpha = 0.15;
app.UIAxesElectrodes.MinorGridAlpha = 0.25;
app.UIAxesElectrodes.Position = [1 1 450 430];
% Create LE1
app.LE1 = uilamp(app.ElectrodeselectionPanel);
app.LE1.Position = [112 323 20 20];
app.LE1.Color = [0.8 0.8 0.8];
% Create LE2
app.LE2 = uilamp(app.ElectrodeselectionPanel);
app.LE2.Position = [219 375 20 20];
app.LE2.Color = [0.8 0.8 0.8];
% Create LE3
app.LE3 = uilamp(app.ElectrodeselectionPanel);
app.LE3.Position = [327 323 20 20];
app.LE3.Color = [0.8 0.8 0.8];
% Create LE4
app.LE4 = uilamp(app.ElectrodeselectionPanel);
app.LE4.Position = [379 216 20 20];
app.LE4.Color = [0.8 0.8 0.8];
% Create LE5
app.LE5 = uilamp(app.ElectrodeselectionPanel);
app.LE5.Position = [328 108 20 20];
app.LE5.Color = [0.8 0.8 0.8];
% Create LE6
app.LE6 = uilamp(app.ElectrodeselectionPanel);
app.LE6.Position = [219 59 20 20];
app.LE6.Color = [0.8 0.8 0.8];
% Create LE7
app.LE7 = uilamp(app.ElectrodeselectionPanel);
app.LE7.Position = [111 108 20 20];
app.LE7.Color = [0.8 0.8 0.8];
% Create LE8
app.LE8 = uilamp(app.ElectrodeselectionPanel);
app.LE8.Position = [59 216 20 20];
app.LE8.Color = [0.8 0.8 0.8];
% Create LE9
app.LE9 = uilamp(app.ElectrodeselectionPanel);
app.LE9.Position = [179 256 20 20];
app.LE9.Color = [0.8 0.8 0.8];
% Create LE10
app.LE10 = uilamp(app.ElectrodeselectionPanel);
app.LE10.Position = [261 256 20 20];
app.LE10.Color = [0.8 0.8 0.8];
% Create LE11
app.LE11 = uilamp(app.ElectrodeselectionPanel);
app.LE11.Position = [260 176 20 20];
app.LE11.Color = [0.8 0.8 0.8];
% Create LE12

```

```

app.LE12 = uilamp(app.ElectrodeselectionPanel);
app.LE12.Position = [180 176 20 20];
app.LE12.Color = [0.8 0.8 0.8];
% Create LE13
app.LE13 = uilamp(app.ElectrodeselectionPanel);
app.LE13.Position = [30 394 20 20];
app.LE13.Color = [0.8 0.8 0.8];
% Create ConnectButton
app.ConnectButton = uibutton(app.DEPControlUIFigure, 'push');
app.ConnectButton.ButtonPushedFcn = createCallbackFcn(app,
@ConnectButtonPushed, true);
app.ConnectButton.Position = [508 527 100 22];
app.ConnectButton.Text = 'Connect';
% Create Label
app.Label = uilabel(app.DEPControlUIFigure);
app.Label.HorizontalAlignment = 'right';
app.Label.Position = [507 503 25 15];
app.Label.Text = '';
% Create TextAreaStatus
app.TextAreaStatus = uitextarea(app.DEPControlUIFigure);
app.TextAreaStatus.Editable = 'off';
app.TextAreaStatus.Position = [507 493 212 27];
% Create SendDataButton
app.SendDataButton = uibutton(app.DEPControlUIFigure, 'push');
app.SendDataButton.ButtonPushedFcn = createCallbackFcn(app,
@SendDataButtonPushed, true);
app.SendDataButton.Enable = 'off';
app.SendDataButton.Position = [619 527 100 22];
app.SendDataButton.Text = 'Send Data';
% Create DEPVoltageSourceKnobLabel
app.DEPVoltageSourceKnobLabel = uilabel(app.DEPControlUIFigure);
app.DEPVoltageSourceKnobLabel.HorizontalAlignment = 'center';
app.DEPVoltageSourceKnobLabel.Position = [552.5 21 117 15];
app.DEPVoltageSourceKnobLabel.Text = 'DEP Voltage Source';
% Create DEPVoltageSourceKnob
app.DEPVoltageSourceKnob = uiknob(app.DEPControlUIFigure,
'discrete');
app.DEPVoltageSourceKnob.Items = {'Internal', 'Off',
'External'};
app.DEPVoltageSourceKnob.ValueChangedFcn =
createCallbackFcn(app, @DEPVoltageSourceKnobValueChanged, true);
app.DEPVoltageSourceKnob.Position = [581 51 60 60];
% Create UIElecStatTable
app.UIElecStatTable = uitable(app.DEPControlUIFigure);
app.UIElecStatTable.ColumnName = {'VDEP'; 'GND'; 'Hi Z'};
app.UIElecStatTable.ColumnWidth = {50, 50, 50};
app.UIElecStatTable.RowName = {};
app.UIElecStatTable.ColumnEditable = true;
app.UIElecStatTable.CellEditCallback = createCallbackFcn(app,
@UIElecStatTableCellEdit, true);

```

```

        app.UIElecStatTable.Position = [507 159 212 322];
        % Create AllElectrodesEnabledButton
        app.AllElectrodesEnabledButton =
uibutton(app.DEPControlUIFigure, 'state');
        app.AllElectrodesEnabledButton.ValueChangedFcn =
createCallbackFcn(app, @AllElectrodesEnabledButtonValueChanged, true);
        app.AllElectrodesEnabledButton.Text = 'All Electrodes Enabled';
        app.AllElectrodesEnabledButton.BackgroundColor = [0.4706 0.6706
0.1882];
        app.AllElectrodesEnabledButton.Position = [169.5 70 139 22];
        app.AllElectrodesEnabledButton.Value = true;
        % Create PresetsListBoxLabel
        app.PresetsListBoxLabel = uilabel(app.DEPControlUIFigure);
        app.PresetsListBoxLabel.HorizontalAlignment = 'right';
        app.PresetsListBoxLabel.Position = [745 499 46 15];
        app.PresetsListBoxLabel.Text = 'Presets';
        % Create PresetsListBox
        app.PresetsListBox = uilistbox(app.DEPControlUIFigure);
        app.PresetsListBox.Items = {'T0 All High Z', 'T1 X Axis', 'T2 Y
Axis', 'T3 Vortex', 'T4 Focus', 'T5 X Line', 'T6 Y Line'};
        app.PresetsListBox.ValueChangedFcn = createCallbackFcn(app,
@Presets, true);
        app.PresetsListBox.Position = [743 314 132 186];
        app.PresetsListBox.Value = 'T1 X Axis';
        % Create UIAxesPreset
        app.UIAxesPreset = uiaxes(app.DEPControlUIFigure);
        title(app.UIAxesPreset, 'Preset preview')
        app.UIAxesPreset.GridAlpha = 0.15;
        app.UIAxesPreset.MinorGridAlpha = 0.25;
        app.UIAxesPreset.Position = [733 5 340 306];
        % Create LoadPresetButton
        app.LoadPresetButton = uibutton(app.DEPControlUIFigure, 'push');
        app.LoadPresetButton.ButtonPushedFcn = createCallbackFcn(app,
@LoadPresetPushed, true);
        app.LoadPresetButton.Position = [745 527 100 22];
        app.LoadPresetButton.Text = 'Load Preset';
        % Create DataCheckButton
        app.DataCheckButton = uibutton(app.DEPControlUIFigure, 'push');
        app.DataCheckButton.ButtonPushedFcn = createCallbackFcn(app,
@DataCheckButtonPushed, true);
        app.DataCheckButton.Position = [853 527 100 22];
        app.DataCheckButton.Text = 'Data Check';
    end
end
methods (Access = public)
    % Construct app
    function app = DEP_Con_V2
        % Create and configure components
        createComponents(app)
        % Register the app with App Designer

```

```
    registerApp(app, app.DEPControlUIFigure)
    % Execute the startup function
    runStartupFcn(app, @startupFcn)
    if nargin == 0
        clear app
    end
end
% Code that executes before app deletion
function delete(app)
    % Delete UIFigure when app is deleted
    delete(app.DEPControlUIFigure)
end
end
end
```

■ APPENDIX G: MATLAB PROGRAMS

○ Clausius-Mossotti factor and electric field strength

```
%% Constants definition
eps0=8.85418781e-12;          %[F/m] Vacuum electrical permittivity

%% Experimental parameters
%Applied electric potential
V=20;                        %[V] Electric potential
delec=50e-6;                  %[m] Microelectrode gap
f=linspace(1,10e9,5000);     %[Hz] Frequency range
magdelEsq=1e15;              %[V^2/m^3] Electric field strength

%%Media properties
epsm=80*eps0;                %[F/m] Electrical permittivity
sigmam=5e-6;                  %[S/m] Electrical conductivity
viscm=8.9e-4;                 %[Pa s] Dynamic viscosity
densm=1000;                   %[kg/m^3] Density

%%Particle properties
epsp=2.6*eps0;                %[F/m] Electrical permittivity
sigmap=6.7e-14;               %[S/m] Electrical conductivity
Rp=linspace(1e-6,50e-6,10000); %[m] Radius range

%%Multi shell model approximation
epsmem=(epsm+epsp)/2;         %[F/m]
sigmamem=(sigmam+sigmap)/2;  %[S/m]
dmem=Rp/10;

%% Clausius-Mossotti factor
for a=1:1:length(f)
    eps1(a)=epsm-li*(sigmam/(2*pi*f(a)));
    eps2(a)=epsp-li*(sigmap/(2*pi*f(a)));
    K(a)=(eps2(a)-eps1(a))/(eps2(a)+(2*eps1(a)));
end

%% Plots
figure (1)
semilogx(f,real(K))

%% Electric field from velocity
u = 10e-5;                    %[m/s] Particle velocity
for a=1:1:length(Rp)
    Efield(a) = abs(3*u*viscm/(real(max(K))*epsm*(Rp(a))^2));
end
figure (2)
semilogx(Rp,Efield)
```

○ Van der Pauw's numerical resistivity computation

```
%% Workspace cleaning
close all
clear all

%% Measured parameters
Rabcd = 4.96;
Rbcda = 4.96;

%% Numerical curve approximation
rho = 0:(1e-6):(1e-2);
t = 17e-6;
y1 = exp(-pi*t*Rabcd./rho);
y2 = 1 -exp(-pi*t*Rbcda./rho);

%% Plots
figure(1)
hold on
plot(rho,y1)
plot(rho,y2) %Intersection between curves determines resistivity
```

- **APPENDIX H: ARTICLE “MICRO DEVICE FOR BIO-PARTICLE POSITIONING IN A 3D SPACE BASED ON CARBON MEMS AND DIELECTROPHORETIC FORCES”**

Micro Device for Bio-Particle Positioning in a 3D space based on Carbon MEMS and Dielectrophoretic Forces

O. Pilloni^{a,d}, José Luis Benítez Benítez^b, Luis F. Olguín^c, Carlos A. Palacios-Morales^a and L. Oropeza-Ramos^a

^a Facultad de Ingeniería, Universidad Nacional Autónoma de México, UNAM, Ciudad de México, 04510, México

^b Centro de Ciencias Aplicadas y Desarrollo Tecnológico, Universidad Nacional Autónoma de México, UNAM

^c Facultad de Química, Universidad Nacional Autónoma de México, UNAM, Ciudad de México, 04510, México

^d Programa de Maestría y Doctorado en Ingeniería, Universidad Nacional Autónoma de México, Ciudad de México, 04510, México

The positioning of micron sized bio particles is of great interest to fields like medicine and biology. We introduce a device that would aid in the positioning of bio particles in a tridimensional space, using a combination of individually addressable planar and 3D carbon micro electrodes to exert a dielectrophoretic (DEP) force. Fabrication and test of the device were performed. Working principle of the motion of micron-sized particles using DEP is characterized by particle image velocimetry.

Introduction

Experiments on micron sized bio particles (bio compatible micro particles, cells) are limited by the manipulation techniques used to position particles in a zone of interest, like the focus point of an optical system, a micro electrode for an electrical measurement, a tridimensional cellular scaffold or a reaction chamber for a chemical process.

Dielectrophoresis (DEP) refers to a force exerted on a polarizable particle by the effect of its interaction with a non-uniform electric field (1). It has been proven that DEP is an effective method of particle sorting in microfluidic channels (2,3) and also it has been explored its use for quantitative cell characterization (4) and as a method for particle positioning in 2D planes (5).

We introduce a device that would aid in the precise positioning in 3D space of micron sized bio particles inside of a microfluidic channel. This would allow the use of the full size of the chamber in which the bio particles are confined, to obtain specialized arrays of such particles in a desired fashion.

This device uses a combination of individually addressable 3D electrodes and planar electrodes based on carbon micro electro mechanical systems (C-MEMS) to induce dielectrophoretic (DEP) forces (6,7). C-MEMS is an emerging field which enumerates advantages over traditional Si technologies such as excellent bio-compatibility, lower manufacturing costs and carbon precursors costs, wider electrochemical stability window and chemical inertness (8). All this encourages its adoption for biological applications.

Working principle and design

The proposed device uses a series of carbon-based 3D electrodes and a matrix of planar electrodes produced by the pyrolysis of a common photoresist (SU-8) (9).

By using the electrodes to exert a pulsed DEP force, coplanar to the substrate by the 3D electrodes and orthogonal to the substrate by the planar electrodes, it is possible to precisely position a bio particle in a confined microfluidic volume at low flow rates.

These types of electrodes are chosen because they can induce a DEP force by applying small electric potentials (~ 10 V) due to the fact that are immersed in the carrying fluid. Pulsed DEP was selected due to its low cost implementation and because it is able to affect bio particles positions while maintaining their viability (10).

The device is built by first depositing a layer of photoresist that is patterned in the shape of the micro electrode interconnections and the planar electrodes, a second layer is then deposited and patterned to obtain 3D micro electrodes. The device is then pyrolyzed, obtaining carbon structures from the photoresist patterned features, which are electrically conductive. A passivation layer made of SU 8 is then deposited on top of the device and is patterned in such a way that it only exposes the planar and 3D microelectrodes to the work fluid. This is depicted in Figure 1.

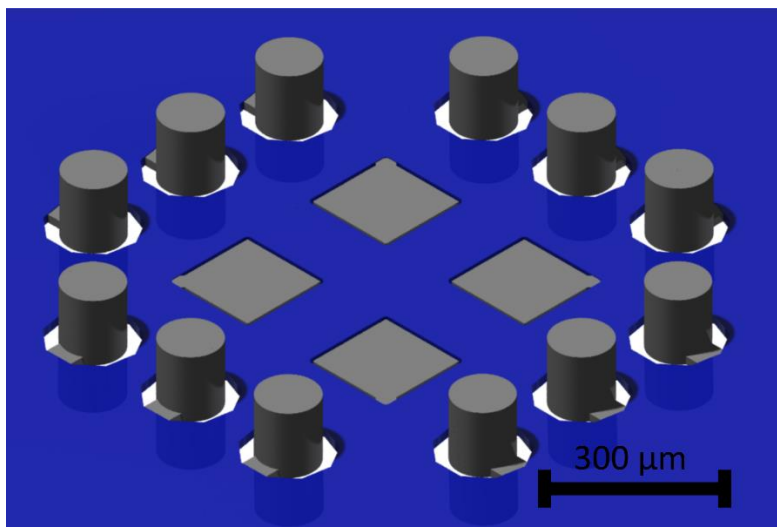


Figure 1. Computer assisted design of the micro electrode device with passivation layer

Fabrication

Photolithography process

A mask-less photolithography process was used to pattern the micro electrodes, consisting of a first thin layer for planar electrodes and interconnections, and a second thick layer for the 3D electrodes. For the first layer, SU8 3035 (Microchem) was deposited on a fused silica substrate (JGS2 grade, 500 μm thick, UniversityWafer Inc.) to form a 35 μm layer of resin.

The resin was soft baked by placing the substrate on a hot plate, preheated to 30 °C and then heated at a rate of 10 °C/min to a temperature of 105 °C, which was held constant for 20 min. Then, the hot plate temperature was decreased at the same rate until it reached room temperature and the substrate was left there to cool naturally. Subsequently, the resin was exposed using an IMP SF100 mask-less photolithography system (Intelligent Micro Patterning) to pattern the planar electrodes and their interconnections.

Then, the resin was post exposure baked following the same ramp profile as for the soft bake, but holding the 105 °C for only 5 minutes. The resin was then developed for 4 minutes using SU8 developer (Microchem) and a final hard bake was performed to enhance adhesion of the resin to the substrate for the pyrolysis process. This step was performed by gradually heating the substrate on a hot plate at a rate of 10 °C/min to a temperature of 190 °C which was held constant for one hour. Then, the temperature was decreased at the same rate until it reached room temperature.

This same process was used to pattern a second layer, 100 μm thick, made of SU8 50 (Microchem) which was used to form the 3D micro electrodes. The differences were that the soft and post exposure bake times were 40 and 12 min, respectively, and the hard bake step was omitted for this layer.

Pyrolysis

The pyrolysis of the resin was performed in a quartz tube, placed inside a tube furnace (GSL-1100X-UL-LD, MTI Corporation), connected to nitrogen (N_2 , 99.9999% pure) and hydrogen (H_2 , 99.99% pure) sources.

First, the system was purged by a 19.5 sccm H_2 flow for one minute followed by a 20 min 1000 sccm N_2 flow. After this, the furnace was turned on and it was heated following several ramps defined by the target temperatures, rates, times and gas flow rates shown in Table I. When the process was done, the furnace was shut down and the substrate was left inside to cool down naturally. After pyrolysis, a 20 μm SU8 3035 passivation layer was patterned.

TABLE I. Temperature Ramps used in the Pyrolysis Process

Temperature [°C]	Time [min]	Rate [°C/min]	Nitrogen [sccm]	Hydrogen [sccm]
0->180	18	+10	1000	0
180->180	15	0	1000	0
180->200	2	+10	1000	0
200->200	30	0	1000	0
200->230	3	+10	1000	0
230->230	15	0	1000	0
230->260	3	+10	1000	0
260->260	15	0	1000	0
260->300	4	+10	1000	0
300->300	15	0	1000	0
300->900	60	+10	1000	0
900->900	60	0	1000	19.5
900->200	70	-10	236	0
200->0	40	-5	236	0

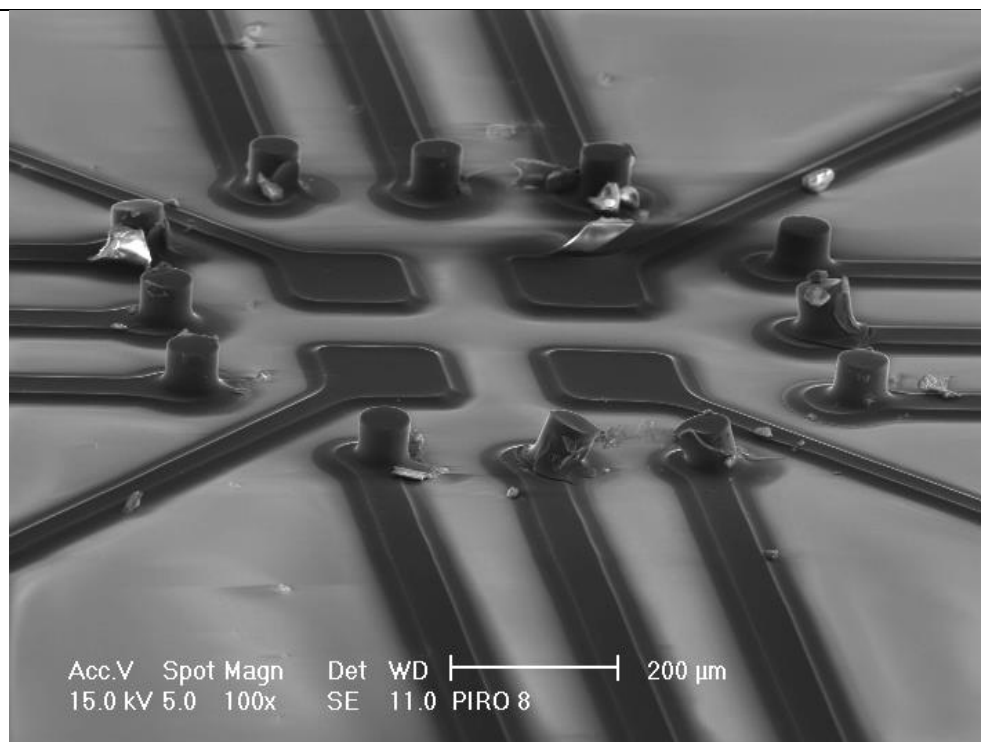


Figure 2. Scanning electron microscopy (SEM) image of the pyrolyzed device.

Electrical resistivity

To characterize the electrical resistivity (ρ) we used Van der Pauw's method, which is based on equation [1], that relates the thickness of the sample (t) and the transresistances (R_{ABCD} and R_{BCDA}) between four probes (A, B, C and D) placed along the surface of the material to this property.

$$e^{-\pi t \frac{R_{ABCD}}{\rho}} = 1 - e^{-\pi t \frac{R_{BCDA}}{\rho}} \quad [1]$$

Rectangular carbon samples were fabricated, 1.5 mm wide by 3 mm long and 14.5 μm thick, using the photolithography and pyrolysis processes described previously. Four wires contacts were attached to the sample, one in each corner, using an epoxy-based silver paste (Epoxy Technology #4898). Measurements were carried out under a vacuum pressure of 5×10^{-4} Torr.

A constant current, ranging from $-2 \mu\text{A}$ to $+2 \mu\text{A}$, was applied by a DC current source (Keithley 6221), and the resulting difference in electrical potential generated in the other two contacts was measured with a nano-voltmeter (Agilent 34420A). Two sets of measurements were performed using these parameters, one for V_{AB} induced by I_{CD} and another for V_{BC} induced by I_{DA} . Linear regression was used in the resulting curves and their slopes, which represent the transresistance (R_{ABCD}, R_{BCDA}) of the test, were used to obtain the materials resistivity.

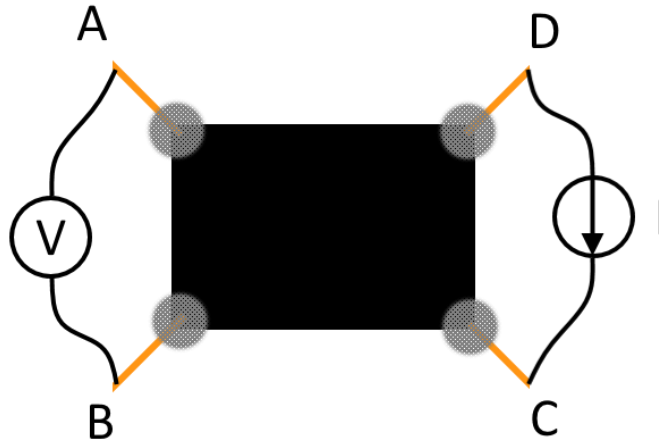


Figure 3. Diagram of an electrical resistivity carbon sample. A typical connection is shown, where a current is passed through contacts C and D (I_{CD}) and resulting voltage in contacts A and B is measured (V_{AB}).

Figure 4 shows the experimental data, as well as its linear regression, obtained for both R_{ABCD} and R_{BCDA} transresistances. Each member of equation [1] was plotted varying ρ and the resistivity value was found to be the intersection of the curves, obtaining a value of $4.828 \times 10^{-4} \Omega m$ for the carbon film resistivity.

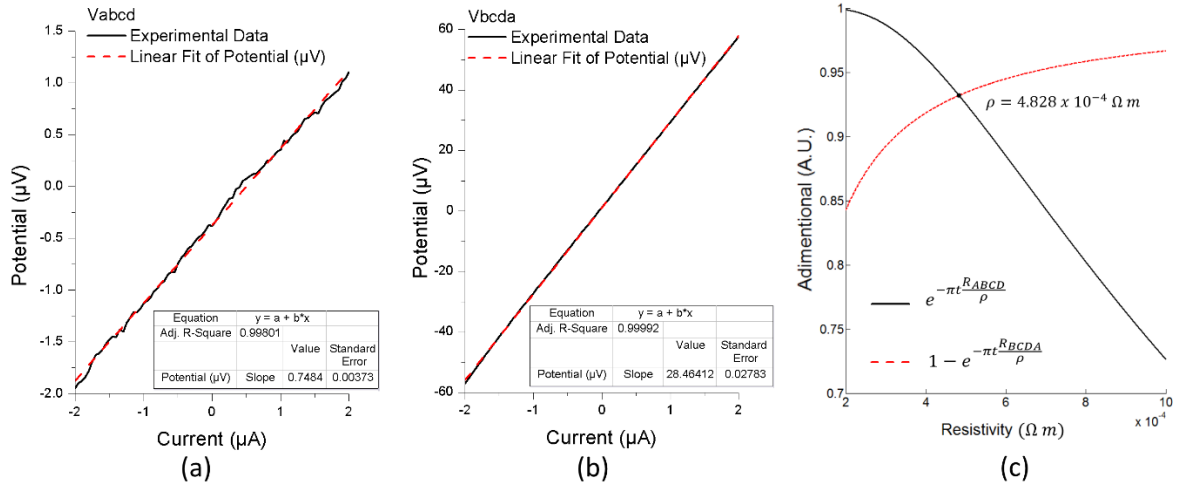


Figure 4. Experimental data and linear regressions for transresistances (a) R_{ABCD} and (b) R_{BCDA} . (c) Plot of equation [1] showing the intersection of the curves and the resistivity of the film.

Particles manipulation

The device was tested using $1 \mu m$ in diameter fluorescent spherical micro particles (FluoSpheres F-13080), suspended in a 1.6 M NaCl solution. Image sequences were acquired by means of an inverted fluorescence microscope and a high-speed camera (Phantom MIRO 310).

A planar electrode and a 3D electrode were connected to an amplifier (TREK PZD350A) and to a signal generator (Agilent 33220A). A sinusoidal signal of 60 V peak to peak and 100 kHz was applied to induce DEP force in the fluorescent particles. Under this conditions, a negative DEP force was expected.

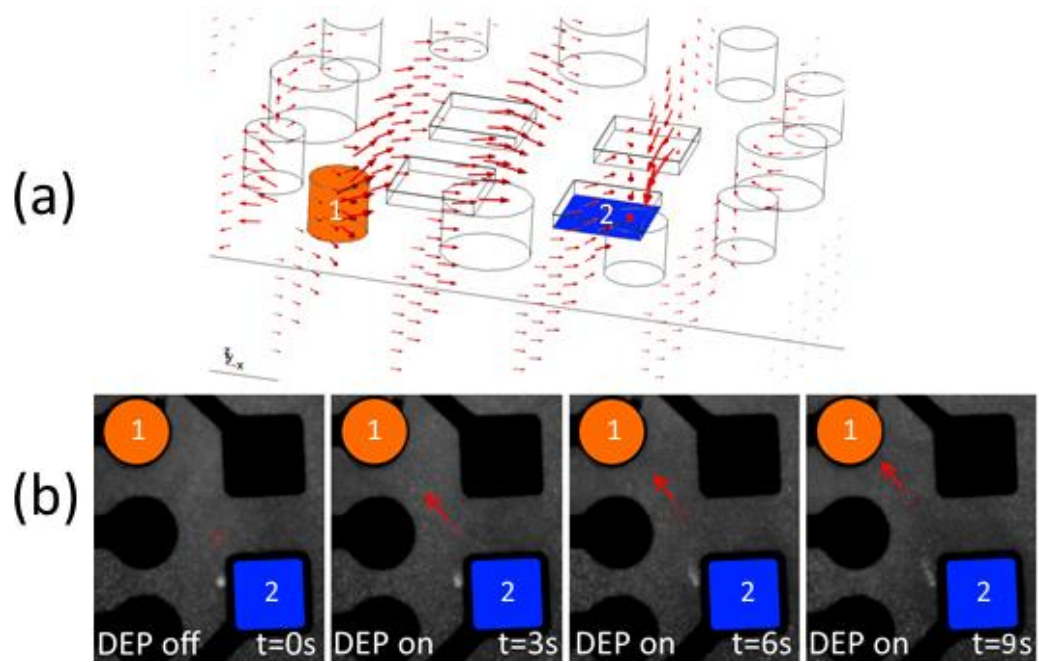


Figure 5. (a) Finite element simulation of the electric field produced between the chosen electrodes, arrows are proportional to the magnitude of the field. (b) Sequence of images showing the motion of a fluorescent particle due to DEP.

Captured images were then processed to obtain particle image velocimetry (PIV) profiles using DynamicStudio (Dantec Dynamics) in the region in between the active electrodes. The velocity profile observed in the particles matches that expected for negative DEP, where particles move away from regions of strong electric field, as shown in Figure 6.

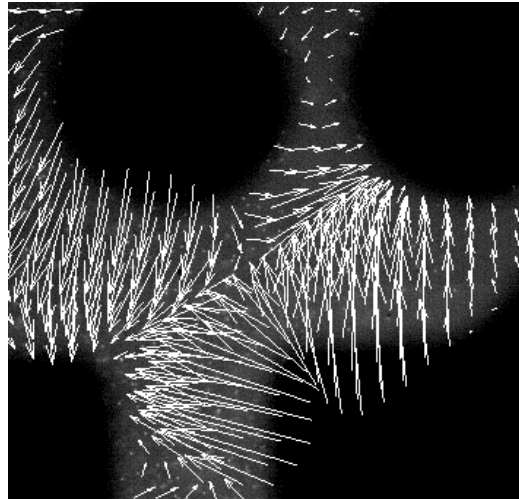


Figure 6. Particle image velocimetry profile exhibited by the fluorescent particles once the electrodes were turned on. Micro electrodes are shown in black, the arrows depict the direction of movement of the fluorescent micro particles.

Conclusions

In this work, fabrication and test of a device that uses planar and 3D carbon micro electrodes, fabricated in a transparent substrate, for the manipulation in 3D space of bio - particles using DEP force were performed.

The carbon electrodes used in this device have a resistivity and electrochemical behavior similar to other pyrolysed electrodes (11,12), but they have the distinctive advantage of presenting very high inter electrode impedance without the need of further fabrication steps.

Another improvement in the present work is the heating profile that is shown in the pyrolysis process, which enables the fabrication of high aspect ratio carbon structures in transparent substrates, enabling more straightforward use of optical microscopy.

We demonstrated here that the position of a particle can be manipulated in a tridimensional space by the use of DEP exerted by a combination of 3D and planar electrodes,

but further experimentation is needed to improve the precision and performance of this device.

Acknowledgments

This work is supported by the PAPIIT-DGAPA IN115116 Grant. We would like to acknowledge the CONACYT for providing a Ph. D. scholarship to the first author and Dr. Doroteo Mendoza from Instituto de Investigaciones en Materiales, UNAM for his assistance.

References

1. H. A. Pohl, *Appl. Phys.* (1951).
2. L. Yang et al., *Lab Chip*, 6, 896–905 (2006).
3. P. R. C. Gascoyne, X. B. Wang, Y. Huang, and R. F. Becker, *IEEE Trans. Ind. Appl.*, 33, 670–678 (1997).
4. R. Pethig, A. Menachery, S. Pells, and P. De Sousa, *J. Biomed. Biotechnol.*, 2010, 182581 (2010).
5. T. P. Hunt, H. Lee, and R. M. Westervelt, *Appl. Phys. Lett.*, 85, 6421–6423 (2004).
6. R. Martinez-Duarte, P. Renaud, and M. J. Madou, *Electrophoresis*, 32, 2385–2392 (2011).
7. C. Wang and M. Madou, *Biosens. Bioelectron.*, 20, 2181–2187 (2005).
8. M. Madou, V. Perez-Gonzalez, and B. Pramanick, *Carbon: The New Silicon?: Book I - Fundamentals*, (2016).
9. A. Singh, J. Jayaram, M. Madou, and S. Akbar, *J. Electrochem. Soc.*, 149, 78–83 (2002).
10. K. Khoshmanesh, S. Nahavandi, S. Baratchi, A. Mitchell, and K. Kalantar-zadeh, *Biosens. Bioelectron.*, 26, 1800–1814 (2011).
11. J. a Lee, S. W. S. S. Lee, K.-C. Lee, S. Il Park, and S. W. S. S. Lee, *J. Micromechanics Microengineering*, 18, 035012 (2008).
12. J. Kim, X. Song, K. Kinoshita, M. Madou, and B. White, *J. Electrochem. Soc.*, 145, 2314–2319 (1998).

- **APPENDIX I: ARTICLE “METHODODOLOGY AND FABRICATION OF ADHERENT AND CRACK-FREE SU-8 PHOTORESIST-DERIVED CARBON MEMS ON FUSED SILICA TRANSPARENT SUBSTRATES”**

Methodology and Fabrication of Adherent and Crack-free SU-8 Photoresist-derived Carbon MEMS on Fused Silica Transparent Substrates

*Oscar Pilloni ^a, Marc Madou ^b, Doroteo Mendoza ^c, Stephen Muhl ^c, Laura Oropeza-Ramos ^{*d}*

^a Programa de Maestría y Doctorado en Ingeniería, Universidad Nacional Autónoma de México, CDMX, México.

^b Department of Mechanical and Aerospace Engineering, University of California, Irvine, USA.

^c Instituto de Investigaciones en Materiales, Universidad Nacional Autónoma de México, CDMX, México.

^d Facultad de Ingeniería, Universidad Nacional Autónoma de México, CDMX, México.

*Corresponding author:

[Laura Oropeza-Ramos](mailto:loropeza@unam.mx)

Facultad de Ingeniería, Departamento de Electrónica

Edificio "P" DIE, 3er piso, Anexo de Ingeniería, CU, C.P. 04510 México, CDMX

Tel: (52.55) 5622.31.20, (DIE) 5622.31.12

loropeza@unam.mx

Abstract

Development of carbon based micro electromechanical systems (C-MEMS) has enabled the fabrication of durable, low cost and biocompatible micro devices for specific applications. Thermochemical decomposition of SU-8 (a common photoresist) is often used to fabricate C-MEMS. However, this technique has yielded unreliable results when fabrication on transparent substrates is required due to cracking and detachment of the produced carbon micro structures. We present a methodology for the fabrication of photopatterned carbon films based on SU-8 deposited on transparent fused silica substrates. Specifically, we developed and implemented this methodology for carbon microstructure fabrication derived from SU-8 2035 and SU-8 3035. It was found that SU-8 3035 derived carbon microstructures were crack free and adhered well to the substrate, while SU-8 2035 resulted in fractured and detached carbon microstructures. In addition, we characterized the produced SU-8 3035 derived carbon by measuring its electrical resistivity ($1.412 \pm 0.011 \text{ m}\Omega \text{ m}$), inter-structure electrical resistance, contact angle ($35.7^\circ \pm 6.0^\circ$), Raman spectrum and adhesion strength to the substrate. In brief, even though SU-8 2035 and SU-8 3035 are useful materials for C-MEMS fabrication, we found that SU-8 3035 is more suitable for the fabrication of crack free and adherent carbon microstructures on transparent fused silica substrates.

Keywords

MEMS; Micro-structure; SU-8; Pyrolysis; Transparent substrate; Carbon.

1. Introduction

Carbon-based micro electromechanical systems (C-MEMS) [1,2] are a collection of technologies that enable the fabrication of carbon microstructures which range from low aspect ratio transparent electrodes [3] to high aspect ratio carbon posts [4] which show desirable properties such as biocompatibility, electrochemical inertness and electrical conduction. C-MEMS are used to build devices for applications in a plethora of fields, such as microfluidics [5], point of care diagnostics [6] and energy storage [7], to list a few.

Although carbon and its allotropes are useful and interesting materials they have proven difficult to pattern in the micro and nano scales. In particular, C-MEMS technology has emerged as a solution by producing devices that use photopatterned pyrolyzed photoresist films (PPF) as building blocks [1,8], with SU-8 photoresist being one of the most popular photo-patternable carbon precursors due to its versatility and ubiquity in traditional MEMS manufacturing.

Moreover, C-MEMS fabrication on transparent substrates enable versatility during the fabrication or the operation of specialized devices when optical transparency is required [9], for example when transmitted light microscopy is desired for observation. Another desirable property for biomedical applications is biocompatibility. Some types of transparent substrates such as fused silica are biocompatible whereas silicon (a common C-MEMS substrate material) has been shown to affect biological and biochemical processes [10–12]. In brief, the useful properties of transparent substrates make them attractive for some application, especially for biomedical and biochemical applications. However, SU-8 derived C-MEMS structure fabrication has been plagued with the vexing problems of cracking and poor adhesion of the PPF to common transparent substrates suitable for pyrolysis [13].

In this paper, we present a methodology for the fabrication of SU-8 derived C-MEMS structures devoid of cracks and well adhered to a transparent substrate. We show that using the more recent SU-8 3035 formulation results in well adhered carbon microstructures whereas the use of the more common SU-8 2035 results in serious adhesion and cracking problems of the PPF. Finally, we report the adhesion strength to the substrate, electrical resistivity, inter-structure electrical resistance, contact angle and Raman spectrum of the produced PPF.

2. Methodology

2.1. Material selection and process outline

Fused silica was selected as substrate material due to its optical transparency, high melting point (which makes it able to withstands the high temperatures needed for the pyrolysis process) and lower cost compared to other alternatives (such as sapphire).

SU-8 2035 and SU-8 3035 photoresists were selected because they are photo-patternable, widely available and suitable for the fabrication of microstructures in sizes ranging from tens to hundreds of micrometers.

We maintained most fabrication parameters constant to show the difference in adhesion due to the photoresists' formulation under the same fabrication and pyrolysis conditions. For this reason, no adhesion promoters were employed and a constant layer thickness was used. A layer thickness of 35 μm was selected because the formulations of both photoresists (SU-8 2035 and 3035) are made specifically to easily achieve this value.

First, samples of SU-8 2035 and SU-8 3035 photoresists were fabricated on the substrate using mask-less photolithography. Secondly, pyrolysis of the photoresists was carried out to obtain the carbon microstructures.

2.2. Photolithography process

2.2.1. Substrate preparation

Fused silica substrates (JGS2 grade, 500 μm thick, UniversityWafer Inc) were cleaned with acetone and isopropyl alcohol and then heated to 230 $^{\circ}\text{C}$ for one hour on a hot plate to dehydrate the surface.

2.2.2. Photoresist coating

Depending on the sample, SU-8 2035 or SU-8 3035 (Microchem) was spin-coated at 3000 rpm on the substrates to obtain 35 μm thick layers.

2.2.3. Sample soft bake

The photoresist coated substrates were soft baked on a hotplate using a heating ramp of 10 °C/min from room temperature (18 °C) to the target temperature of 105 °C. The target temperature was maintained constant for 20 minutes. Afterwards, the hot plate was tuned off and the substrates were left to cool down naturally.

2.2.4. Photopatterning

Photoresist patterning was performed in a mask-less photolithography system (SF100 XCEL, Intelligent MicroPatterning) with a resolution of 1.25 µm and a minimum feature size of 5 µm. The system uses a digital micro-mirror device (DMD) to reflect or block the collimated and filtered light of a polychromatic mercury arc lamp. By this means, the digital pattern loaded into the DMD is transmitted by an optical array to the surface of a target sample [14]. The dose administered is controlled by the time the pattern is exposed to the sample. Exposure time was set to 7.1 s using a wavelength of 365 nm.

2.2.5. Sample post exposure bake

Post exposure bake of the samples was carried on a hotplate using a heating ramp of 10 °C/min from room temperature to the target temperature of 105 °C. The target temperature was held constant for 6 minutes. Then, the hot plate was tuned off and the substrates were left to cool down naturally.

2.2.6. Microstructure development and final bake

Samples were developed for five minutes using SU-8 Developer (Microchem) and a moderate agitation with an orbital shaker. Afterwards, the samples were dried using nitrogen.

The final bake of the samples was performed on a hot plate using a heating ramp of 10°C/min from room temperature to a target temperature of 190 °C. The target temperature was held constant for one hour. Then, temperature was decreased at a rate of 10 °C/min until natural cooling took over and samples were left to reach room temperature. Active cooling was not used during the baking procedures.

2.3. Pyrolysis process

Pyrolysis was performed using a quartz tube furnace (GSL-1100X-UL-LD, MTI) under a constant pure nitrogen (99.99%) flow of 1000 sccm. The target temperature of the process was set to 900 °C, following the temperature profile depicted in Fig. 1 d. The atmosphere was switched to a forming gas mixture of 95% nitrogen and 5% hydrogen (99.998%) upon reaching the target temperature [15].

After one hour at the target temperature of 900 °C, atmosphere was switched back to pure nitrogen and cooling was performed at a rate equal to or slower than 10 °C/min until the sample reached ambient temperature. Active cooling was not used during this procedure.

Finally, the samples were exposed to a nitrogen stream to clean them of fractured structures that had peeled-off from the substrate.

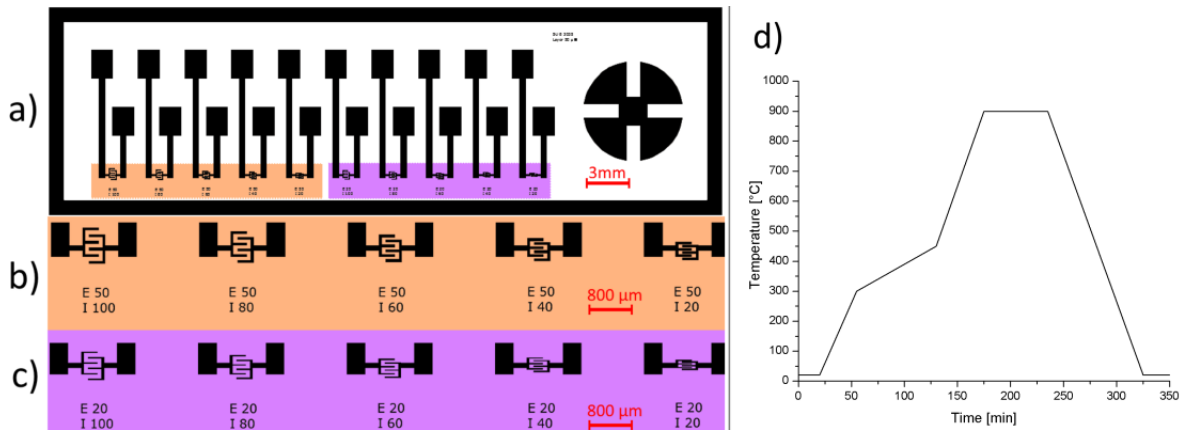


Fig. 1: a) Test pattern used for the pyrolyzed photoresist films (PPF) samples. It consisted of ten arrays of interdigitated electrodes (IDEs) for inter-structure electrical resistance measurement and a cloverleaf shaped structure for electrical resistivity measurement, contact angle and adhesion strength measurements. Detail of the (b)) five IDEs with 50 μm width and interdigit spacing of 100, 80, 60, 40 and 20 μm; and the (c)) five IDEs with 20 μm width and interdigit space of 100, 80, 60, 40 and 20 μm. d) The temperature profile for the pyrolysis process.

3. Results and discussion

The photolithography and pyrolysis processes described above were used to fabricate five carbon samples made of SU-8 2035 and five carbon samples made of SU-8 3035. The test pattern shown in Fig. 1 a-c was used to fabricate the samples. It consisted of ten arrays of interdigitated electrodes (IDEs) for inter-structure electrical resistance measurement (combinations of 50 and 20 μm electrode widths with interdigit spacings of 100, 80, 60, 40 and 20 μm), and a cloverleaf shaped structure for electrical resistivity, contact angle and adhesion strength measurements.

As noted by Martinez-Duarte et. al. [16], the final bake procedure was found to be imperative to maintain adhesion of PPFs to fused silica substrates after pyrolysis. In order to improve the success rate of the pyrolysis, we used a slower ramping rate for the pyrolysis between 300 and 450 $^{\circ}\text{C}$, which corresponds to the main carbonization of the materials, to accommodate any stress developed in the film during the carbonization [17].

After fabrication, we found that all the SU-8 3035 samples had most of their structures well-adhered to the substrate and with no appreciable fractures observable by optical microscopy or SEM. However, the five SU-8 2035 samples presented mayor cracking and detachment from the substrate, as shown in Fig. 2.

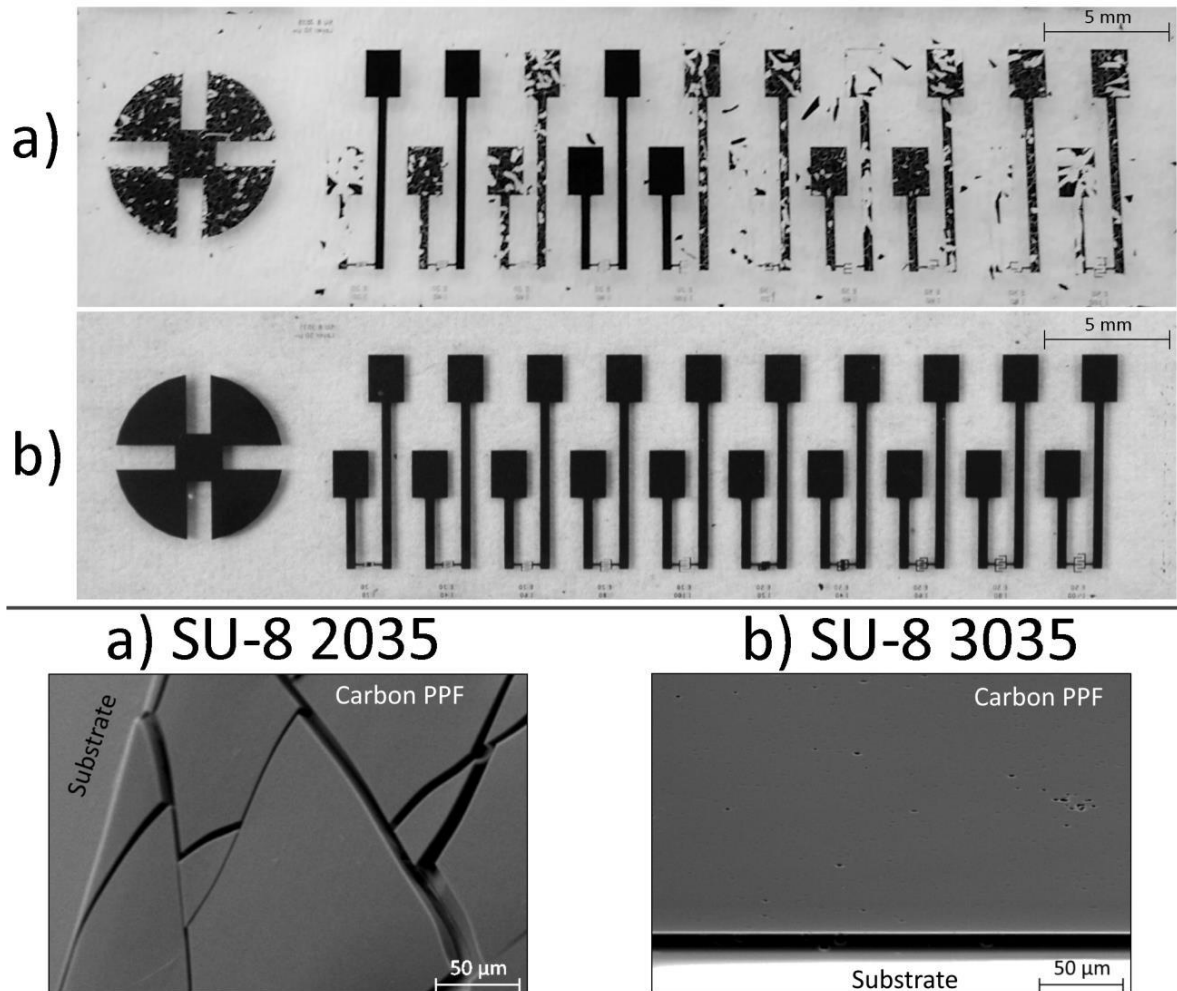


Fig. 2: Optical photograph (top) and SEM (bottom) images of typical samples of pyrolyzed a) SU-8 2035 and b) SU-8 3035. Most, if not all, of the SU-8 2035 structures were fractured and not well-adhered to the substrate after pyrolysis; while SU-8 3035 structures maintained their shape and kept good adhesion to the fused silica substrate.

A possible explanation for the difference in adhesion between SU-8 3035 and 2025 samples stem from the shear analysis performed by the photoresists manufacturer using a similar substrate material (quartz). This analysis showed that SU-8 3035 and SU-8 2035 films had adhesion strengths of 80 MPa and 61 MPa, respectively [18].

The SU-8 2035 weaker adhesion strength prior to pyrolysis, in addition to the thermal stresses introduced during the pyrolysis process, could be the cause of the observed detachment and cracking of the PPF. This might mean that the bonding strength of the carbon structure to the substrate could be dependent on the adhesion of the carbon precursor to the substrate before pyrolysis. To explore this, measurements of adhesion to the substrate were conducted for both photoresists before and after pyrolysis.

Given that all SU-8 2035 samples presented mayor detachment and cracking problems, measurements of electrical resistivity, inter-structure electrical resistance, contact angle and Raman spectrum were only performed on the SU-8 3035 samples. Measurements of adhesion strength to the substrate were carried in the SU-8 2035 structures that remained adhered and intact after pyrolysis.

3.1. Adhesion strength to the substrate

SU-8 3035 and SU-8 2035 PPF adhesion to the fused silica substrate was tested using micro-scratch testing and sonication before and after pyrolysis.

The scratch test consists of a moving load applied by a counter body of known shape and size to a film or coating. To assess the adhesion force, the load is increased until a critical value where the film detaches from the substrate. This critical load is a function of film-substrate adhesion, flaw size distribution at substrate-film interface, mechanical properties of substrate and film, film thickness, counter body tip radius, loading rate, internal stress in coating, and friction between counter body tip and coating [19–23].

First, samples were subjected to a variable-load scratch test (0.2 to 15 N at a loading rate of 7.5 N/min) using a micro-scratch tribometer (Nanovea, PB1000) and a 200 μm diameter spherical diamond tip as the counter body. Measurements of the SU-8 2035 PPF were carried on the few adherent structures that withstood the pyrolysis process. Fig. 3 summarizes these data points obtained. Also, scratch tests were made for both photoresists deposited in a silicon substrate as control experiments for comparison.

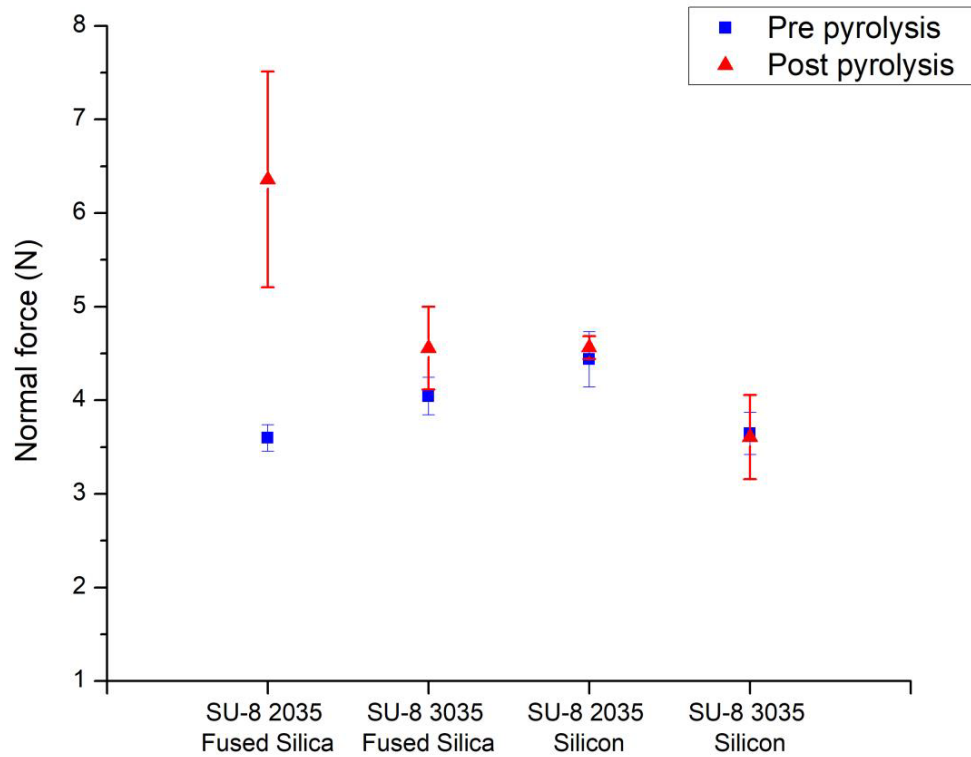


Fig. 3: Critical load (normal force) required to delaminate the photoresists films from their substrate. Measurements for before and after pyrolysis process are provided.

Secondly, samples were submerged in deionized water and treated in an ultrasonic bath for five minutes. Optical microscopy was used to search for cracked or detached structures. However, no appreciable changes were found in any SU-8 3035 sample, before or after pyrolysis. That is, structures remained intact and well-adhered to the fused silica substrate. This constitutes a significant improvement over similar tests made in previous works [13]. On the other hand, SU-8 2035 structures showed complete to partial detachment, with only a few structures remaining adherent to the substrate. This behavior occurred to SU-8 2035 structures both before and after pyrolysis. Photographs of this test are provided in a supplementary information document.

These results indicate that the produced PPF adhesion to the substrate after pyrolysis may be independent from its adhesion to fused silica but closely related for silicon before the process, and that this parameter may not be related to the cracking problems of the PPF due to it being similar for both photoresists. However, the severe delamination problems presented by SU-8 2035 during sonication suggests that the interface of the photoresist to substrate is highly susceptible to humidity and vibration, whereas SU-8 3035 remained impervious to the test. This property of SU-8 3035 PPFs may prove useful for cleaning procedures, or for the intended operation of devices fabricated with the proposed method.

3.2. Electrical resistivity

Van der Pauw [24] resistivity measurements of the pyrolyzed films were carried out using a source meter (Keithley 2636B) connected to the cloverleaf shaped structure shown in Fig. 1. An average resistivity of $1.412 \pm 0.011 \text{ m}\Omega \text{ m}$ was measured across all pyrolyzed SU-8 3035 samples.

The measured resistivity is comparable to previous electrical measurements of original SU-8 formulation, and polyimide-derived carbon PPFs [13,25]. This makes the obtained material useful for devices that require electrical conductivity, such as microelectrode arrays.

3.3. Inter-structure electrical resistance

As pointed out by Matias et. al. [26], sometimes the C-MEMS process results in undesirable residual conducting carbon layers in areas originally designed to be insulating. Interdigitated electrodes with varying inter-electrode spacing (Fig. 4) were used to measure the inter-structure electrical resistance resulting from such spurious layers produced by the proposed methodology.

Spacing equal or greater than $40 \mu\text{m}$ between electrodes resulted in electrically isolated structures, with electrical resistances higher than what we were able to measure ($>109 \Omega$, Fluke 116). Electrodes with $20 \mu\text{m}$ inter-structure spacing resulted in electrically connected structures, showing electrical resistances of 103Ω .

This likely indicates that the combination of the careful selection of inter-microstructure spacing, and the good adhesion of the carbon film to the substrate could influence the reproducibility of devices free of residual layer without the need for further processing.

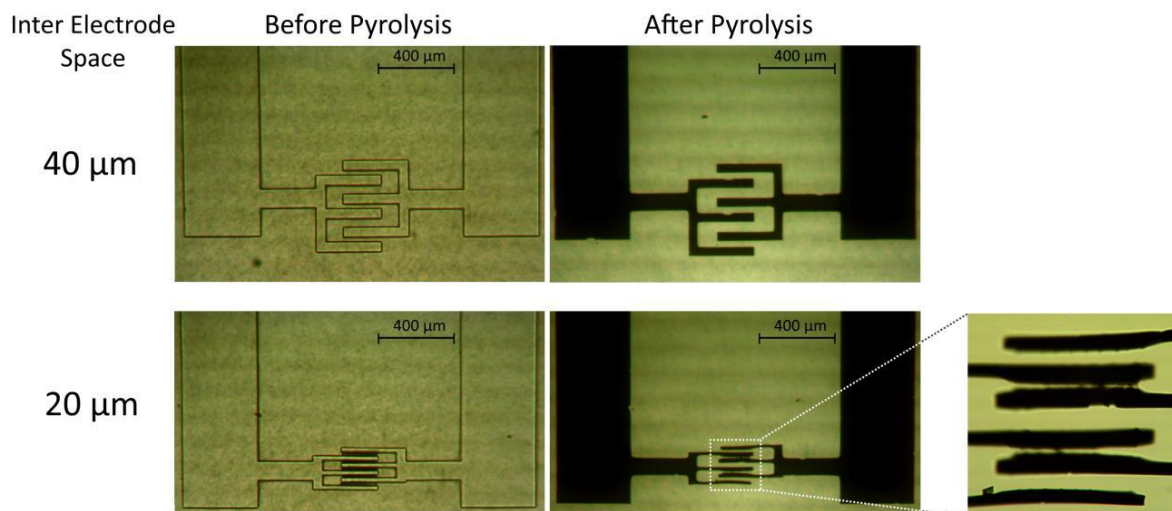


Fig. 4: SU-8 3035 interdigitated electrodes (IDEs) before and after pyrolysis. IDEs with an inter-structure spacing equal or greater than $40\ \mu\text{m}$ were electrically isolated from adjacent features, whereas features with $20\ \mu\text{m}$ separations were electrically connected (bonded by residual material trapped in between the IDEs).

3.4. Raman spectroscopy

Raman spectroscopy has been proven to reliably obtain microstructural information of thin carbon films[27]. For this reason, Raman spectra of the SU-8 3035 samples were obtained. We measured the spectra at 3 different locations on each sample, using a 532 nm wavelength laser Raman microscope (DXR, Thermo Scientific). The wavenumber for the G band (associated with the graphitic content of the PPF) was found at $1591.7 \pm 2.55\ \text{cm}^{-1}$ and the D band (associated with the level of disorder of the carbon lattice) was found at $1333.5 \pm 2.25\ \text{cm}^{-1}$ (Fig. 5 a-b). We calculated an average D to G band intensity ratio (ID/IG) of 0.9694 ± 0.0503 .

These results suggest that the achieved material is comparable to glassy carbon, which is a useful type of carbon for electrochemical applications [2,7]. All samples showed homogenous Raman spectra across each sample (Fig. 5 a) and overall (Fig. 5 b), which shows that the proposed methodology can produce a uniform and highly reproducible material.

3.5. Contact angle measurements

A set of contact angle measurements were made to investigate the carbon hydrophobicity. We used 38 μl droplets of deionized water on the carbon surface of the SU-8 3035 samples and measured an average contact angle of $35.7^\circ \pm 6.0^\circ$. A representative measurement is shown in Fig. 5 c.

Previous reports have shown that the contact angle of SU-8 derived PPFs is affected by post-carbonization surface treatments and various fabrication variables, such as the pyrolysis atmosphere [28]. Furthermore, measurements performed by C. S. Sharma on pyrolyzed SU-8 2000 films showed post pyrolysis angles of around 70° [29]. The variables that could have affected this angle include the photoresist formulation, and therefore the pyrolysis by-products, and the inert atmosphere used during pyrolysis.

Although both Sharma's and our results indicate a hydrophilic surface, our samples had a contact angle that was roughly half of that reported immediately after fabrication. This makes the obtained microstructured carbon attractive for applications that require a hydrophilic surface without the need of further surface treatment.

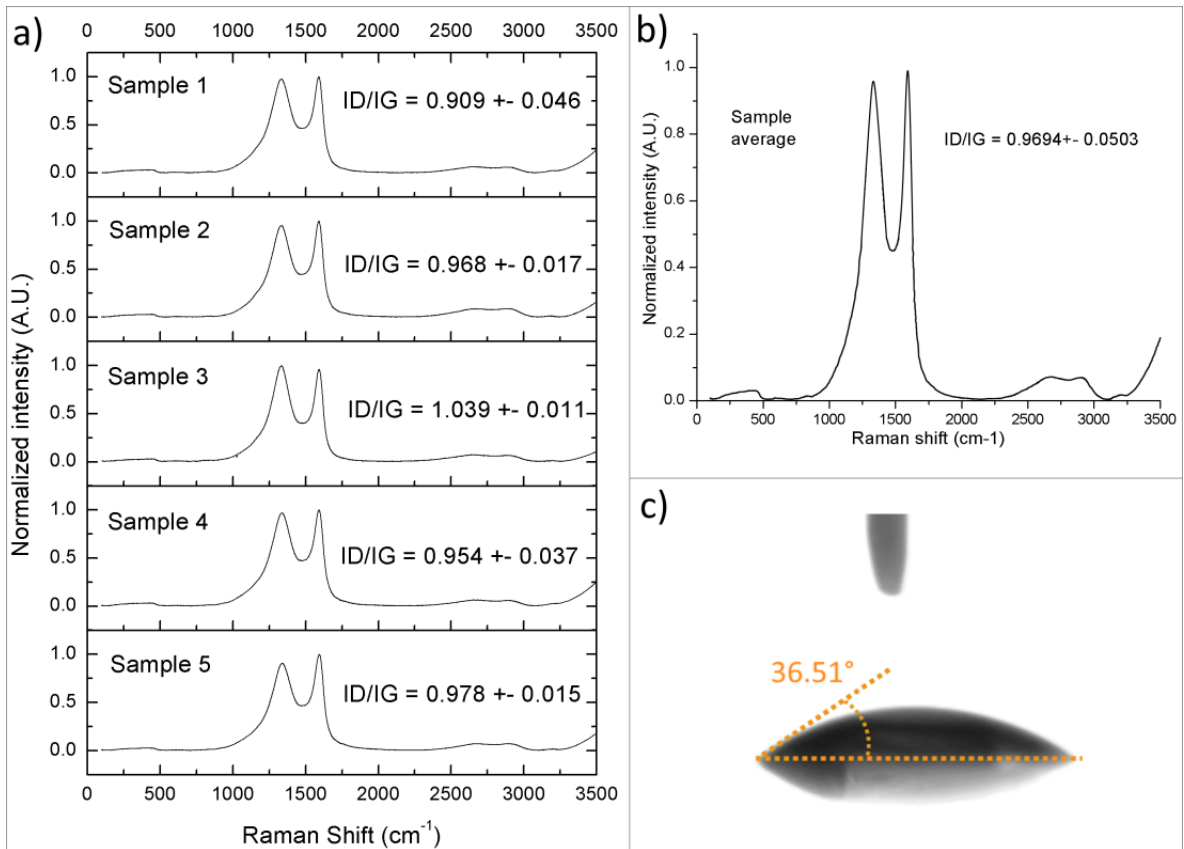


Fig. 5: Average Raman spectra obtained from pyrolyzed SU-8 3035 for a) each sample (n=3) and b) overall (n=15). Intensity ratios of D and G peaks (ID/IG) are shown for each sample and an overall average. c) A contact angle measurement made on the PPF. The dark blob is water, the tip at the top is the liquid dispenser and the gray area below the dotted line results from the droplet's reflection on the carbon surface.

4. Conclusions

We have shown that the proposed methodology is suitable for the fabrication of SU-8 3035 derived C-MEMS microstructures devoid of cracks which have good adhesion to transparent substrates.

In brief, SU-8 3035 was found more suitable to produce adherent carbon microstructures on transparent fused silica substrates, while SU-8 2035 yields fractured and detached microstructures following the same fabrication methodology. Both photoresists presented similar adhesion strength to fused silica before and after pyrolysis, but SU-8 2035 interface to the substrate showed mayor susceptibility to water resulting in the detachment of the film from the substrate. This suggests that the exposure of SU-8 2035 films to ambient humidity may play a determining factor for the success or failure of the fabrication of C-MEMS devices based on that photoresist built on fused silica.

In conclusion, the low resistivity, hydrophilic contact angle, lack of cracking, good adhesion and lack of susceptibility to water of the interface to fused silica of SU-8 3035 derived PPF produced with the proposed method provides enough design flexibility to build novel C-MEMS on transparent substrates for applications that require optical transparency, such as biomedical, medical or biological applications requiring the use of optical microscopy with transmitted illumination for the inspection of samples.

Author Contributions

The manuscript was written with contributions from all the authors. All authors have given approval to the final version of the manuscript.

Acknowledgements

This work was funded by DGAPA-PAPIIT-UNAM [grant number IN115116] and by CONACYT-UNAM [project number 269280] for the acquisition of the Nanovea tribometer. Partially funded by CONACYT Fronteras de la Ciencia [grant number 344] and PAPIIT [grant number IN106316]. The first author was supported by CONACYT scholarship [scholarship number 487698], and we also would like to thank Ing. Ma. Cristina Zorrilla Cargas from the

Laboratorio de Materiales Avanzados, Instituto de Física, UNAM for her assistance in the Raman spectroscopy.

Competing Interests

The authors declare that they have no competing interests.

References

- [1] Wang C and Madou M 2005 From MEMS to NEMS with carbon Biosens. Bioelectron. 20 2181–7.
- [2] Ranganathan S, McCreery R, Majji S M and Madou M 2000 Photoresist-Derived Carbon for Microelectromechanical Systems and Electrochemical Applications J. Electrochem. Soc. 147 277.
- [3] Donner S, Li H W, Yeung E S and Porter M D 2006 Fabrication of optically transparent carbon electrodes by the pyrolysis of photoresist films: Approach to single-molecule spectroelectrochemistry Anal. Chem. 78 2816–22.
- [4] Wang C, Jia G, Taherabadi L H and Madou M J 2005 A novel method for the fabrication of high-aspect ratio C-MEMS structures J. Microelectromechanical Syst. 14 348–58.
- [5] Rouabah H a, Park B Y, Zaouk R B, Morgan H, Madou M J and Green N G 2011 Design and fabrication of an ac-electro-osmosis micropump with 3D high-aspect-ratio electrodes using only SU-8 J. Micromechanics Microengineering 21 035018.
- [6] Martinez-Duarte R, Gorkin R a, Abi-Samra K and Madou M J 2010 The integration of 3D carbon-electrode dielectrophoresis on a CD-like centrifugal microfluidic platform. Lab Chip 10 1030–43.
- [7] Wang C, Taherabadi L, Jia G, Madou M, Yeh Y and Dunn B 2004 C-MEMS for the Manufacture of 3D Microbatteries Electrochem. Solid-State Lett. 7 A435.
- [8] Pilloni O, Benítez Benítez J L and Oropeza-Ramos L 2016 Micro Device for Bio-Particle Positioning in a 3D space based on Carbon MEMS and Dielectrophoretic Forces ECS Trans. 72 17–24.
- [9] Martinez-Duarte R 2014 SU-8 Photolithography as a Toolbox for Carbon MEMS Micromachines 5 766–82.

- [10] Steinhauer C, Ressine A, Marko-Varga G, Laurell T, Borrebaeck C A K and Wingren C 2005 Biocompatibility of surfaces for antibody microarrays: Design of macroporous silicon substrates *Anal. Biochem.* 341 204–13.
- [11] Coletti C, Jaroszeski M J, Pallaoro A, Hoff A M, Iannotta S and Sadow S E 2007 Biocompatibility and wettability of crystalline SiC and Si surfaces *Annu. Int. Conf. IEEE Eng. Med. Biol. - Proc.* 5849–52.
- [12] Ni M, Tong W H, Choudhury D, Rahim N A A, Iliescu C and Yu H 2009 Cell culture on MEMS platforms: A review. *Int. J. Mol. Sci.* 10 5411–41.
- [13] Singh A, Jayaram J, Madou M and Akbar S 2002 Pyrolysis of Negative Photoresists to Fabricate Carbon Structures for Microelectromechanical Systems and Electrochemical Applications *J. Electrochem. Soc.* 149 E78.
- [14] Xiang N, Yi H, Chen K, Wang S and Ni Z 2013 Investigation of the maskless lithography technique for the rapid and cost-effective prototyping of microfluidic devices in laboratories *J. Micromechanics Microengineering* 23.
- [15] Pilloni O, Benítez J L B, Olguín L F, Palacios-Morales C A and Oropeza-Ramos L 2016 Micro Device for Bio-Particle Positioning in a 3D space based on Carbon MEMS and Dielectrophoretic Forces *ECS Transactions* vol 72.
- [16] Martinez-Duarte R, Renaud P and Madou M J 2011 A novel approach to dielectrophoresis using carbon electrodes *Electrophoresis* 32 2385–92.
- [17] G. M. Jenkins K K 1976 *Polymeric Carbons: Carbon Fibre, Glass and Char* (Cambridge University Press).
- [18] Microchem SU-8 Table of properties.
- [19] Bull S J 1997 Failure Mode Maps in the Thin Scratch Adhesion Test *Tribol. Int.* 30.
- [20] Kutilek P and Miksovsky J 2011 The procedure of evaluating the practical adhesion strength of new biocompatible nano-and micro-thin films in accordance with international standards *Acta Bioeng. Biomech.* 13 87–94.

[21] Bull S J 1991 Failure Modes in Scratch Adhesion Testing Surf. Coatings Technol. 50 25–32.

[22] Mittal K L 1976 Adhesion Measurement of Thin Films Electrocompon. Sci. Technol. 3 21–42.

[23] Matthewson M J 1986 Adhesion measurement of thin films by indentation Appl. Phys. Lett. 49 1426.

[24] van der Pauw L J 1958 A method of measuring the resistivity and hall coefficient of discs of arbitrary shape Philips Res. Reports 13 1–9.

[25] Park B Y, Taherabadi L, Wang C, Zoval J and Madou M J 2005 Electrical Properties and

Shrinkage of Carbonized Photoresist Films and the Implications for Carbon Microelectromechanical Systems Devices in Conductive Media J. Electrochem. Soc. 152 J136.

[26] Vázquez Piñón M, Cárdenas Benítez B, Pramanick B, Perez-Gonzalez V H, Madou M J, Martinez-Chapa S O and Hwang H 2017 Direct current-induced breakdown to enhance reproducibility and performance of carbon-based interdigitated electrode arrays for AC electroosmotic micropumps Sensors Actuators, A Phys. 262 10–7.

[27] Tuinstra F and Koenig J L 1970 Raman Spectrum of Graphite J. Chem. Phys. 53 1126–30.

[28] Hsia B, Kim M S, Vincent M, Carraro C and Maboudian R 2013 Photoresist-derived porous carbon for on-chip micro-supercapacitors Carbon N. Y. 57 395–400.

[29] Sharma C S, Sharma A and Madou M 2010 Multiscale carbon structures fabricated by direct micropatterning of electrospun mats of SU-8 photoresist nanofibers Langmuir 26 2218–22.